2014/2 vol.11

# ACTA GEOTECHNICA SLOVENICA

2014/2

**Mladen Ćosić et al.**
NUMERICAL SIMULATION OF THE PILE INTEGRITY TEST ON DEFECTED PILES

**Suchit D. Gumaste et al.**
DETERMINATION OF FABRIC ALTERATION OF MARINE CLAYS

**Manolo Galván et al.**
CORRELATION BETWEEN THE POINT LOAD INDEX, $I_{s(50)}$, AND RESISTANCE TO UNCONFINED COMPRESSION IN LIMESTONE FROM THE COMUNIDAD VALENCIANA (SPAIN)

**Hojjat Ahmadi et al.**
EXPERIMENTAL RESEARCH ON VARIATION OF PORE WATER PRESSURE IN CONSTANT RATE OF STRAIN CONSOLIDATION TEST

**Xinhua Xue et al.**
ESTIMATING PIPING POTENTIAL IN EARTH DAMS AND LEVEES USING GENERALIZED NEURAL NETWORKS

**Erol Sadoğlu**
DESIGN OPTIMIZATION FOR SYMMETRICAL GRAVITY RETAINING WALLS

ISSN 1854-0171

ISSN: 1854-0171

ACTA
GEOTECHNICA
SLOVENICA

| ustanovitelji | founders |
|---|---|

Univerza v Mariboru, Fakulteta za gradbeništvo
University of Maribor, Faculty of Civil Engineering

Univerza v Ljubljani, Fakulteta za gradbeništvo in geodezijo
University of Ljubljana, Faculty of Civil and Geodetic Engineering

Univerza v Ljubljani, Naravoslovnotehniška fakulteta
University of Ljubljana, Faculty of Natural Sciences and Engineering

Slovensko geotehniško društvo
Slovenian Geotechnical Society

Društvo za podzemne in geotehniške konstrukcije
Society for Underground and Geotechnical Constructions

| izdajatelj | publisher |
|---|---|

Univerza v Mariboru, Fakulteta za gradbeništvo
University of Maribor, Faculty of Civil Engineering

| lektor | proof-reader |
|---|---|
| Paul McGuiness | |

| naklada | circulation |
|---|---|
| 300 izvodov - issues | |

| cena | price |
|---|---|

25 EUR/letnik - 25 EUR/vol.; (50 EUR for institutions/za institucije)

| tisk | print |
|---|---|
| Tiskarna Koštomaj d.o.o. | |

Revija redno izhaja dvakrat letno. Članki v reviji so recenzirani s strani priznanih mednarodnih strokovnjakov. Baze podatkov v katerih je revija indeksirana: SCIE - Science Citation Index Expanded, JCR – Journal Citation Reports / Science Edition, ICONDA - The international Construction database, GeoRef. Izid publikacije je finančno podprla Javna agencija za raziskovalno dejavnost Republike Slovenije iz naslova razpisa za sofinanciranje domačih periodičnih publikacij.

| naslov uredništva | address |
|---|---|

ACTA GEOTECHNICA SLOVENICA
Univerza v Mariboru, Fakulteta za gradbeništvo
Smetanova ulica 17, 2000 Maribor, Slovenija
Telefon / Telephone: +386 (0)2 22 94 300
Faks / Fax: +386 (0)2 25 24 179
E-pošta / E-mail: ags@uni-mb.si

| spletni naslov | web address |
|---|---|
| http://www.fg.uni-mb.si/journal-ags/ | |

The journal is published twice a year. Papers are peer reviewed by renowned international experts. Indexation data bases of the journal: SCIE - Science Citation Index Expanded, JCR – Journal Citation Reports / Science Edition, ICONDA- The international Construction database, GeoRef. The publication was financially supported by Slovenian Research Agency according to the Tender for co-financing of domestic periodicals.

# VSEBINA

# CONTENTS

# UVODNIK

V začetku leta 2014 so me člani Izdajateljskega sveta revije Acta Geotechnica Slovenica imenovali za novo glavno urednico revije.  Na tem mestu sem nadomestila dolgoletnega glavnega urednika prof.dr. Ludvika Traunerja, ki je to delo opravljal kar deset let, od začetka izhajanja revije.

Tudi moje sodelovanje pri izdajanju revije AGS se je pričelo že ob njeni zasnovi leta 2004. Takrat smo sodelavci Katedre za geotehniko Fakultete za gradbeništvo v Mariboru, pod vodstvom prof.dr. Ludvika Traunerja, z  idejo o izdajanju slovenske geotehniške revije seznanili kolege s Fakultete za gradbeništvo in geodezijo ter Naravoslovnotehniške fakultete Univerze v Ljubljani, člane Slovenskega geotehniškega društva ter Slovenskega društva za podzemne gradnje. Dober odziv in pripravljenost sodelovanja vseh omenjenih fakultet in društev je vodila do skupne ustanovitve revije in izdaje prve številke v mesecu decembru leta 2004.

V času izdajanja revije smo se na Fakulteti za gradbeništvo v Mariboru, skupaj s prej omenjenimi ustanovitelji, spopadali s številnimi težavami, od pomanjkanja člankov in ustreznih recenzentov v začetku do tehničnih in logističnih vprašanj, ki so zadevala komunikacije z avtorji, recenzenti, lektorji in oblikovalci ter prenosi vsebin člankov med njimi. Do začetka sofinanciranja revije s strani Javne agencije za raziskovalno dejavnost RS smo ustanovitelji izdajanje revije tudi v celoti financirali. Le trmasto vztrajanje vseh sodelujočih je takrat omogočilo, da je revija dejansko zaživela in vsa leta tudi redno izhajala.

V desetih letih izdajanja revije smo dosegli veliko v začetku zastavljenih ciljev in uvedli številne spremembe. Med prvimi bi omenila že znano dejstvo, to je uvrstitev revije v Thomsonovo bazo Science Citation Index Expanded in Journal Citation Reports/Science Edition. Faktor vpliva, ki bo veljal do sredine leta 2015, je 0,455. Med spremembami bi omenila predvsem uvedbo sistema za sledenje člankov, ki omogoča pregledno komunikacijo med avtorji, recenzenti, uredniki, lektorjem ter oblikovalcem vsebin, kar je vsem močno olajšalo delo. Slednje je bilo nujno tudi zato, ker se je v zadnjih letih število prispevkov močno povečalo.

V uredništvu revije smo seveda zelo veseli velikega odziva avtorjev, saj nam to omogoča izbor najboljših člankov. Vendar smo zaradi tega prisiljeni zavračati tudi tiste prispevke, ki bi bili zanimivi in vredni objave. Iz tega razloga smo že v preteklem letu razmišljali o izdaji več številk revije letno, vendar pa trenutni finančni okvirji tega ne dopuščajo. V nasprotnem primeru bi morali avtorji prevzeti del bremen financiranja revije, s čimer pa bi omejili njihove možnosti objavljanja.
Iz tega razloga smo se odločili, da ostajamo pri izdaji dveh številk revije na leto s tem, da smo skupno število člankov povečali na 12.

Zamenjava glavnega urednika revije vedno prinese s seboj tudi nekatere spremembe. Med njimi bi omenila, da smo v tem letu razširili Uredništvo revije. Pridružila sta se prof.dr. Jakob Likar z Naravoslovnotehniške fakultete in izr.prof.dr. Janko Logar s Fakultete za gradbeništvo in geodezijo Univerze v  Ljubljani. Oba sta od samega začetka aktivno sodelovala pri izdajanju revije in veliko pripomogla k njeni kvaliteti in prepoznavnosti. Prav tako dopolnjujemo tudi Uredniški odbor. Kljub temu, da smo v preteklih letih uspeli pritegniti številne eminentne člane v ta odbor, zahtevajo nove vsebine prispevkov vključevanje novih strokovnjakov. Tako smo letos medse že povabili  dr. Svetlano Melentijevic, višjo svetovalko v družbi Rodio Kronsa, S.L., Soletanche-Bachy Group, ki je strokovnjakinja za mehaniko hribin. Veseli smo, da se nam je pridružila.

V tem letu smo se vključili tudi v Digitalno knjižnico Slovenije - dLib.si, to je spletni portal za prost on-line dostop do različnih digitalnih vsebin (http://www.dlib.si). Na tem mestu lahko najdete članke, objavljene v revijah AGS od leta 2006 dalje. Vsi prispevki od začetka izhajanja revije pa so prosto dostopni tudi na spletni strani revije (http://www.fg.uni-mb.si/journal-ags/).

Kot nova glavna urednica revije Acta Geotechnica Slovenica se bom trudila upravičiti izkazano zaupanje.

Bojana Dolinar
Glavna urednica

# EDITORIAL

At the start of 2014, I was appointed as the new editor-in-chief by the members of the Editorial Board of Acta Geotechnica Slovenica, and thus I replaced the long-time editor-in-chief Prof. Dr Ludvik Trauner, who held this position for 10 years, from the date of the first publication of our journal.

My work on the journal's publication also started in 2004, when it was first designed. Back then the members of the Chair of Geotechnics of the Faculty of Civil Engineering University of Maribor, under the leadership of Prof. Dr Ludvik Trauner, informed colleagues from the Faculty of Civil and Geodetic Engineering and the Faculty of Natural Sciences and Engineering, University of Ljubljana, as well as the members of Slovenian Geotechnical Society and the Slovenian Society for Underground and Geotechnical Constructions about the idea of publishing a Slovenian geotechnical journal. The positive response and the readiness for cooperation from all the mentioned faculties and societies led to the common foundation of the journal and publication of the first issue in December 2004.

In these years of publication, the Faculty of Civil Engineering in Maribor and the above-mentioned co-founders, have dealt with many problems, from a lack of articles and suitable reviewers in the beginning to technical and logistics issues, referring to communication with authors, reviewers, proofreaders and designers and the transfer of the article contents between them. The founders also completely financed the publication of the journal until the Slovenian Research Agency began to co-finance it. Only the stubborn persistence of all the participants enabled the journal to get off the ground and to be published regularly.

In this period we have reached many goals, set at the beginning, and also introduced various changes. In the first place I would like to point out the already-known fact that our journal is placed in Thomson's database Science Citation Index Expanded in Journal Citation Reports/Science Edition. The impact factor, valid until the middle of 2015, is 0.455. Then I would like to mention the introduction of the article-tracking system that enables the transparent communication between authors, editors, reviewers, proofreaders and content designers, which makes their work easier. Such a system was also necessary because the number of articles has increased substantially in recent years.

So, our Editorial Board is very happy to have great responses from the authors, because it enables us to choose the best articles. However, this means that we are forced to refuse some contributions that are interesting and worthy of publication.  Last year we were thinking about increasing the number of issues per year, but our financial framework unfortunately does not permit it. Otherwise, the authors would have to co-finance the journal's publication, so the opportunities to publish their articles would be limited. This is the reason why we decided to keep to two issues a year and enlarge the common number of articles to 12.

A change in the editor-in-chief always brings some modifications. First, I would like to mention that two co-editors, Prof. Dr Jakob Likar from the Faculty of Natural Sciences and Engineering and Assoc. Prof. Dr Janko Logar from the Faculty of Civil and Geodetic Engineering, University of Ljubljana, joined us this year. Both have been actively working on the journal's publication from the beginning and contributed greatly to its quality and recognition. Second, we are expanding our Editorial board. Even though we already involved many eminent members on the board in previous years, new contents of articles demand new experts. So we invited Dr Svetlana Melentijevic, a principle adviser in the company Rodio Kronsa, S.L., Soletanche-Bachy Group, who is an expert on rock mechanics. We are glad that she has joined us.

Third, we entered the Digital Library of Slovenia – dLib.si this year, which is an Internet service allowing free access to various digitalized material (http://www.dlib.si). Here you can find articles, published in AGS journals since 2006. All the contributions are also freely accessible on the journal's webpage (http://www.fg.uni-mb.si/journal-ags/).

As the new editor-in-chief of Acta Geotechnica Slovenica I will strive to justify the trust placed in me.

Bojana Dolinar
Editor–in–chief

# NUMERIČNA SIMULACIJA PIT TESTA NA POŠKODOVANIH PILOTIH

MLADEN ĆOSIĆ, BORIS FOLIĆ in RADOMIR FOLIĆ

## o avtorjih

Mladen Ćosić
University of Belgrade,
Faculty of Civil Engineering
Marka Milanovića 17, 15300 Loznica, Srbija
E-pošta: mladen.cosic@ymail.com

Boris Folić
University of Belgrade,
Faculty of Mechanical Engineering
E-pošta: boris.folic@gmail.com

Radomir Folić
University of Novi Sad,
Faculty of Technical Sciences
E-pošta: folic@uns.ac.rs

## izvleček

*V prispevku je prikazan in razvit diskretni numerični 2D in 3D trdninski model pilotov s prekinitvami in napakami, namenjen simulaciji ne-destruktivnega testiranja z uporabo PIT (pile integrity test). Modeliranje prekinitev in napak v pilotih je bilo izvedeno z redukcijo posebnih končnih elementov in modula elastičnosti betona. Analiza odgovora širjenja valov v pilotih je bila izvedena na podlagi postopne numerične integracije z uporabo metode Hilber-Hughes-Taylor v časovni domeni. Originalno je opredeljen koncept analize odgovora sistema z integracijo posameznih reflektogramov v ploskev reflektograma, ki je generirana v 3D cilindričnem koordinatnem sistemu. Z uporabo ploskev reflektograma je mogoče razumeti širjenje valov s pomočjo hitrosti, ki je na višjem nivoju kot je običajno za standardne, eno-dimenzionalne reflektograme. Spremembe odzivov hitrosti na reflektogramu, ki se spreminjajo iz pozitivne v negativno vrednosti, kažejo na lokacijo prekinitev in napak diskretnega 3D modela pilotov. Pri tem obstaja jasna razlika v reflektogramih v odvisnosti od položaja merilnega mesta. Študija definira tipološke modele reflektograma: pilot brez prekinitev in napak, napaka glave pilota, napaka v sredini dolžine pilota oziroma zmanjšani modul elastičnosti v sredini dolžine pilota, napaka noge pilota oziroma zmanjšani modul elastičnosti v območju noge pilota ter zmanjšani modul elastičnosti v območju glave pilota.*

## ključne besede

ploskev reflektograma, numerični model pilota, trdninski končni elementi

# NUMERICAL SIMULATION OF THE PILE INTEGRITY TEST ON DEFECTED PILES

### MLADEN ĆOSIĆ, BORIS FOLIĆ and RADOMIR FOLIĆ

## about the authors

Mladen Ćosić
University of Belgrade,
Faculty of Civil Engineering
Marka Milanovića 17, 15300 Loznica, Serbia
E-mail: mladen.cosic@ymail.com

Boris Folić
University of Belgrade,
Faculty of Mechanical Engineering
E-mail: boris.folic@gmail.com

Radomir Folić
University of Novi Sad,
Faculty of Technical Sciences
E-mail: folic@uns.ac.rs

## Abstract

*This paper deals with the development of a discrete numerical 2D and 3D solid pile model with a discontinuity and defects to simulate non-destructive testing using the pile integrity test (PIT). The pile discontinuity and defects were modelled by reducing the specific finite elements and the elastic modulus of concrete. The wave-propagation response of the pile was analyzed based on a step-by-step numerical integration using the Hilber-Hughes-Taylor (HHT) method in the time domain. The concept of a system-response analysis was originally formulated based on the integration of individual reflectograms into a reflectogram surface, which is generated in a 3D cylindrical coordinate system. The use of reflectogram surfaces enables an understanding of wave propagation based on their velocity to a higher level than is usually the case with standard, one-dimensional reflectograms. Changes in the velocity responses on the reflectogram, shifting from a positive to a negative value, point to the locations of discontinuities and defects in the discrete 3D pile model, and there is a clear difference in the reflectograms, depending on the position of the measuring point. The study defines the typological models of the reflectogram: without discontinuities and defects, pile-head defect, defect in the middle of the pile length or a reduced modulus of elasticity in the middle of the pile length, pile-base defect or reduced modulus of elasticity in the pile-base zone and reduced modulus of elasticity in the pile-head zone.*

## keywords

reflectogram surface, numerical pile model, solid finite elements

## 1 INTRODUCTION

Dynamic non-destructive testing (NDT) methods are usually accompanied by low stress and strain states in the pile in the linear-elastic behaviour of a material. The pile integrity test (PIT) is a fast and reliable method, mostly used for evaluating the condition of the pile in the soil. It is based on the reflection of the waves emitted from the pile head towards the pile toe. The quality and integrity of the placed pile is identified by verifying the actual length and diameter of the pile, its discontinuities, defects and damages. However, despite the proven reliability of the PIT test, there are a number of issues regarding this method, such as the effect of the propagation of the emitted waves through the pile at different levels and models of the discontinuities and defects. In [1] the authors describe a special method for monitoring the dynamic pile-testing sensors, based on strain tensors, installed inside the pile body. The results of the measured experimental investigation are compared with a numerical study of the pile and soil model in the software PLAXIS. The specific aspects of measuring the strains of the pile in the interaction with the ground for dynamic testing, where the sensors are fixed to the expansion-reinforcing bars, are shown in the paper too [2]. In addition to testing the piles in real conditions using the PIT test, tests can be conducted based on simulating analytical and numerical methods, such as the finite-element method (FEM). In [3], the numerical modelling of a tube system pile is discussed using 3D solid finite elements, while the pile defects were simulated with a series of PIT tests based on changes in the pile-wall thickness and in the Young's elastic modulus. A numerical analysis using the PIT simulation and the wave propagation through the pile and the soil is described in [4] and [5] using the CEFIT software.

The pile integrity using the PIT simulation and artificial neural networks (ANNs) was tested in [6]. Unlike the aforementioned studies, paper [7] describes the numerical aspects of resolving the wave equation for a pile using the MAPLE, ANSYS and WEAP 87 software.

This paper summarizes the theoretical basis for the treatment of wave propagation in piles with and without a discontinuity when using the PIT. The defects were identified based on processing the reflectograms that were subsequently integrated into a single response using the reflectogram surface, originally introduced in this study. The discontinuity and defects in the pile were modelled using a NDT simulation and 3D solid finite elements. This allowed the defects in the pile to be presented in a more detailed manner by eliminating some of the solid finite elements. The aspects of wave propagation in the pile were considered for various angles of impacts, while specific solutions were subsequently processed and integrated into the 3D response model.

## 2 TREATING WAVE PROPAGATION IN THE PILE USING THE PIT

The PIT is based on the principle of the induction, propagation, reflection, refraction and reception of waves in the pile. Waves, as external excitation, are caused by using a striking hammer. Upon the initiation, the wave expands (propagates) through the pile from its head towards the toe and vice versa. The effect of reflection occurs at the interface of two different media – in this case, at the pile toe-soil surface where the wave propagates towards the pile head. If the wavelength is longer than or equal to the pile diameter, then the wave propagation through the pile may be considered using the one-dimensional wave-propagation theory in a solid medium [8]. The one-dimensional wave equation (along the $x$) is:

$$\frac{\partial^2 u}{\partial t^2}=v^2\frac{\partial^2 u}{\partial x^2}\ , \qquad (1)$$

while the general solution of this equation is as follows:

$$u(t)=u_1(x-vt)+u_2(x+vt)\,. \qquad (2)$$

where $v$ is the wave velocity, $u$ is displacement, and $t$ is time. The velocity of propagation of longitudinal waves in a solid medium $v$ is a function of the given medium's material properties and is determined by:

$$v=\sqrt{\frac{E}{\rho}}\ \text{ or }\ v=\sqrt{\frac{E(1-\mu)}{\rho(1+\mu)(1-2\mu)}}\ , \qquad (3)$$

where $E$ is the Young's modulus, $\rho$ is the bulk weight, and $\mu$ is the Poisson's ratio. For simpler systems and contour conditions, the solution for Equations (1) can be obtained in a closed form; however, more complex pile models with discontinuities and defects require the use of the finite-element method.

The dynamic load applied to the pile head is a sinus function, while only half of the sine wave is taken into consideration [9]:

$$p=p_0\sin\omega t\ \text{ for }\ 0\le t\le\frac{T}{2}\ , \qquad (4)$$

where $T$ is the vibration period of the external excitation. The expression that defines the relationship between the wavelength $\lambda$, the wave-propagation velocity $v$ and the frequency $f$ is as follows:

$$\lambda=\frac{v}{f}\ . \qquad (5)$$

The time $t$ required for the wave to travel through the pile is measured from the moment of initiation by an external excitation, throughout its propagation through the pile, reflection at the toe and its return to the pile head. Changes in the wave propagation through the pile over time are displayed in a reflectogram (reflect signal). The pile length $L$ is determined, based on the reflectogram, according to [10]:

$$L=\frac{vt}{2}\ . \qquad (6)$$

The wave-propagation velocity through the pile is estimated using an accelerometer. The resulting accelerogram is then further corrected (amplified and filtered), integrated and presented over the change in the wave-propagation velocity through the pile. The pile length in the soil is determined for a time interval $[t_1,t_2]$, where the initiation of waves in the pile head corresponds with the peak velocity $v_1$, while the reflected wave in the pile head corresponds with the peak velocity $v_2$.

The shape of the reflectogram is significantly influenced by the material properties of the pile, and also influenced by the effects of wave reflection and refraction at the pile-soil interface. Depending on the soil strength, and the quality and type in the pile-toe zone, the reflected signal can have either a positive or a negative value. If the soil in the pile-toe base is very stiff, then the reflected signal is negative; if the stiffness of this soil is low, then the reflected signal is positive [11]. Due to the friction that occurs at the pile mantle-soil interface, the reflected wave can be of a smaller magnitude, resulting in problems with the interpretation of the reflectogram in the case of extremely long piles.

## 3 TREATING WAVE PROPAGATION IN A PILE WITH DISCONTINUITIES

A pile-integrity analysis is based on the one-dimensional wave-propagation theory. Wave reflection, generated by the impedance *Z* changing (discontinuity), extends all the way to the pile head, where the reflectogram records these changes. The changes in the reflectogram generally occur due to changes in the pile toe, changes in the pile diameter along its mantle, as a result of a partial inclusion of the soil into the pile, cracks, due to variation in the quality of pile material and/or soil layers, and the influence of reinforcing steel in the pile (in the case of a strongly reinforced pile).

The possible variations in the response to the propagation of waves along the pile discontinuity on the reflectogram are implied by the appearance of a positive or negative wave. The existence of discontinuities and defects in the pile is reflected through changes in the velocity on the reflectogram, where the following cases are possible: "normal" pile length without discontinuities and defects (Figure 1a), problem with the pile head (Figure 1b), discontinuity or impedance reduction (Figure 1c), the pile length is shorter than designed (Figure 1d), the pile length is longer than designed (Figure 1e) and there is a deviation or there is a lack of clear wave reflection in the pile toe (Figure 1f). The option for determining the quality of a given reflectogram is to record the signal for a number of measuring points, or enter the pulse at some other suitable location on the pile head.

## 4 PROCESSING THE REFLECTOGRAM SIGNALS

Reflectogram signals are processed in order to facilitate the adjustment, presentation and interpretation of the recorded values. The processing procedures are conducted in accordance with the signal theory, i.e., amplification, filtering and analysis of Fourier of transforms. The procedure of amplification involves the amplification of either the entire reflectogram or only a part of it, based on traditional scaling or advanced techniques: linear or exponential [10]. This procedure is especially useful when amplification on the recorded reflectogram cannot be clearly identified or the magnitude of the reflected wave is reduced. If a number of minor discontinuities or defects exist along the pile, then the reflectogram contains frequency oscillations in amplitudes of discrete velocity values, which makes it difficult to determine the actual pile length, and requires filtering.

In order to minimize the filtering error, the iterative filtering technique is used, where the reflectogram peaks are gradually reduced. It is particularly useful to apply a low-pass filter that eliminates the span of higher frequencies [12]. In the low-pass filter it is possible to apply a Butterworth function that describes the principle of conservation and elimination of frequencies, while their construction is based on the transfer function. The frequency domain analysis (FDA) of the reflectogram is based on the use of the discrete Fourier transformation (DFT) [13]:

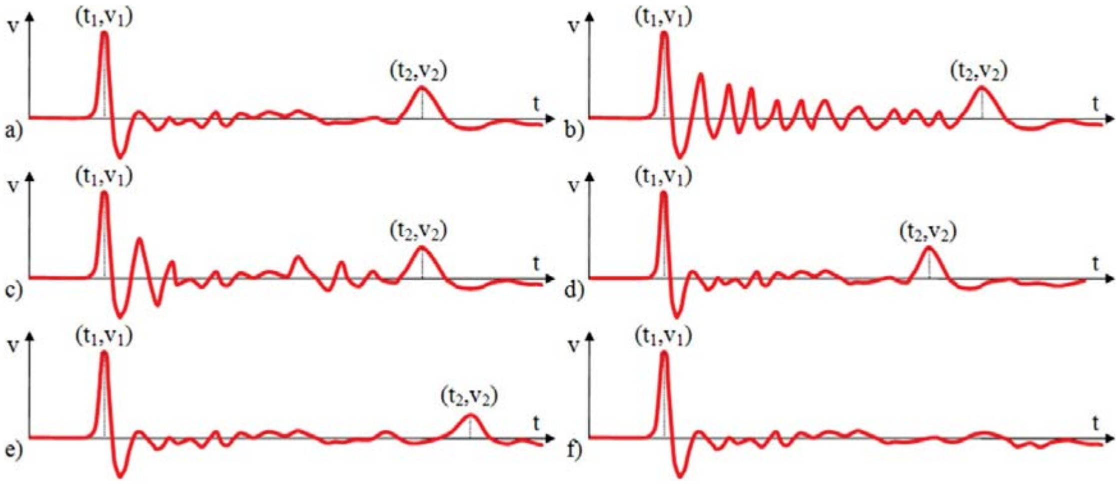

**Figure 1**. Reflectograms: a) "normal" pile length without discontinuities and defects, b) problem with the pile head, c) discontinuity in impedance reduction, d) pile length is shorter than designed, e) pile length is longer than designed, f) there is a deviation or there is a lack of clear wave reflection in the pile toe.

$$G(n)=\frac{1}{N}\sum_{k=0}^{N-1}g(k)e^{-\frac{2\pi jkn}{N}} \quad \text{for } n = 0, \ldots N\text{-}1 \,, \qquad (7)$$

$$g(n)=\sum_{k=0}^{N-1}G(k)e^{\frac{2\pi jkn}{N}} \quad \text{for } n = 0, \ldots N\text{-}1 \;. \qquad (8)$$

The frequency response realized through the Fourier transformation is presented through the Fourier amplitude spectrum (FAS):

$$amp=\sqrt{\mathrm{Re}\big(G(f)\big)^2+\mathrm{Im}\big(G(f)\big)^2} \;. \qquad (9)$$

## 5 NUMERICAL MODELLING AND ANALYSIS OF THE DISCONTINUITIES AND DEFECTS IN THE PILE

Modelling the pile and analyzing the wave propagation using the PIT simulation test can be carried out in the following ways: using the analytical method to a lumped mass model (LMM), method of characteristics (MC), finite-difference method (FDM) and the finite-element method (FEM). Using the finite-element method enables the PIT simulation test for the 1D discrete pile model with the 2D or 3D discrete soil model; for the 2D discrete pile model with the 2D discrete soil model; and for the 3D discrete pile model with the 3D discrete soil model. The above-presented options are for explicit soil modelling by using the 2D or 3D discrete model; however, it is also possible to be taken implicitly into the soil-pile interaction analysis. The present study is based on the simulation of PIT of the 3D discrete homogeneous and inhomogeneous elastic pile model with the implicitly implemented effects of pile-soil interaction. The components of soil stiffness were introduced over replacement springs, while the damping was introduced through the damping elements according to [14]:

$$k_v=2.3G_s\,, c_v=2\pi\rho_s V_s d,\, K_v=\frac{4G_s d}{1-\mu_s}, C_v=\frac{0.85K_v d}{V_s}, \qquad (10)$$

where $k_v$ is the vertical stiffness component for the pile mantle, $c_v$ is the vertical damping component for the pile mantle, $K_v$ is the vertical stiffness component for the pile toe, $C_v$ is the vertical damping component for the pile toe, $\rho_s$ is soil bulk density, $d$ is the pile diameter, $\mu_s$ is the Poisson's ratio of the soil, and $V_s$ is the shear wave propagation velocity:

$$V_s=\sqrt{\frac{G_s}{\rho_s}}\,, \qquad (11)$$

where $G_s$ is the shear modulus of the soil:

$$G_s=\frac{E_s}{2(1+\mu_s)}\,, \qquad (12)$$

and $E$ is Young's elastic modulus for the soil.

The process of determining the acceleration, velocity and displacement of the pile using the PIT is based on considering the differential equations of motion:

$$[M]\{U\}+[C]\{V\}+[K]\{D\}=\{Q\}\,, \qquad (13)$$

where $[M]$ is the mass matrix, $\{U\}$ is the acceleration vector, $[C]$ is the damping matrix, $\{V\}$ is the velocity vector, $[K]$ is the stiffness matrix, $\{D\}$ is the displacement vector and $\{Q\}$ is the vector of external loads. The Equations (13) are resolved using step-by-step numerical integration with a modified form of the Hilber-Hughes-Taylor (HHT) method [15]:

$$\begin{aligned}&[M]\{U\}_{i+1}+(1+\alpha)[C]\{V\}_{i+1}-\alpha[C]\{V\}_i+\\&\quad+(1+\alpha)[K]\{D\}_{i+1}-\alpha[K]\{D\}_i=\{Q\}_{i+\alpha}\,,\end{aligned} \qquad (14)$$

and for a moment of time:

$$t_{i+1}=t_i+\Delta t\;. \qquad (15)$$

In order to achieve a high-quality numerical solution for wave propagation both in the discrete numerical model and in the actual soil model, the length of one side of the finite element $\Delta l$ needs to be [16]:

$$\Delta l=\frac{\lambda}{10}\cdot \qquad (16)$$

Numerical modelling of the pile degradation is carried out by analyzing the pile using the staged degradation analysis (SDA). The SDA is constructed so that the pile degradation is generated and simulated by linking the individual analyses. These analyses are successively implemented using the system stiffness matrix from the end of the previous analysis of the degraded condition as the initial system stiffness matrix of the next analysis of degradation. The mathematical formulation of the SDA is derived by starting from the expression for the condition before testing the pile using the PIT:

$$t=0\text{:}\;\; [K_0]\{U_0\}=\{P_0\}\,, \qquad (17)$$

where $[K_0]$ is the non-degraded pile stiffness matrix. For the initial stage of pile degradation, the analysis is as follows:

$$\begin{aligned}&t=1\text{:}\;\; [K_1]\{U_1\}=\{P_1\},\;\; [K_1]=[K_0]-[K_0'],\\&[M_1]=[M_0]+[M_1'],\end{aligned} \qquad (18)$$

where $[K'_0]$ is the stiffness matrix of the eliminated domain of finite pile elements, $[M_0]$ is the non-degraded pile mass matrix, $[M'_1]$ is the mass matrix of the eliminated domain of finite pile elements. In the $i$-th stage of pile degradation, the analysis is conducted according to:

$$t=i\text{: } \left[K_i\right]\left\{U_i\right\}=\left\{P_i\right\},\left[K_i\right]=\left[K_{i-1}\right]-\left[K'_{i-1}\right], \\ \left[M_i\right]=\left[M_{i-1}\right]+\left[M'_i\right], \qquad (19)$$

while for the $n$-th stage the following applies:

$$t=n\text{: } \left[K_n\right]\left\{U_n\right\}=\left\{P_n\right\},\left[K_n\right]=\left[K_{n-1}\right]-\left[K'_{n-1}\right], \\ \left[M_n\right]=\left[M_{n-1}\right]+\left[M'_n\right], \qquad (20)$$

where $[K_n]$ is the pile stiffness matrix in the final stage of degradation, and $[M_n]$ is the pile mass matrix in the final stage of degradation.

## 6 DISCUSSION OF THE RESULTS OF NUMERICAL TESTING OF THE PILE DISCONTINUITIES AND DEFECTS

The numerical simulation of the non-destructive pile testing was carried out by using the SAP 2000 software [17]. Before processing the 3D model of the pile with defects, numerical analyses were carried out on a 2D pile and soil model, with each model using more than 40000 surface finite elements. Only part of the finite-element mesh for each model has been shown separately. Figure 2 shows the 2D numerical pile and soil models: model 1 - no discontinuities and defects (Figure 2a), model 2 - pile head defect (Figure 2b), model 3 - defect in the middle of the pile length (Figure 2c), model 4 - pile base (toe) defect (Figure 2d), model 5 - reduced modulus of elasticity in the pile-head zone (Figure 2e), model 6 - reduced modulus of elasticity in the mid of the pile length (Figure 2f) and model 7 - reduced modulus of elasticity in the pile base (toe) (Figure 2g). The dimensions of the pile considered in the study were $L$=15m and $d$=0.5m; regarding the quality of materials: concrete bulk mass $\rho$=2400kg/m$^3$, Young's elastic modulus of concrete $E$=30GPa, Poisson's ratio of concrete $\mu$=0.2, and the corresponding velocity of wave propagation in concrete $v$=3535.53m/s. The external impulsive load applied to the pile head is $Q$=1KN, while the sine wave oscillation period is $T$=1ms, the corresponding oscillation frequency $f$=1kHz and the wavelength $\lambda$=3.73m. The expected wave-propagation time through the pile is $t$=8.2ms. In the HHT procedure a time increment of $\Delta t$=0.01ms was used, while the total number of steps in the analysis was 1200, so that the considered time interval of the reflectogram is 12ms. All the reflectograms were filtered using a low-pass filter and a weighted-average smoothing filter to obtain a smooth response function for facilitating the interpretation of results, while avoiding the elimination of important peaks. Additionally, spline interpolation was applied to the discrete values of the reflectogram.

A parametric analysis was conducted in order to consider the impact of the changes in the modulus of elasticity of soil below the pile base and around the pile on the shape of the reflectogram. Figure 3 shows the resulting reflectograms for: model 1 - no discontinuities and defects while changing the modulus of elasticity of the soil below the pile base (Figure 3a), model 1 - no discontinuities and defects while changing the modulus of elasticity of the soil around the pile (Figure 3b),

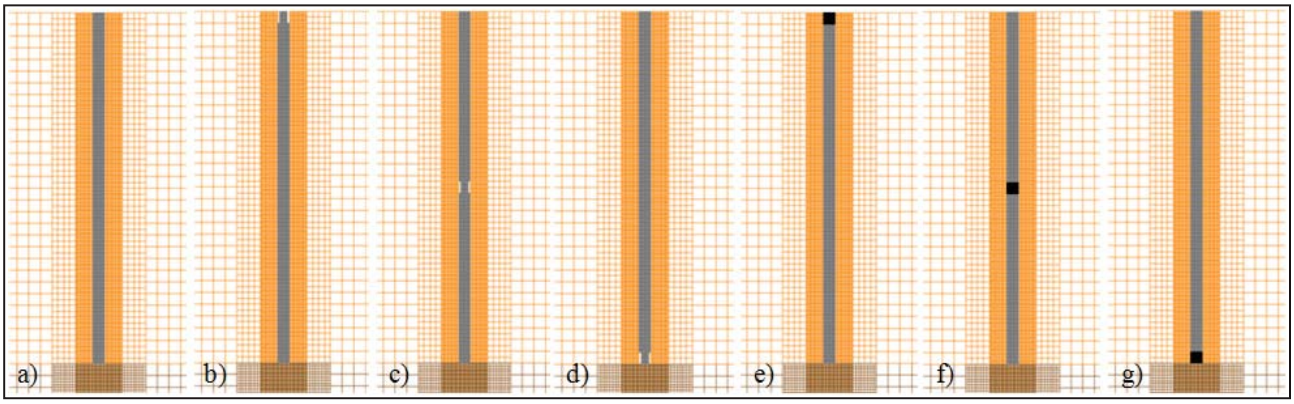

**Figure 2**. Numerical pile models: a) model 1 - no discontinuities and defects, b) model 2 – pile-head defect, c) model 3 - defect in the middle of the pile length, d) model 4 – pile-base (toe) defect , e) model 5 - reduced modulus of elasticity in the pile-head zone, f) model 6 - reduced modulus of elasticity in the middle of the pile length, g) model 7 - reduced modulus of elasticity in the pile base (toe).

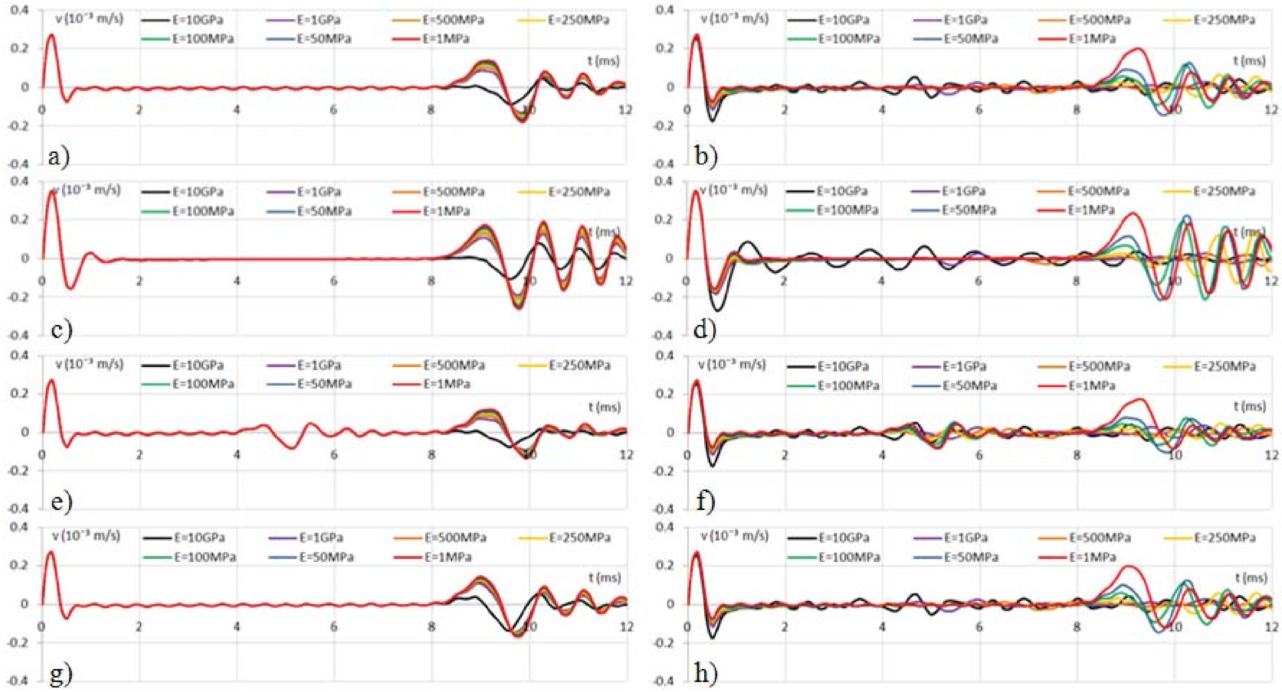

**Figure 3**. Reflectograms: a) model 1 - no discontinuities and defects while changing the modulus of elasticity of the soil below the pile base, b) model 1 - no discontinuities and defects while changing the modulus of elasticity of the soil around the pile, c) model 2 – pile-head defect while changing the modulus of elasticity of the soil below the pile base, d) model 2 – pile-head defect while changing the modulus of elasticity of the soil around the pile, e) model 3 - defect in the middle of the pile length while changing the modulus of elasticity of soil below the pile base, f) model 3 - defect in the middle of the pile length while changing the modulus of elasticity of the soil around the pile, g) model 4 - pile base (toe) defect while changing the modulus of elasticity of the soil below the pile base and h) model 4 - pile base (toe) defect while changing the modulus of elasticity of the soil around the pile.

model 2 - pile head defect while changing the modulus of elasticity of the soil below the pile base (Figure 3c ), model 2 - pile head defect while changing the modulus of elasticity of the soil around the pile (Figure 3d), model 3 - defect in the middle of the pile length while changing the modulus of elasticity of the soil below the pile base (Figure 3e), model 3 - defect in the middle of the pile length while changing the modulus of elasticity of the soil around the pile (Figure 3f), model 4 - pile base (toe) defect while changing the of modulus of elasticity of the soil below the pile base (Figure 3g) and model 4 - pile base (toe) defect while changing the modulus of elasticity of the soil around the pile (Figure 3h). Comparing the resulting reflectograms, the locations of the changes in the signal are clearly identified and they correspond to the position of the pile defects. In the case of the defect in the pile head, both positive and negative velocity values are increased in the defect area; the period of oscillation is also increased. In the case of the defect in the middle of the pile length, the signal shifts from a positive to a negative value, clearly indicating the position of the pile defect, while in the case of the pile base defect, the signal shifts its velocity value somewhat earlier. Changes in the modulus of elasticity of the soil below the pile base do not induce changes in the reflectogram, except in cases of very high values of the modulus of elasticity; in these cases the velocities are reduced. Changes in the modulus of elasticity of the soil around the pile influence the shape of reflectogram to a greater degree than the changes in the modulus of elasticity of the soil below the pile base. In this case, when increasing the modulus of elasticity of the soil, and in particular at very high values of the elastic modulus, the velocity values begin to oscillate slightly at about the value of zero. However, the times for the initiation of defects in the pile are not significantly changed, which can be seen in the reflectogram for the defect in the middle of the pile length.

Figure 4 shows the resulting reflectogram for: model 1 - no discontinuities and defects while changing the modulus of elasticity of the soil below the pile base (Figure 4a ), model 1 - no discontinuities and defects while changing the modulus of elasticity of the soil

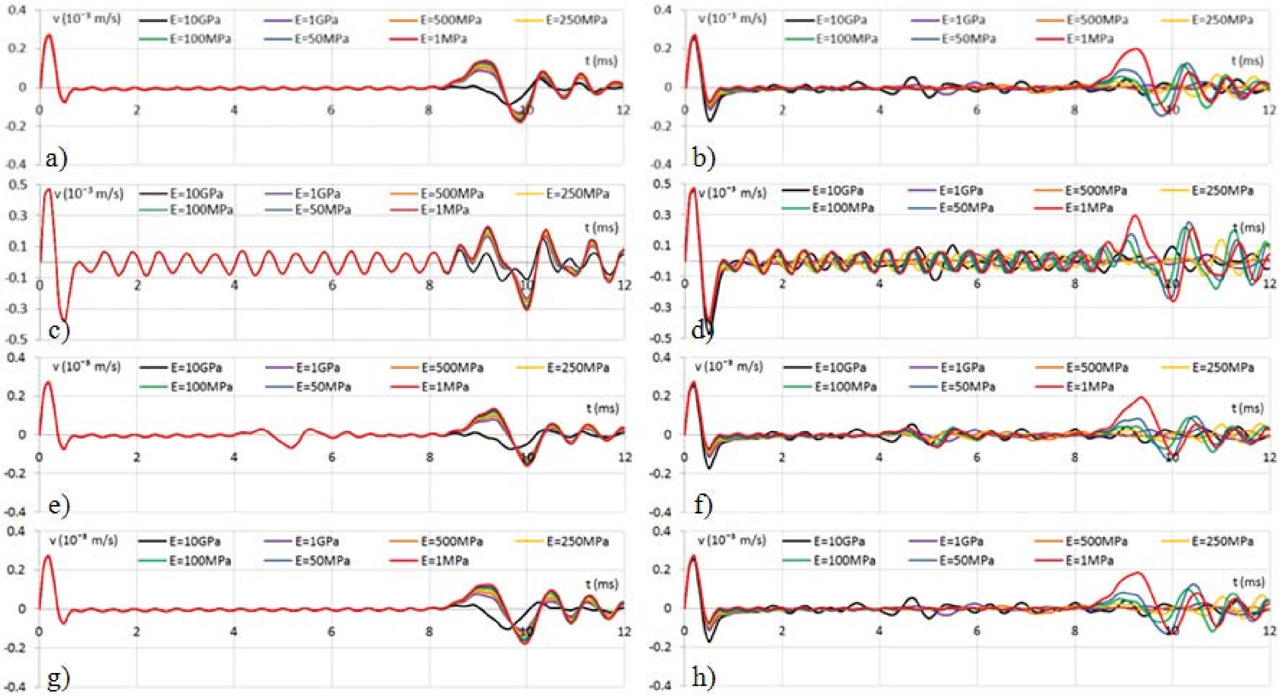

**Figure 4**. Reflectograms: a) model 1 - no discontinuities and defects pile base (toe) defect while changing the modulus of elasticity of the soil below the pile base, b) model 1 - no discontinuities and defects pile base (toe) defect while changing the modulus of elasticity of the soil around the pile, c) model 2 - reduced modulus of elasticity in the area in the pile-head zone while changing the modulus of elasticity of the soil below the pile base, d) model 2 - reduced modulus of elasticity in the pile head zone while changing the modulus of elasticity of the soil around the pile, e) model 3 - reduced modulus of elasticity in the middle of the pile length while changing the modulus of elasticity of the soil below the pile base, f) model 3 - reduced modulus of elasticity in the middle of the pile length while changing the modulus of elasticity of the soil around the pile, g) model 4 - reduced modulus of elasticity in the pile base (toe) zone while changing the modulus of elasticity of the soil below the pile base and h) model 4 - reduced modulus of elasticity in the pile base (toe) zone while changing the modulus of elasticity of the soil around the pile.

around the pile (Figure 4b), model 2 - reduced modulus of elasticity in the pile-head zone while changing the modulus of elasticity of the soil below the pile base (Figure 4c), model 2 - reduced modulus of elasticity in the pile-head zone while changing the modulus of elasticity of the soil around the pile (Figure 4d), model 3 - reduced modulus of elasticity in the middle of the pile length while changing the modulus of elasticity of the soil below the pile base (Figure 4e), model 3 - reduced modulus of elasticity in the middle of the pile length while changing the modulus of elasticity of the soil around the pile (Figure 4f), model 4 - reduced modulus of elasticity in the pile base (toe) while changing the modulus of elasticity of the soil below the pile base (Figure 4g) and model 4 - reduced modulus of elasticity in the pile base (toe) zone while changing the modulus of elasticity of the soil around the pile (Figure 4h). As in the previous case, comparing the resulting reflectograms the locations of changes in the signal are identified, and they correspond to the positions of the reduction in the modulus of elasticity of the pile. In the case of a reduction in the modulus of elasticity of the pile head, both the positive and negative velocity values are now much more increased in this area, and the period of oscillation is also increased. This results from the fact that the zone of reduction of the modulus of elasticity of concrete comprises the entire cross-section, while for the simulation of the pile defect only the cross-sectional area has been reduced. Upon the initiation of the reduction of the modulus of elasticity of the pile head, the reflectogram indicates changes in the velocity similar to a sinusoidal function. However, despite the differences in the middle of the reflectogram of the healthy pile and the pile with a reduced modulus of elasticity in its head, the time of transition of the waves from the pile base to the soil below the pile can be clearly observed. In the case of a defect in the middle of the pile length, similar to the previous case, the signal shifts from a positive to a negative value, clearly indicating the position of the pile defect, while in case of the pile base defect, the signal shifts its velocity value somewhat earlier. Changes in the modulus of elasticity of the soil below the pile base do not induce changes in the reflectogram, except in cases of very high values of the modulus of elasticity; in these cases the velocities are being reduced when the waves cross the zone between the pile base and the soil below the pile. Changes in the modulus of elasticity of the soil around the pile influence the shape of reflectogram to a greater degree than changes in the modulus of elasticity of the soil below the pile base. In this case, when increasing the modulus of elasticity of the soil, and in particular at very high values of the elastic modulus, the velocity values also begin to oscillate slightly at about a zero value for the reduced modulus of elasticity in the middle of the pile length and in the pile base zone.

Figure 5a shows the 3D pile model as generated from 3D solid finite elements, Figure 5b shows a segment of the pile cross-section. Figure 5c shows the sensor locations (positions for which the reflected waves were measured) and the central position for applying the impact loading. The values of the stiffness components are $k_v$=10$^2$N/m$^3$ and $K_v$=10$^5$N/m$^3$, and the values of the damping components are $c_v$=10Ns/m$^3$ and $C_v$=10$^4$Ns/m$^3$. Numerical modelling was considered for the model without defects and discontinuities and for seven models with varying pile discontinuities and defects: model 1 - no discontinuities and defects (Figure 6a), model 2 - asymmetric pile toe defect (elimination of specific finite elements

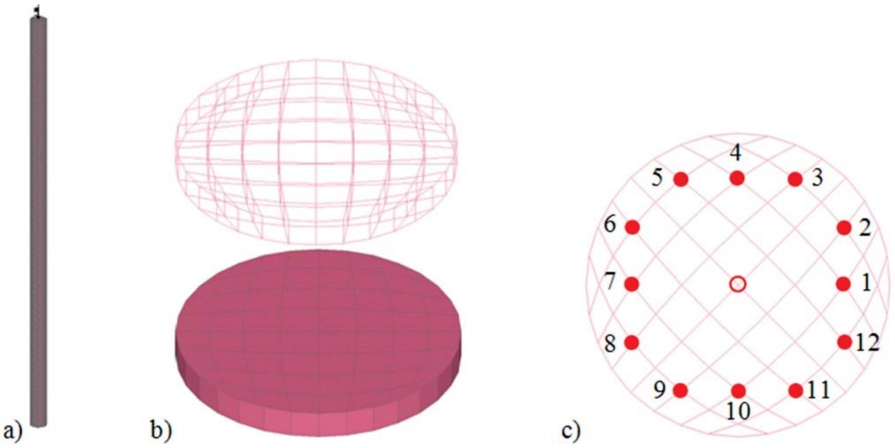

**Figure 5**. a) the 3D pile model generated from 3D solid finite elements, b) a pile segment, c) sensor locations (positions for which the reflected waves were measured) and the central position of applying the impact loading.

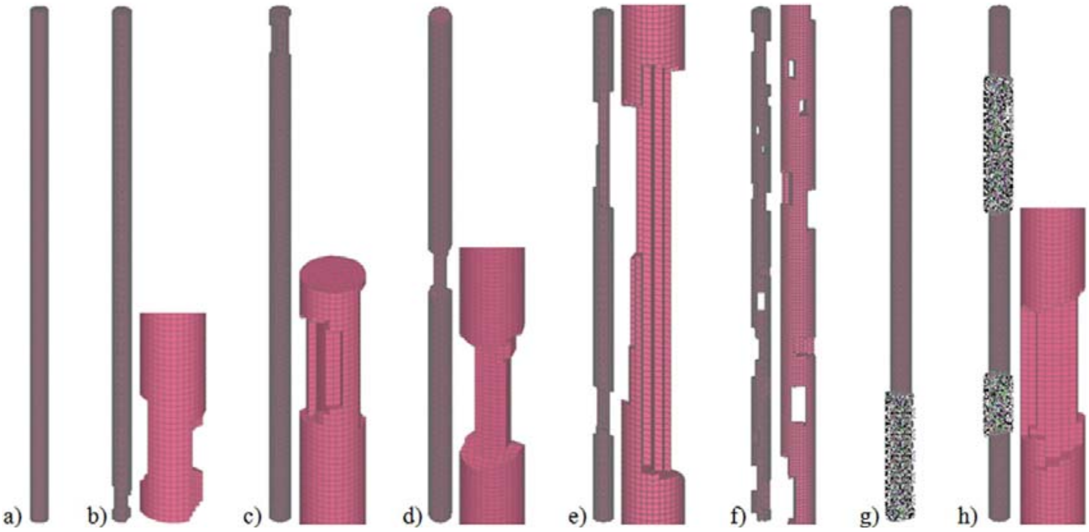

**Figure 6**. Numerical pile models: a) model 1 - without discontinuities and defects, b) model 2 - asymmetric pile-toe defect, c) model 3 - asymmetric pile-head defect, d) model 4 - asymmetric reduction of cross-section in the middle of the pile length, e) model 5 - asymmetric reduction of cross-section in two locations along the pile length, f) model 6 - significantly degraded pile along its full length, g) model 7 - different elastic modulus in pile-toe zone, h) model 8 - different elastic modulus and asymmetric reduction of cross-section in two locations along the pile.

in a length of 1m) (Figure 6b), model 3 - asymmetric pile head defect (elimination of specific finite elements in the length of 1m) (Figure 6c), model 4 - asymmetric reduction of cross-section in the middle of the pile length (elimination of specific finite elements) (Figure 6d), model 5 - asymmetric reduction of cross-section in two locations along the pile length (elimination of specific finite elements) (Figure 6e), model 6 - significantly degraded pile along its full length (elimination of specific finite elements) (Figure 6f), model 7 - different elastic modulus in the pile-toe zone (changing the elastic modulus in the length of 2m) (Figure 6g) and model 8 - different elastic modulus and asymmetric reduction of cross-section at two locations along the pile (changing the elastic modulus and eliminating specific finite elements) (Figure 6h).

**Table 1**. Parameters of numerical pile models.

| model | nodes | solid FE | no. of system equilibrium equations | degrees of freedom of the system masses |
|---|---|---|---|---|
| 1 | 24381 | 19200 | 87786 | 73143 |
| 2 | 24131 | 18784 | 87036 | 71955 |
| 3 | 23621 | 18348 | 84954 | 70551 |
| 4 | 22963 | 17891 | 82263 | 68880 |
| 5 | 21095 | 15032 | 77928 | 60009 |
| 6 | 20991 | 14141 | 77616 | 59193 |
| 7 | 24381 | 19200 | 87786 | 73143 |
| 8 | 21095 | 15032 | 77928 | 60009 |

Table 1 shows the parameters of the numerical pile models. The appropriate wave-propagation time $t$=8.3ms and the appropriate pile length $L$=15.4m for the pile without discontinuities and defects (model 1) were identified using the finite-element method. The upper part of Figure 7 shows a reflectogram of the 3D solid pile model without a discontinuity (model 1) from the numerical analysis, while the lower part of Figure 7 shows the corresponding analytical solution obtained from Equation (6). There is a remarkable agreement for the wave-propagation times through the pile in both applied methods. In addition to the reflectogram-based considerations regarding the pile responses, the Fourier amplitude spectrum (FAS) was also applied. After the pile responses were considered based on the use of reflectograms at 12 measuring locations, the same was carried out along the 12 independent reflectograms for each pile model. These reflectograms were subsequently integrated into a single response using the reflectogram surfaces originally introduced in this study. The reflectograms were first considered in a 2D plane coordinate system and then transformed into a 2D polar coordinate system, while their final form was reached by transforming them into a 3D cylindrical coordinate system. The angle increment in the cylindrical coordinates is $\Delta\theta$=30°. The location of the pile defect and the corresponding reduction in the modulus of elasticity were identified, among the others, on the basis of the differences in the velocity of the reflectogram of the damaged $v(t)_d$ and the healthy pile $v(t)_0$.

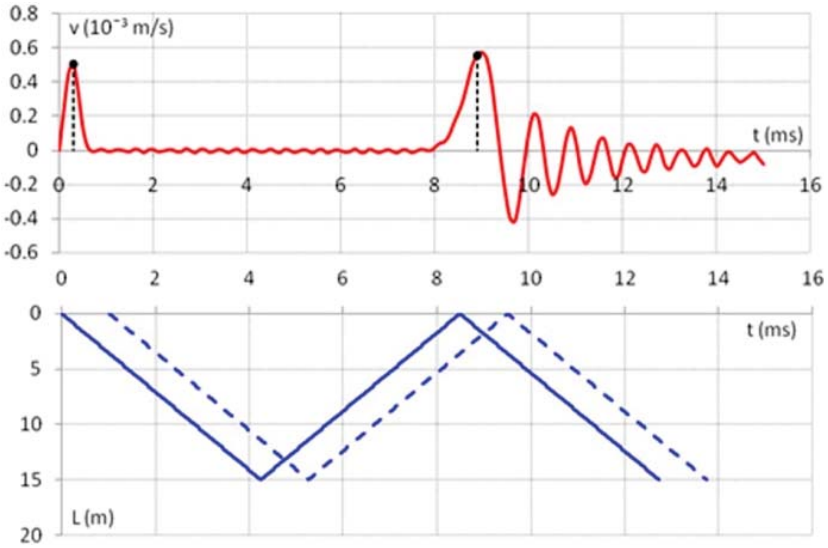

**Figure 7**. Reflectogram of the 3D solid pile model without discontinuities (model 1) and the corresponding analytical solution.

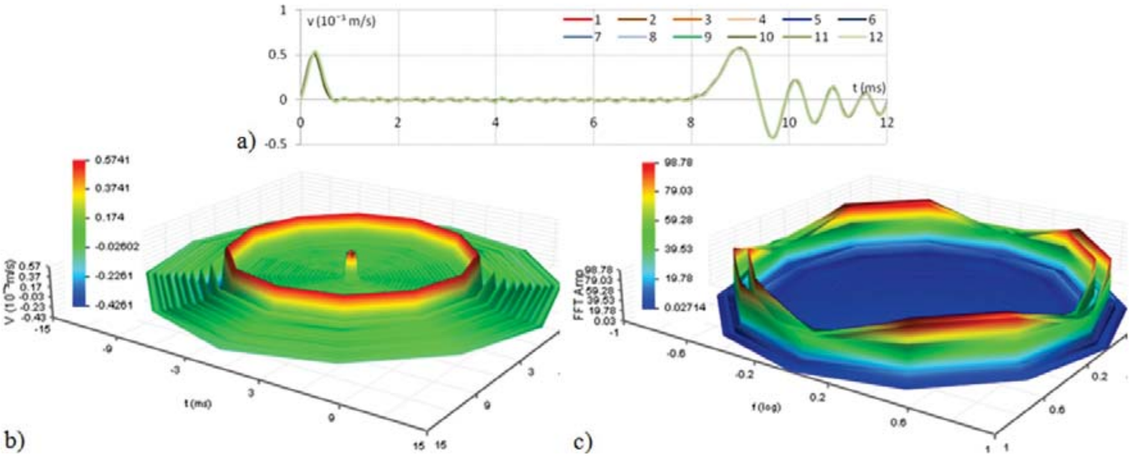

**Figure 8**. Numerical model of pile 1 - without discontinuities and defects: a) reflectograms, b) the 3D reflectogram surface, c) the 3D FAS spectrum surface.

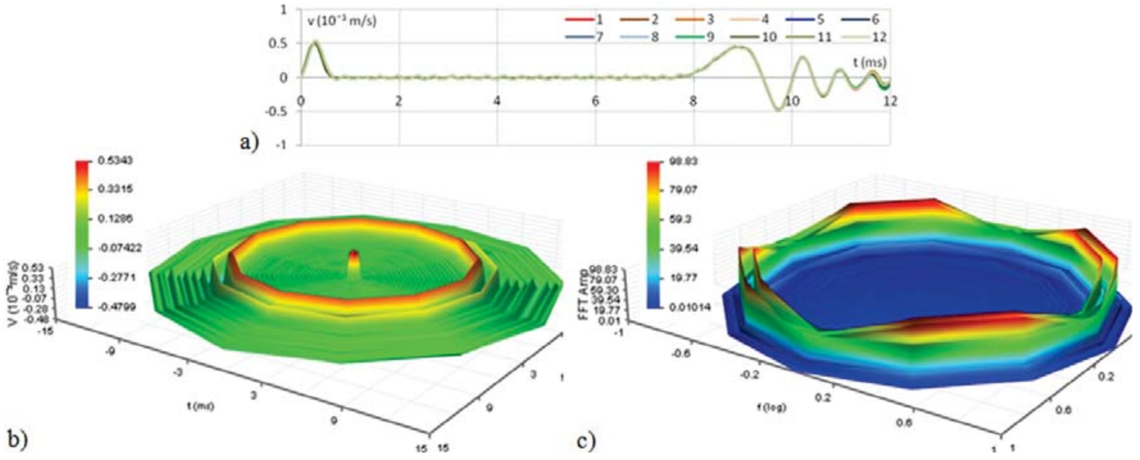

**Figure 9**. Numerical model of pile 2 - asymmetric pile-toe defect: a) reflectograms, b) the 3D reflectogram surface, c) the 3D FAS spectrum surface.

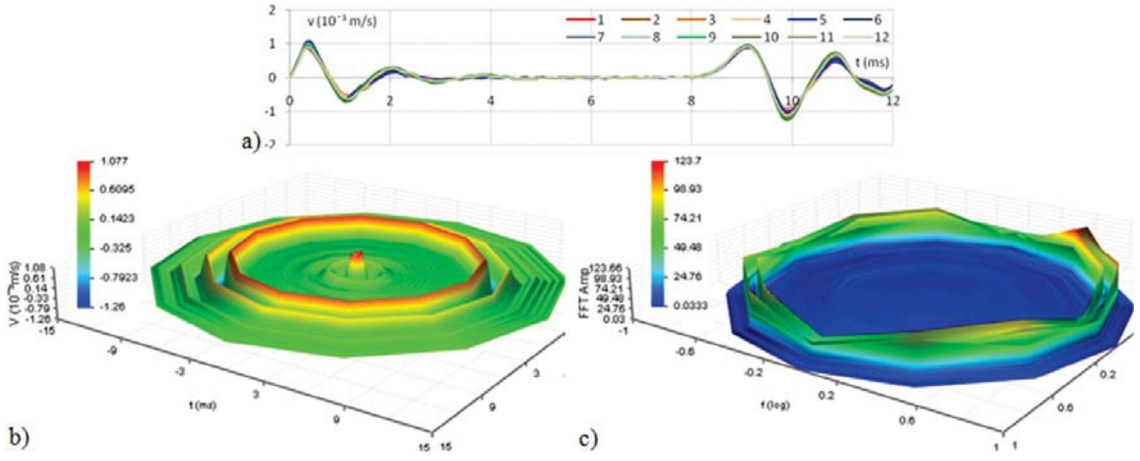

**Figure 10**. Numerical model of pile 3 - asymmetric pile-head defect: a) reflectograms, b) the 3D reflectogram surface, c) the 3D FAS spectrum surface.

Figures 8 to 15 show the reflectograms, the 3D reflectogram surfaces and the 3D surfaces of the FAS response spectrum for all eight pile models under consideration. All the reflectograms achieved in model 1 are identical, since the pile is without any discontinuities and defects, so that the reflectogram surface is an ideal rotationally symmetric surface (Figure 8). Almost identical reflectograms were also achieved in model 2, given the minimum asymmetry defect of the pile toe (Figure 9). On the other hand, since the pile toe defect was simulated based on the reduction of solid finite elements along the pile mantle near the toe, the central part of the pile remained intact, so that the waves were propagating and reflecting with minimum reduction, making the model 2 reflectograms similar to the model 1 reflectograms, except for the reduced wave-propagation velocity in the pile-toe zone. In model 3 with the asymmetric pile-head defect, the wave propagation through the pile head was identified using a reflectogram based on the response rate shifting from a negative to a positive value (Figure 10). The length at which the reflectogram located the defect is $l=0.5v(t_1-t_0)=1.1$m, obtained from Equation (6), while the modelled defect length is 1m, while the level of agreement between the simulated PIT results and the numerical model results is obviously satisfactory. The length obtained based on the model 4 reflectogram with the asymmetric reduction of the cross-section in the middle of the pile length is $l=0.5v(t_2-t_1)=1.3$m, which corresponds to the length of the simulated discontinuity zone (Figure 11). In this model, the initiation and termination of the discontinuity zone are accompanied by shifting the velocity value in the middle of the pile length from positive to negative. The positive velocity value corresponds to the initiation of a discontinuity

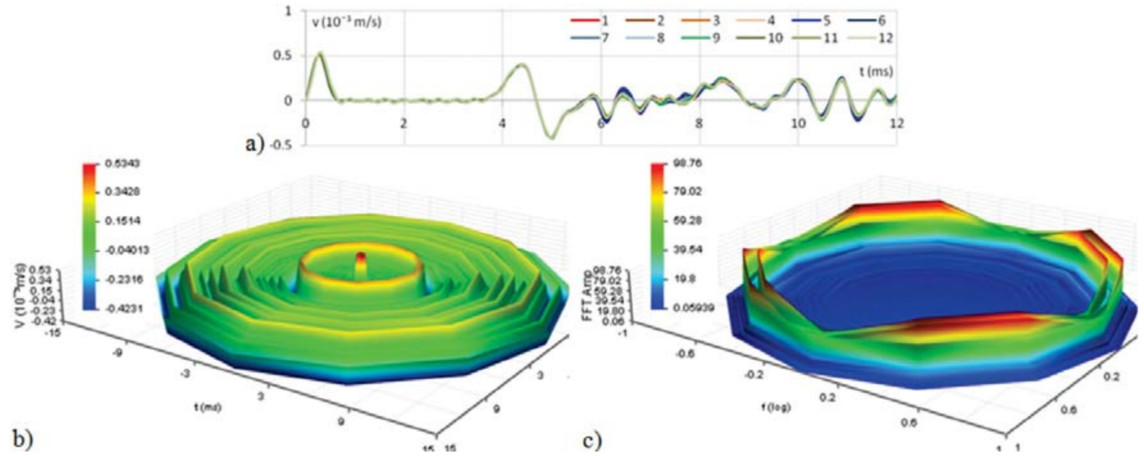

**Figure 11**. Numerical model of pile 4 - asymmetric reduction of cross-section in the middle of the pile length: a) reflectograms,b) the 3D reflectogram surface, c) the 3D FAS spectrum surface.

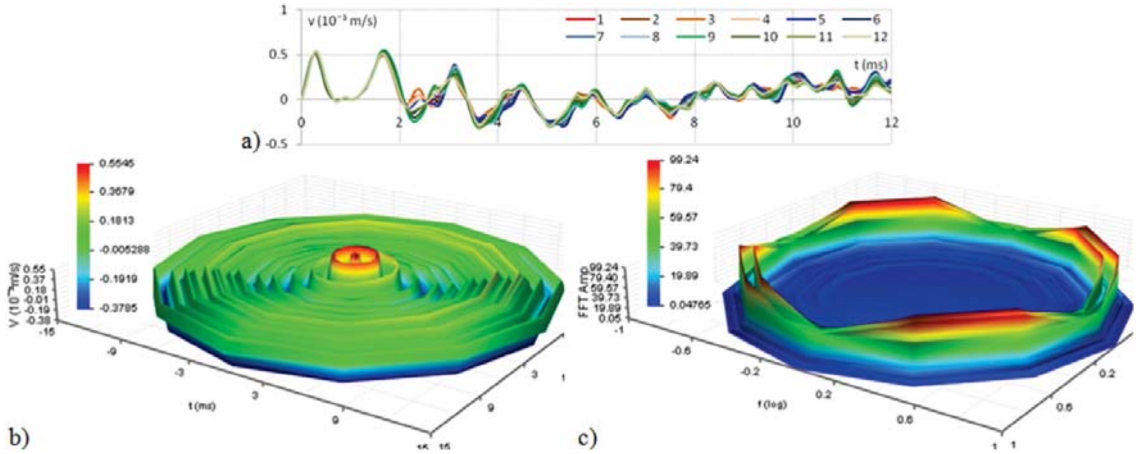

**Figure 12**. Numerical model of pile 5 - asymmetric reduction of cross-section in two locations along the pile length: a) reflectograms, b) the 3D reflectogram surface, c) the 3D FAS spectrum surface-

zone, while the negative velocity value corresponds to the termination of the discontinuity zone. In model 5 with an asymmetric reduction of the cross-section in two locations along the pile length the reflectogram identified the first discontinuity (Figure 12) as follows $l=0.5v(t_2-t_1)=2.4$m, while the length of the second discontinuity is $l=0.5v(t_4-t_3)=1.5$m. The reflectograms of this pile model are not all identical, due to the asymmetric and uneven discontinuities and defects, making the larger number of velocity shifts from the positive to the negative values obvious. There is an additional velocity shift on the transition between the two pile discontinuities, which is a consequence of the substantial irregularity of the discontinuities, as also evidenced by the reflectogram response for the diagonal measuring locations. The reflectograms obtained for the model 6 pile (with a significant degradation along the full pile length) vary significantly, depending on the position of the measuring location (Figure 13). The defects in this pile were modelled based on the principle of the stochastic modelling of defects in the concrete, resulting in frequent changes of velocity on the reflectogram. In the case when the actual pile model results in this type of reflectogram, further pile strengthening is recommended or the pile needs to be replaced due to reduced capacity, stability, usability and durability. The model 7 is characterized by a different elastic modulus in the pile-toe zone, where the wave-propagation velocity is $v=2635.23$m/s (Figure 14). This velocity is typical of poor-quality concretes; it is also typical for piles significantly degraded in the toe zone. The reflectogram is featured by the reduced wave velocity in the pile, which is a direct consequence of the different elastic modulus

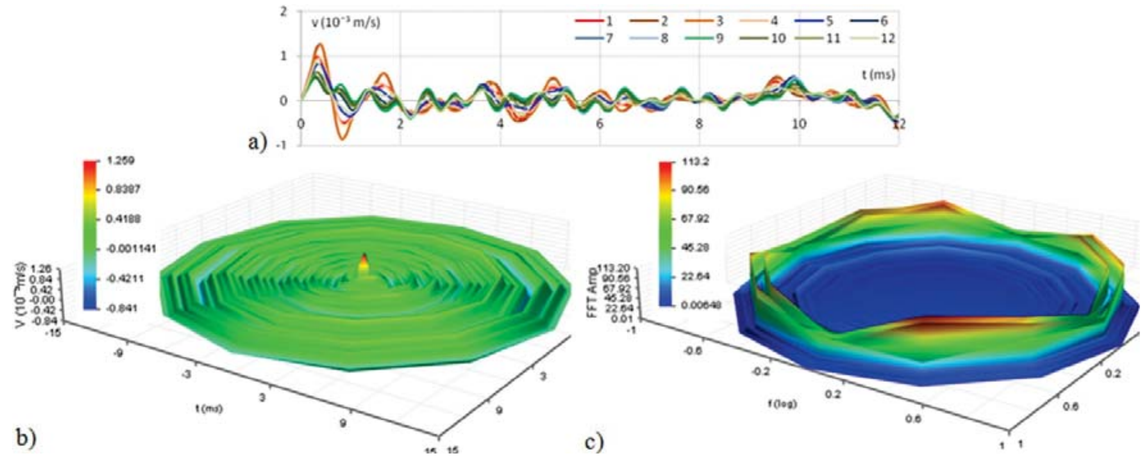

**Figure 13**. Numerical model of pile 6 - significant degradation along the full pile length: a) reflectograms, b) the 3D reflectogram surface, c) the 3D FAS spectrum surface.

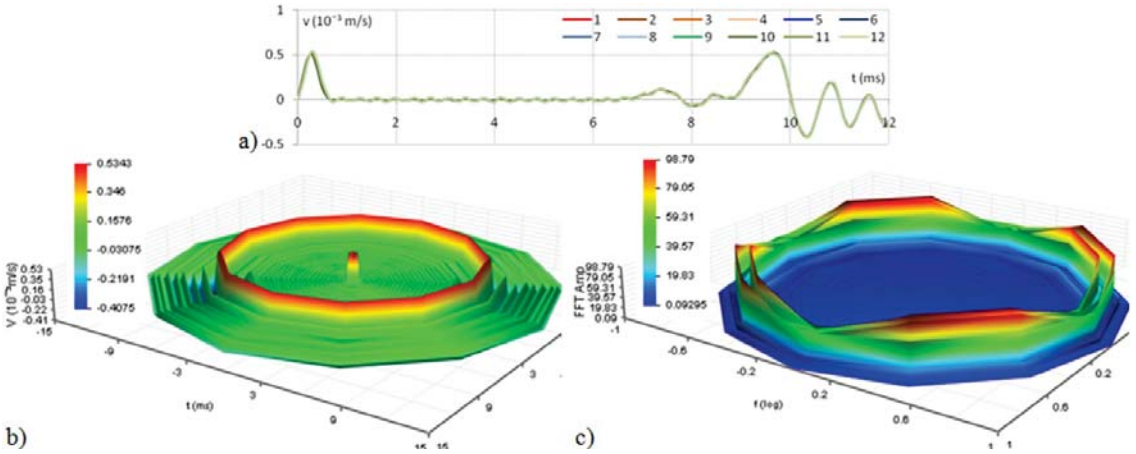

**Figure 14**. Numerical model of pile 7 - different elastic modulus in the pile toe zone: a) reflectograms, b) the 3D reflectogram surface, c) the 3D FAS spectrum surface.

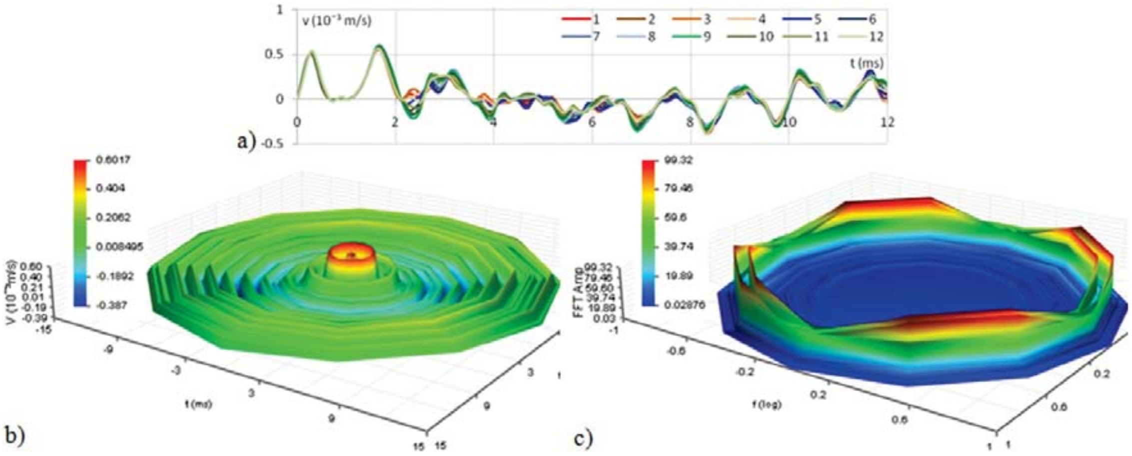

**Figure 15**. Numerical model of pile 8 - different elastic modulus and asymmetric reduction of cross-section in two locations along the pile length: a) reflectograms, b) the 3D reflectogram surface, c) the 3D FAS spectrum surface.

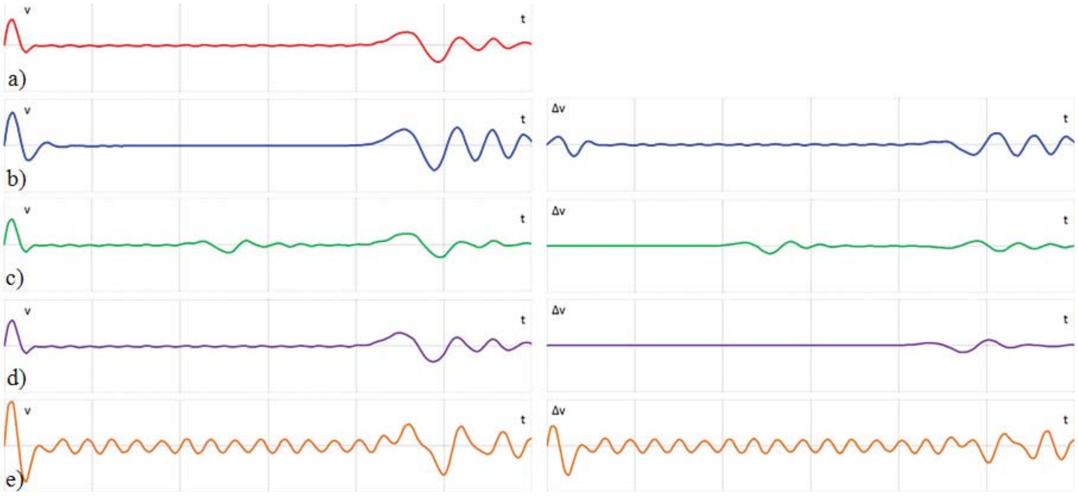

**Figure 16**. Reflectogram (left) and reflectograms obtained as the velocity difference $\Delta v$ between the damaged $v(t)_d$ and the healthy pile $v(t)_0$ (right): a) no discontinuities and defects, b) pile-head defect, c) defect or reduced modulus of elasticity in the middle of the pile length, d) pile-base defect or reduced modulus of elasticity in the pile base zone, e) reduced modulus of elasticity in the pile head zone.

at this location. The zone of the reduction of the elastic modulus is initiated between lengths of 12.9 and 15m, where the reflectogram contains a change in the sign of the velocity. In model 8 with different elastic modulus and an asymmetric reduction of the cross-section in two locations along the pile length, there is a significant difference in the system response presented by the reflectograms (Figure 15). In the first part, up to the initiation of the reduction of the cross-section, the reflectograms are all identical, but along with the propagation of waves through the zone of discontinuity the nature of the response at the measuring locations is stochastic.

The typology of the reflectograms was conducted in order to facilitate the identification of the pile damage. Figure 16 shows the general reflectogram models (left) and the reflectograms obtained as the velocity differences $\Delta v$ between the damaged $v(t)_d$ and healthy pile $v(t)_0$ (right): without discontinuities and defects (Figure 16a), pile-head defect (Figure 16b), defect or reduced modulus of elasticity in the middle of the pile length (Figure 16c), pile-base defect or reduced modulus of elasticity in the pile-base zone (Figure 16d), and reduced modulus of elasticity in the pile-head zone (Figure 16e).

## 7 SUMMARY AND CONCLUSIONS

This paper describes the development of discrete numerical 2D and 3D solid pile models with a discontinuity and defects to simulate the non-destructive testing using the pile integrity test (PIT). The pile discontinuity and defects were modelled by reducing the specific finite elements and using the staged degradation analysis (SDA). The effect of the degradation of the pile concrete quality is introduced through the reduction of the elastic modulus in specific zones. The wave-propagation response of the pile was analyzed based on a step-by-step numerical integration using the Hilber-Hughes-Taylor (HHT) method in the time domain. The concept of the system response analysis was originally formulated based on the integration of individual reflectograms into a reflectogram surface, which is generated in a 3D cylindrical coordinate system.

In addition to the pile without discontinuities and defects, seven different models of pile discontinuities and defects were considered: asymmetric pile toe, asymmetric pile-head defect, asymmetric reduction of cross-section in the middle of the pile length, asymmetric reduction of cross-section in two locations along the pile length, significantly degraded pile along its full length, different elastic modulus in the pile-toe zone and different elastic modulus and asymmetric reduction of the cross-section in two locations along the pile. Shifting in the response velocity on the reflectogram from positive to negative values indicates the locations of discontinuities and defects in the discrete 3D pile model, where there is a clear difference between the reflectograms depending on the position of the measuring locations.

The study defines the typological reflectogram models: without discontinuities and defects, pile-head defect, defect in the middle of the pile length or a reduced modulus of elasticity in the middle of the pile length, pile-base defect or a reduced modulus of elasticity in the pile-base zone, and a reduced modulus of elasticity in the pile-head zone. The identification of cracks in the pile is the next step in studying numerical simulations of the PIT.

### ACKNOWLEDGEMENT

The research described in this paper was financially supported by the Ministry of Education and Sciences Republic of Serbia within the Project TR 36043. This support is gratefully acknowledged.

## REFERENCES

[1] Štrukelj, A., Pšunder, M., Vrecl-Kojc, H., Trauner, L. (2009). Prediction of the pile behaviour under dynamic loading using embedded strain sensor technology. Acta Geotechnica Slovenica 6, 65-77.

[2] Trauner, L. (2012). The current state and trends in geotechnics. The 2nd International Scientific Meeting GTZ 2012, Tuzla, Bosnia and Herzegovina, 41-59.

[3] Ding, X., Liu, H., Liu, J., Chen, Y. (2011). Wave propagation in a pipe pile for low-strain integrity testing. Journal for Engineering Mechanics 137, 9, 598-609.

[4] Niederleithinger, E. (2006). Numerical simulation of non-destructive foundation pile tests. The 9th European Conference on NDT, Berlin, Germany.

[5] Niederleithinger, E. (2008). Numerical simulation of low strain dynamic pile test. The 8th International Conference on the Application of Stress Wave Theory to Piles, Lisbon, Portugal, 315-320.

[6] Zhang, C., Yang, S., Zhang, J., Xiao, N. (2010). The numerical simulation for the low strain dynamic integrity testing and its application in quality diagnosis of foundation pile. Journal of Xiamen University (Natural Science), Xiamen, China.

[7] Warrington, D., Wynn, R. (2000). Comparison of numerical methods to closed form solution for wave equation analysis of piling, The 13th Annual Meeting of the Tennessee Section of the American Society of Civil Engineers, Smyrna, USA.

[8] Holeyman, A. (1992). Technology of pile dynamic testing, in: F. Barends (ed.), Application of Stress-Wave Theory to Piles, Balkema, 195-215.

[9] Ambrosini, D., Ezeberry, J. (2005). Long piles integrity trough impact echo technique. Mechanica Computational, Buenos Aires, Argentina, 651-669.

[10] Middendorp, P. (2005). Method statement sonic integrity testing (pile integrity testing). Profound.

[11] Thilakasiri, H. (2006). Interpretation of pile integrity test (PIT) results. Annual Transactions of IESL, 78-84.

[12] Likins, G., Rausche, F. (2000). Recent advances and proper use of PDI low strain pile integrity testing, in: Niyama and Beim (eds.), Application of Stress-Wave Theory to Piles, Balkema, 211-218.

[13] Rorabugh, C. (2011). Notes on digital signal processing - practical recipes for design. Analysis and Implementation, Prentice Hall, New York, USA.

[14] Liao, S., Roesset, J. (1997). Dynamic response of intact piles to impulse loads. International Journal for Numerical and Analytical Methods in Geomechanics 21,4, 255-275.

[15] Hilber, H., Hughes, T., Taylor, R. (1977). Improved numerical dissipation for time integration algorithms in structural dynamics. Earthquake Engineering and Structural Dynamics 5, 3, 283-292.
[16] Kim, D., Kim, H., Kim, W. (2002). Parametric study on the impact-echo method using mock-up shafts. NDT&E International 35, 8, 595-608.
[17] SAP 2000, (2010). Integrated Software for Structural Analysis and Design, CSI Berkeley, USA.

# DOLOČITEV TEKSTURNIH SPREMEMB V MORSKI GLINI

SUCHIT D. GUMASTE, KANNAN R. IYER, SUSMITA SHARMA in D.N. SINGH

## o avtorjih

Suchit D. Gumaste
Indian Institute of Technology Bombay,
Department of Civil Engineering
Powai, Mumbai-400076, Indija
E-pošta: suchit.gumaste@gmail.com

Kannan R. Iyer
Indian Institute of Technology Bombay,
Department of Civil Engineering
Powai, Mumbai-400076, Indija
E-pošta: kannankr20@gmail.com

Susmita Sharma
Indian Institute of Technology Bombay,
Department of Civil Engineering
Powai, Mumbai-400076, Indija
E-pošta: susmita.sharma4@gmail.com

**vodilni avtor**
Devendra Narain Singh
Indian Institute of Technology Bombay,
Department of Civil Engineering
Powai, Mumbai-400076, Indija
E-pošta: dns@civil.iitb.ac.in

## izvleček

*V članku so opisane preiskave, izvedene za določitev teksture (t.j. razporejenosti zrn zemljine in por) intaktnih vzorcev morske gline, pridobljene z globin od 5 m do 65 m pod morskim dnom. Za določanje električne prevodnosti vzorcev morske gline v vzdolžnih in prečnih smereh sedimentacije je bila uporabljena impedančna spektroskopija, ki je neškodljiva in neinvazivna tehnika. Stopnje anizotropije v teksturi zemljin so izražene z anizotropnim koeficientom* $A_e$ *kot funkcije globine. Za preučevanje teksture oziroma porazdelitve velikosti por teh vzorcev sta bila uporabljena vrstični elektronski mikroskop in živosrebrna porozimetrija. Rezultati raziskav so pokazali, da se* $A_e$ *z globino poveča zaradi spremenjene razporejenosti zrn. V manjših globinah so zrna kosmičena in naključno orientirana, v večjih globinah pa razpršena in paralelno usmerjena. Študija poudarja pomembnost in uporabnost anizotropnega koeficienta* $A_e$ *za določanje sprememb v teksturi morske gline zaradi zgostitve pod lastno težo.*

## ključne besede

morska glina, anizotropija, laboratorijski testi

# DETERMINATION OF THE FABRIC ALTERATION OF MARINE CLAYS

SUCHIT D. GUMASTE, KANNAN R. IYER, SUSMITA SHARMA and D.N. SINGH

## about the authors

Suchit D. Gumaste
Indian Institute of Technology Bombay,
Department of Civil Engineering
Powai, Mumbai-400076, India
E-mail: suchit.gumaste@gmail.com

Kannan R. Iyer
Indian Institute of Technology Bombay,
Department of Civil Engineering
Powai, Mumbai-400076, India
E-mail: kannankr20@gmail.com

Susmita Sharma
Indian Institute of Technology Bombay,
Department of Civil Engineering
Powai, Mumbai-400076, India
E-mail: susmita.sharma4@gmail.com

**corresponding author**
Devendra Narain Singh
Indian Institute of Technology Bombay,
Department of Civil Engineering
Powai, Mumbai-400076, India
E-mail: dns@civil.iitb.ac.in

## Abstract

*This paper presents details of investigations that were conducted to determine the fabric (i.e., the arrangement of soil grains and pores) of undisturbed marine clay samples that were retrieved from 5 m to 65 m below the seabed. Impedance Spectroscopy (IS), which is a non-destructive and non-invasive technique, was employed to determine the electrical conductivities of the marine clay samples in their longitudinal and transverse planes of sedimentation. These results were employed to define the extent of the fabric anisotropy in terms of an anisotropy coefficient,* $A_e$*, as a function of depth. In addition, Scanning Electron Microscopy (SEM) and Mercury Intrusion Porosimetry (MIP) were employed to study the fabric and pore-size distribution of these samples, respectively. Based on these investigations it has been observed that* $A_e$ *increases with sampling depth, which is indicative of the alteration from flocculated fabric, at shallower depths, to the dispersed fabric, at deeper depths. The study highlights the importance and usefulness of the anisotropy coefficient,* $A_e$*, for determining the alteration in the fabric of marine clays, due to self-weight consolidation.*

## Keywords

marine clays, anisotropy, laboratory tests

## NOTATIONS

| | |
|---|---|
| $\sigma_{dc}$ | DC conductivity of the sample |
| $\eta$ | porosity of the sample |
| $G$ | specific gravity |
| $e$ | voids ratio |
| $\gamma_d$,$\gamma_t$ | dry and total unit weight of the sample, respectively |
| $w$ | gravimetric water content |
| $\omega$ | frequency of the AC |
| $\sigma_{dct}$, $\sigma_{dcl}$ | DC conductivity in the transverse and longitudinal directions, respectively |
| $\sigma_{AC}$ | AC conductivity |
| $A$ | area of the electrodes |
| $A_e$ | anisotropy coefficient |
| $d_s$ | sampling depth |
| $d$ | pore diameter |
| $d_m$ | mean pore diameter |
| $d_d$ | dominant pore diameter |
| IS | impedance spectroscopy |
| $l$ | distance between the electrodes |
| L/S | liquid to solid |
| MIP | mercury intrusion porosimetry |
| $P$ | pressure |
| SEM | scanning electron microscopy |
| $V_{Hg}$ | cumulative volume of mercury intruded in the sample |
| $V_{HgI}$ | incremental volume of mercury intruded in the sample |
| $Z'$ | real part of the impedance |

# 1 INTRODUCTION

Marine clays are formed through a process of the sedimentation of suspended particles in seawater. During this process, clay and silt particles flocculate and settle as flocs on the seabed due to the cations present in the seawater [1]. When more and more flocs accumulate at the top, the bottom layers consolidate due to the weight of the sediments lying above. This process, called self-weight consolidation, was previously studied by other researchers [2-6]. Marine clays are soft in consistency and hence exhibit a poor shear strength and a high compressibility [7], and hence due to such adverse engineering behaviour, these soils pose great challenges to the civil-engineering profession [8].

An overview of the studies conducted by previous researchers [9-18] reveals that factors like degree of consolidation, extent of agglomeration, swelling and shrinkage characteristics of sediments, and the chemical constituents of seawater, are responsible for the post-sedimentation fabric (i.e., the spatial arrangement of the particles and the pores) of marine clays. Therefore, a close interrelation between the fabric, and the origin and degree of consolidation of marine clays is expected. Also, as soil fabric is one of the major factors influencing the strength and deformation characteristics of clays [17, 19-34], investigations into the fabric of marine clays that have undergone varying degrees of self-weight consolidation need to be conducted.

In this context, efforts made by some of the previous researchers are worth mentioning. The fabric of marine clays, corresponding to the same depths below the seabed, from the eastern and western coastal cities of India, has been studied with the help of Scanning Electron Microscopy (SEM) [17], and it has been reported that these soils exhibit a mainly flocculated or dispersed fabric, depending upon the characteristics of the depositional environment (e.g., the chemical constituents of seawater). Incidentally, researchers [35] have proposed various models to explain the flocculated, random and dispersed fabric. Efforts have also been made by researchers [36, 37] to study the interrelation between the microstructure of clays and their physical properties using the XRD and SEM techniques. In this context, the mineralogical and micro-fabric analyses of marine clays from Hong Kong are worth mentioning [38, 39].

However, not many efforts have been made to establish a correlation between the fabric of the marine clays with the conditions prevailing during their formation and the degree of compactness, in a quantitative manner. It is believed that such relations would be helpful in understanding the overall effect of the process of self-weight consolidation on the fabric changes in these clays. It should be noted that changes in the fabric also influence the degree of anisotropy of the permeability, shear strength, and other physical properties, as reported by previous researchers [40], and hence quantification of the fabric changes in terms of the fabric anisotropy becomes essential.

Keeping in view the above-mentioned aspects, investigations were carried out on undisturbed marine clays, retrieved from different depths below the seabed. The main objective of these investigations is to quantify the change in the fabric anisotropy with respect to the sampling depth and thereby to elaborate how the fabric of marine clays alters when they are subjected to self-weight consolidation. Details of the investigations performed to achieve this objective are presented in the following.

# 2 LABORATORY INVESTIGATIONS

## 2.1 DETAILS OF THE SAMPLES

Undisturbed marine clay samples (Table 1), collected from the south-eastern coast of India, were used in this study. These samples were retrieved from the same borehole with the help of Shelby tubes of internal diameter 76mm, pushed from the seabed and then transferred to PVC tubes (200 mm long, 90 mm internal diameter and 2 mm wall thickness). Due care was taken to prevent the migration of moisture from the sample, and any physical damage occurring to it, during its transportation from the site to the laboratory, by wrapping it with a cellophane membrane and a bubbled polythene sheet. Both sides of these tubes were covered with PVC caps and sealed with wax. The depth of these samples ranged from 5 to 65 m below the seabed. The specific gravity $G$ of these samples was determined with the help of a helium gas pycnometer (Quantachrome, USA) [41,42]. The total unit weight $\gamma_t$, water content $w$, dry density $\gamma_d$, voids ratio $e$, and porosity $\eta$, of these samples were also determined (Table 1).

## 2.2 PHYSICAL CHARACTERIZATION

A certain portion of each sample was oven dried at 105±5 °C, pulverized, and used for establishing the particle size distribution characteristics [43] and the consistency limits [44]. The results obtained from this exercise are presented in Table 2. Based on the Unified Soil Classification System (USCS) [45] classification, as

**Table 1**. Physical properties of the samples.

| Sample designation | Depth (m) | water content, w (%) | Total unit weight, $\gamma_t$ (kN/m$^3$) | Dry unit weight, $\gamma_d$ (kN/m$^3$) | Specific gravity, *G* | void ratio, *e* | Porosity, $\eta$ (%) |
|---|---|---|---|---|---|---|---|
| S1 | 5.50 | 50.6 | 16.8 | 11.2 | 2.56 | 1.29 | 56 |
| S2 | 8.45 | 35.7 | 17.9 | 13.2 | 2.73 | 1.07 | 52 |
| S3 | 9.45 | 38.2 | 20.5 | 14.8 | 2.91 | 0.96 | 49 |
| S4 | 12.50 | 56.0 | 18.9 | 12.1 | 2.51 | 1.07 | 52 |
| S5 | 15.10 | 27.6 | 19.0 | 14.9 | 2.64 | 0.77 | 44 |
| S6 | 18.55 | 35.3 | 19.9 | 14.7 | 2.68 | 0.82 | 45 |
| S7 | 21.50 | 47.6 | 19.8 | 13.4 | 2.48 | 0.85 | 46 |
| S8 | 27.15 | 32.2 | 19.7 | 14.9 | 2.77 | 0.86 | 46 |
| S9 | 33.50 | 36.7 | 19.1 | 14.0 | 2.53 | 0.81 | 45 |
| S10 | 36.45 | 36.9 | 22.6 | 16.5 | 2.73 | 0.65 | 40 |
| S11 | 38.55 | 28.3 | 20.6 | 16.1 | 2.67 | 0.66 | 40 |
| S12 | 40.55 | 25.8 | 21.2 | 16.9 | 2.82 | 0.67 | 40 |
| S13 | 47.50 | 29.4 | 20.9 | 16.2 | 2.49 | 0.54 | 35 |
| S14 | 50.60 | 56.0 | 25.5 | 16.3 | 2.57 | 0.57 | 36 |
| S15 | 64.40 | 17.6 | 21.5 | 18.3 | 2.68 | 0.47 | 32 |

**Table 2**. Physical properties of the samples: Particle size distribution characteristics and classification of the samples.

| Sample designation | % | | | Liquid limit (%) | Plastic limit (%) | Plasticity Index (%) | USCS* |
|---|---|---|---|---|---|---|---|
| | Clay fraction | Silt fraction | Sand fraction | | | | |
| S1 | 60 | 39 | 1 | 65 | 27 | 38 | MH |
| S2 | 53 | 43 | 4 | 71 | 29 | 42 | CH |
| S3 | 66 | 30 | 4 | 72 | 36 | 36 | MH |
| S4 | 54 | 44 | 1 | 73 | 32 | 41 | CH |
| S5 | 57 | 40 | 3 | 78 | 40 | 38 | MH |
| S6 | 60 | 39 | 1 | 77 | 39 | 38 | MH |
| S7 | 59 | 40 | 1 | 78 | 31 | 47 | CH |
| S8 | 64 | 30 | 6 | 80 | 34 | 46 | CH |
| S9 | 65 | 34 | 1 | 78 | 33 | 45 | CH |
| S10 | 63 | 37 | 0 | 72 | 31 | 41 | CH |
| S11 | 60 | 38 | 2 | 78 | 39 | 39 | MH |
| S12 | 59 | 40 | 1 | 76 | 33 | 43 | CH |
| S13 | 78 | 20 | 2 | 82 | 34 | 48 | CH |
| S14 | 73 | 27 | 0 | 97 | 37 | 60 | CH |
| S15 | 62 | 34 | 4 | 78 | 31 | 47 | CH |

* Unified soil classification system (as per ASTM D 2487-06e1)

depicted in Fig. 1, it can be inferred that these samples belong to the MH and CH groups. This indicates that the marine sediments are relatively uniform up to the depth of interest.

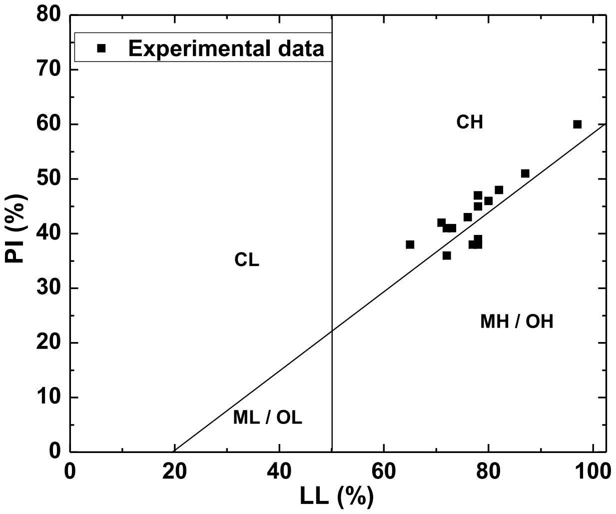

**Figure 1**. Location of different samples on the USCS plasticity chart.

## 2.3 CHEMICAL CHARACTERIZATION

The range of chemical composition (by % weight) of the sample, in the form of major oxides, was determined by using an X-ray Fluorescence setup (Phillips 1410, Netherlands). It was observed that these samples contain $SiO_2$ as a major oxide (58 to 66 %) along with 14 to 17 % of $Al_2O_3$ and 2 to 13 % of $Fe_2O_3$.

The chloride and sulphate contents of the sample were determined on an extract of 2:1 water-to-soil ratio (designated as L/S, by weight), with the help of an Indion Easy test kit (supplied by Ion Exchange India Ltd., Mumbai, India). It was observed that these samples have a sulphate content varying between 5 to 30 ppm for an L/S equal to 10 and 20. However, the chloride content of these soils was found to vary from 700 to 1000 ppm and 300 to 550 ppm, for an L/S equal to 10 and 20, respectively. A water-quality analyser (Model PE 136, Elico Ltd., India), fitted with a glass calomel electrode, was employed for measuring the pH of the soil solution with different liquid-to-solid ratios (L/S=10 and 20). The pH values of these soil solutions fall in the range 8.1 to 8.9.

## 2.4 INVESTIGATIONS ON THE FABRIC ANISOTROPY

In order to establish the variation of the fabric with the depth of the sampling of the specimen, the anisotropy coefficient, $A_e$, which is defined by Eq. 1 [46-48], was employed:

$$A_e = \sqrt{\frac{\sigma_{dct}}{\sigma_{dcl}}} \qquad (1)$$

where $\sigma_{dct}$ and $\sigma_{dcl}$ are the DC conductivities in the horizontal (i.e., transverse to the plane of sedimentation) and vertical (i.e., longitudinal to the plane of sedimentation) directions, respectively.

The methodology based on Impedance Spectroscopy (IS) [49-51], developed by previous researchers [48], was employed to measure $\sigma_{dct}$ and $\sigma_{dcl}$ and hence to compute $A_e$. In addition, Scanning Electron Microscopy (SEM) and Mercury Intrusion Porosimetry (MIP) were also conducted on the specimens of the samples in order to observe the particle-to-particle interaction and the pore size distribution, respectively, as discussed in the following.

## 2.5 ELECTRICAL CONDUCTIVITY MEASUREMENTS

With the help of a stainless-steel sample extruder (exhibiting an area ratio of less than 10%) and a piston attached to it, samples (38 mm diameter and 30 mm long) were retrieved from the PVC tubes. To avoid any distortion during the sample collection and extraction, the extruder was lubricated with silicon grease. The DC conductivities, $\sigma_{dc}$, of these samples were determined for the longitudinal direction and the transverse direction by employing an LCR (Inductance, Capacitance and Resistance) meter (Agilent 4284A). The methodology for sample preparation, the detailed information regarding the test setup, the method of calibration and the procedure adopted for determining $\sigma_{dc}$, reported by previous researchers [48, 52], are discussed in the following.

The test setup, depicted in Fig. 2, was employed for measuring the electrical conductivity, $\sigma_{dc}$, of the sample. This setup consists of two acrylic plates (100 mm × 100 mm × 10 mm) and at the centre of each of these plates a stainless-steel electrode (50 mm × 50 mm × 2 mm) is fitted. These electrodes are mirror finished, passivated and are connected to brass bolts, across which an electrical potential can be applied. The sample can be fitted between these plates by adjusting their distance with the help of a steel rod and screws arrangement, as depicted in Fig. 2(d). The calibration of the test setup was made by applying open- and short-circuit corrections, which help in eliminating the unwanted impedance generated due to connecting the cables of the LCR meter and the stray capacitance [48, 52]. After the calibration of the test setup, the $\sigma_{dc}$ of the sample (38 mm in diameter and 30 mm in height) was determined, as explained in the

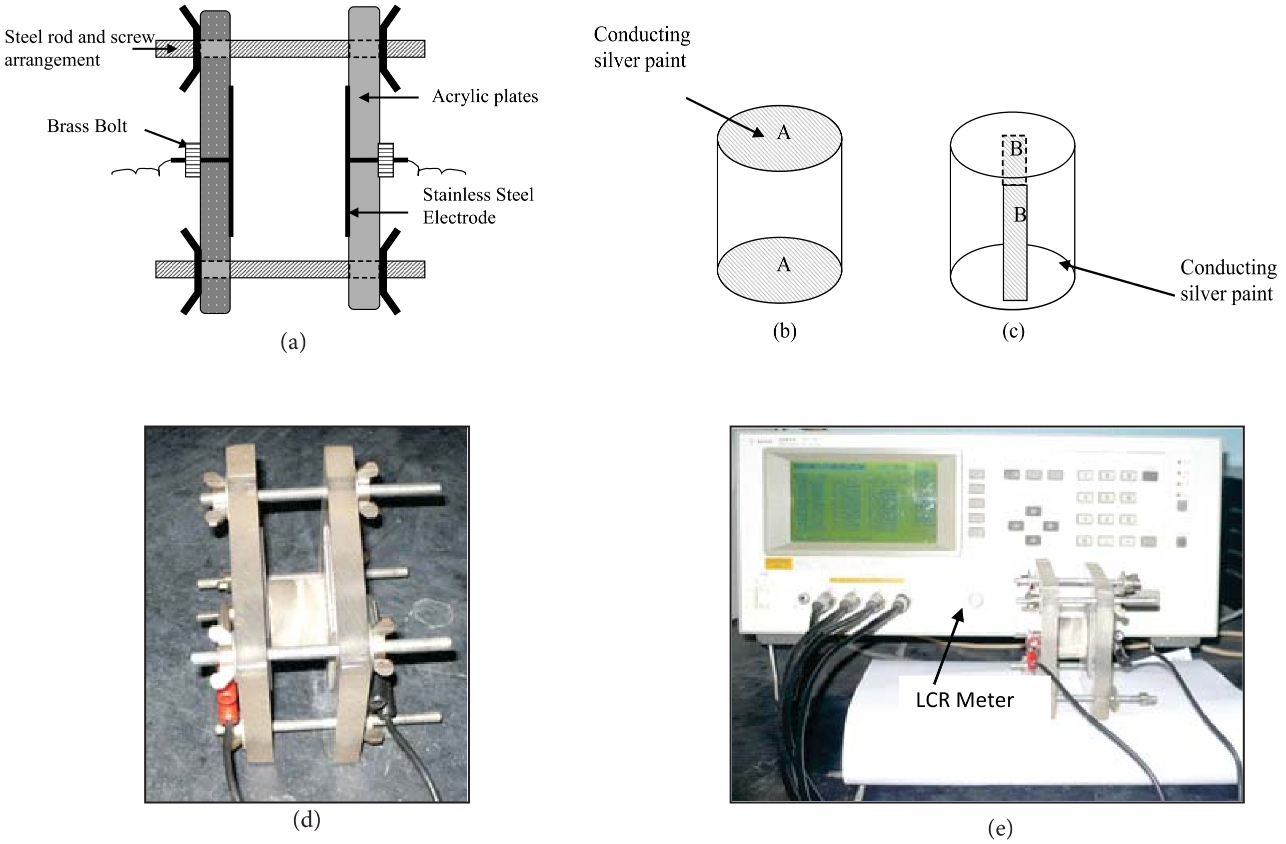

(a) (b) (c)

(d) (e)

**Figure 2**. (a) Schematic of the sample holder, (b) Longitudinal (A-A) view of the sample, (c) transverse (B-B) view of the sample, the photographs of (d) the sample holder and (e) the test setup.

following. As depicted in Fig. 2(b and c), the top and bottom surfaces, and the about 10-mm-thick curved surface on the opposite sides of the sample, were painted with a conducting silver paint. Next, the AC conductivity, $\sigma_{AC}$, of the sample was determined by employing a LCR meter, which works in the frequency range 20 Hz to 1 MHz and by applying an electric field of 1 V. As reported by previous researchers [52], the real part of the impedance, $Z'$, which gets displayed on the LCR meter corresponding to a different frequency of AC (designated as $\omega$), was recorded and by employing Eq. 2 the $\sigma_{AC}$ was computed.

$$\sigma_{AC} = \frac{\boldsymbol{l}}{Z' \cdot \boldsymbol{A}} \qquad (2)$$

where ***l*** and ***A*** are the distance between the electrode plates and area of the electrodes, respectively.

Subsequently, $\sigma_{AC}$ was plotted with respect to $\omega$ (on x-axis) and the intersection of the linear portion of the plot on the $\sigma_{AC}$ axis ($\omega$=0) was determined, which yields the $\sigma_{dc}$ of the sample [52].

## 2.6 DETERMINATION OF SOIL FABRIC

The fabric of the sample was determined using SEM and MIP. To achieve this, approximately 5-mm-sized cubic specimens were extruded from the middle one-third portion of the samples, after the electrical conductivity was recorded. The pore-fluid present in the specimen was removed by employing an air-drying technique [48]. As the soil specimens are non-conducting in nature, there will be a charge accumulation on their surface, which results in blurring and poor quality of the images during the SEM studies. In order to minimize this, the specimens were placed on a sample holder, with a conducting carbon base, and were coated with an about 15-nm-thick gold-palladium (a conducting material) layer by employing a coating device (JCF 1600, JEOL). The SEM images (corresponding to 500× to 8000× magnification and depicting the view perpendicular to the plane of deposition) of the specimen were obtained by employing Quanta 200 ESEM instrument. Although the ESEM allows different modes (i.e., the high-vacuum mode and the ESEM mode) for image capturing, which also facilitates an analysis of wet specimens, the high-vacuum mode, which necessitates the use of air-dry specimens, was employed in the present study to obtain a better resolution of the images. At lower magnifications, general fabric features were studied, while at higher magnifications the particle assemblage, the type of the contacts and the pore space morphology were inspected.

The pore-size distribution characteristics of the specimen were obtained with the help of a MIP (Quantachrome, USA). The MIP works on the principle that the applied pressure required for the intruding mercury (a non-wetting liquid) into the pores is inversely proportional to their size [53]. The test is performed by increasing the pressure, $P$ (up to 225 MPa, which corresponds to the pore diameter, 0.0064 μm), on the mercury filling the cell containing the sample. The pore-size obtained from the measured pressure, by assuming a contact angle and a surface tension of the mercury as 140° and 0.480 N/m, respectively [54], when plotted against the cumulative volume of the mercury intruded into the sample, $V_{Hg}$, facilitates a determination of the pore-size distribution characteristics of different specimens (see Fig. 9).

## 3 RESULTS AND DISCUSSION

The magnitude of $\sigma_{dc}$ for the soil samples measured in two directions, designated as $\sigma_{dct}$ and $\sigma_{dcl}$, is presented in Table 3. It is clear from the data presented in the table that $\sigma_{dct}$ is higher than $\sigma_{dcl}$ for all the samples. This indicates that the electrical conductivity measurements are dependent on the direction along which they are measured and this directional dependency (i.e., electrical anisotropy) can be quantified by employing Eq. 1. Although $\sigma_{dc}$ depends strongly upon the voids ratio, particle arrangement and the pore-fluid conductivity, $A_e$ would be a function of the anisotropy of the particle arrangement or the fabric anisotropy [48, 55]. With

**Table 3**. DC Conductivities and anisotropy coefficient of different samples.

| Sample designation | Depth (m) | $\sigma_{dcl}$ (S/m) | $\sigma_{dct}$ (S/m) | $A_e$ |
|---|---|---|---|---|
| S1 | 5.50 | 2.14 | 5.53 | 1.61 |
| S2 | 8.45 | 2.84 | 8.65 | 1.75 |
| S3 | 9.45 | 2.86 | 9.06 | 1.78 |
| S4 | 12.50 | 2.52 | 6.92 | 1.66 |
| S5 | 15.10 | 3.10 | 9.40 | 1.74 |
| S6 | 18.55 | 2.79 | 9.14 | 1.81 |
| S7 | 21.50 | 1.95 | 6.53 | 1.82 |
| S8 | 27.15 | 2.34 | 9.13 | 1.97 |
| S9 | 33.50 | 1.53 | 4.96 | 1.79 |
| S10 | 36.45 | 1.58 | 6.15 | 1.97 |
| S11 | 38.55 | 2.29 | 10.10 | 2.10 |
| S12 | 40.55 | 2.12 | 9.61 | 2.13 |
| S13 | 47.50 | 0.81 | 3.68 | 2.14 |
| S14 | 50.60 | 2.45 | 11.86 | 2.20 |
| S15 | 64.40 | 0.26 | 1.36 | 2.27 |

$\sigma_{dct}$ = DC conductivity in the transverse direction;
$\sigma_{dcl}$ = DC conductivity in the longitudinal direction;
$A_e$ = anisotropy coefficient

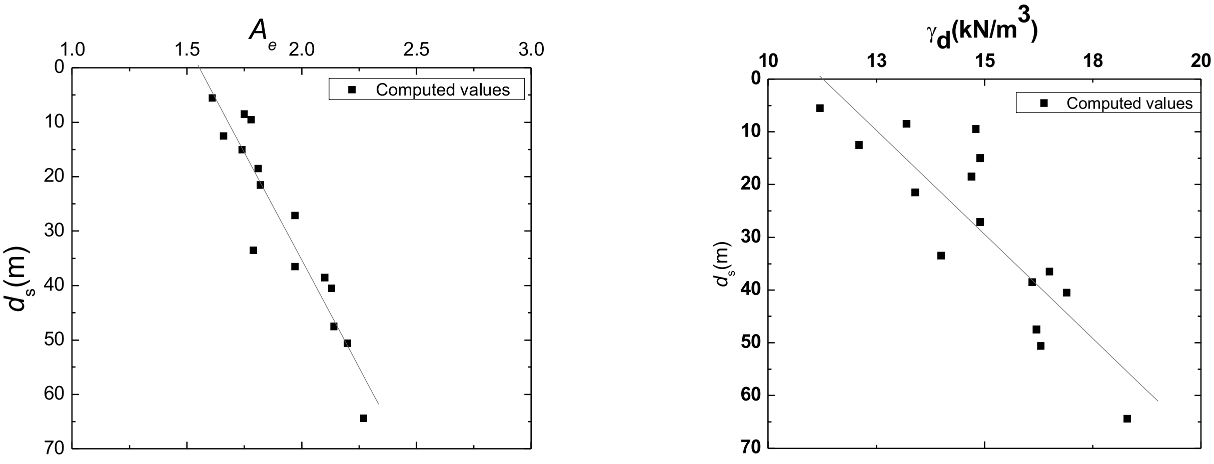

(a)

(b)

**Figure 3**. Variation of (a) $A_e$ and (b) $\gamma_d$ with the depth of different samples.

this in view, $A_e$ for different samples was computed (see Table 3) and its variation with respect to the sampling depth, $d_s$, is depicted in Fig. 3(a). Also, the variation of $\gamma_d$, with respect to $d_s$ is depicted in Fig. 3(b).

It is clear from the trends depicted in Fig. 3 that with an increase in $d_s$, $A_e$ and $\gamma_d$ increase linearly. These trends can be attributed to the variation in the spatial arrangement of the soil particles and the pores, along the depth of the sediment deposition. This can be confirmed from Table 4, where the macro pores reduce nearly linearly with depth (i.e., from 42.04 % for S1, at 5.5 m depth, to 6.61% for S15, at 64.4 m depth).

**Table 4**. Summary of the MIP results for different samples.

| Sample Designation | Macro-pores (%) | Meso-pores (%) | Micro-pores (%) | $^*d_d$ (μm) | $^*d_m$ (μm) |
|---|---|---|---|---|---|
| S1 | 42.04 | 52.59 | 5.37 | 0.04-0.3 | 0.043 |
| S4 | 30.22 | 65.00 | 4.78 | 0.03-0.1 | 0.036 |
| S7 | 23.43 | 68.84 | 7.73 | 0.02-0.06 | 0.029 |
| S11 | 12.80 | 84.13 | 3.07 | 0.02-0.06 | 0.026 |
| S14 | 9.55 | 84.73 | 5.72 | 0.008-0.02 | 0.023 |
| S15 | 6.61 | 78.77 | 14.62 | 0.007-0.03 | 0.018 |

$^*d_d$ = Dominant pore diameter;
$^*d_m$ = Mean pore diameter

Furthermore, up to 15 m depth, comparatively smaller values of $A_e$ (≈1.7) are observed. In this context, researchers [48] have reported that $A_e$ for undisturbed samples is higher than that of the remoulded samples and undisturbed soil samples, with dispersed fabric structure, exhibit $A_e$≈2.0. It has also been stated by these researchers that the transition from the flocculated to the dispersed structure, for the remoulded samples, occurs at $A_e$≈1.6. Hence, $A_e$≈1.7 reflects a random arrangement, or a small degree of preferred orientation of the particles, in the natural soil deposits. This type of particle arrangement, referred to as a 'Flocculated' fabric, would normally be associated with comparatively younger sediments in the seabed. In this fabric, particles get attracted to one another in a very loose, haphazard manner, resulting in higher values of the voids ratio, *e*. However, a further decrease in *e*, with a corresponding increase in $d_s$, clearly indicates that sediments develop denser fabrics. This phenomenon can also be attributed to a subsequent increase in the overburden pressure, which the initial fabric would not be able to sustain as a result of the continuous accumulation of sediments. In other words, self-weight consolidation [2-6] would cause the rearrangement, or reorientation, of the particles in the preferred direction, progressively, which is reflected in an increase in $A_e$ [≥2.0 for $d_s$>35 m, see Fig. 3(a)]. As such, higher values of $A_e$ clearly indicate an increasing degree of preferred orientation of the particles in the horizontal plane. In other words, the fabric appears to be more anisotropic with the increase in depth, which is a typical characteristic of the dispersed fabric. Hence, it can be stated that with an increase in the depth of marine clays, the initially developed flocculated fabric is changed to a dispersed fabric and this alteration could be captured, quantitatively, in terms of $A_e$, relatively easily and quickly. In order to verify this hypothesis the results obtained from MIP and SEM were further analysed, as discussed in the following.

Samples S1, S4, S7, S11, S14 and S15 were analysed by employing the SEM and MIP techniques. Based on the data presented in Table 1, the samples used in the present study can be considered to represent sediments ranging from shallow depths (up to 35 m) to greater depths (>35 m). The SEM images of the specimens of these samples are depicted in Figures 4 to 8.

For instance, the SEM images of specimen S1 (taken in the horizontal plane of the sample, as depicted in Figure 4), which is a younger sediment than its counterparts, reveal that the fabric exhibits mainly 'edge-to-edge' and/or 'edge-to-face' contacts between the clay particles that are randomly orientated [23]. From the figure it can also be observed that it is a typical case of a honeycomb fabric [56] or a cellularity, by which sediments have been deposited in the form of continuous chains, as depicted in Fig. 4(a). This phenomenon can be attributed to the electrolyte-rich conditions of the marine environment, which is mainly due to the presence of a high chloride content. And due to this, the sediments are deposited in the form of flocs or agglomeration, and hence as a result a highly porous fabric is observed. Incidentally, Fig. 4(b) does not exhibit any sign of stratification (parallel orientation of clay platelets). Thus, it is a typical fabric of the marine clay that has been subjected to a negligible overburden pressure, due to the shallow depth of the deposition. On the other hand, for specimen S4 the SEM images are depicted in Figure 5. These micrographs reveal the presence of a typical matrix fabric [56], wherein larger gaps between the silt particles are found to be occupied by agglomerated clay platelets. From the results presented in Table 2, a comparatively higher percentage of silt fraction can be confirmed for sample S4. Such a type of fabric is relatively common among poorly and moderately consolidated marine clays (i.e., those deposited in an estuary), with a dry density not higher than 16.5 kN/m$^3$ [57].

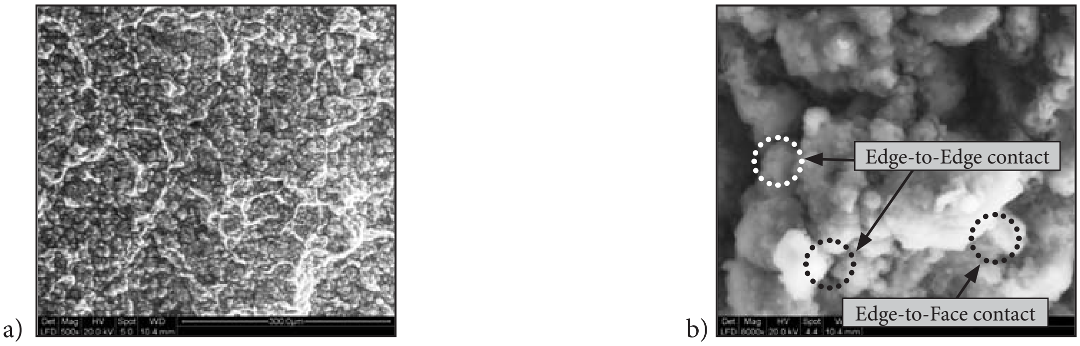

**Figure 4**. SEM images of S1 along horizontal (transverse) plane.

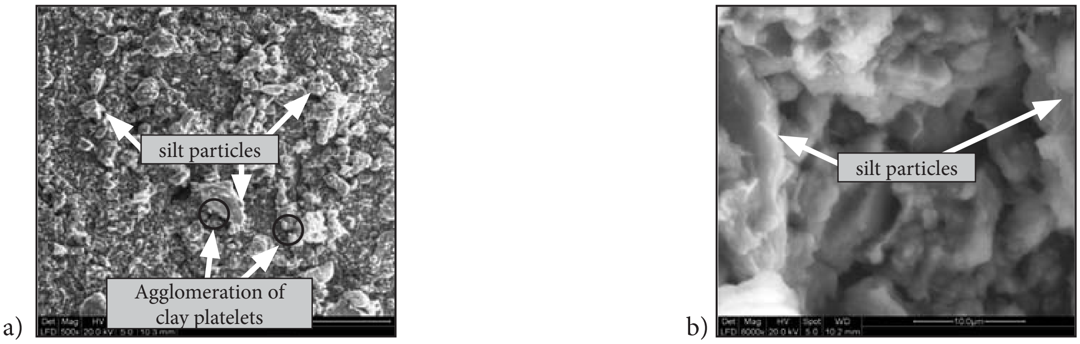

**Figure 5**. SEM images of S4 along horizontal (transverse) plane.

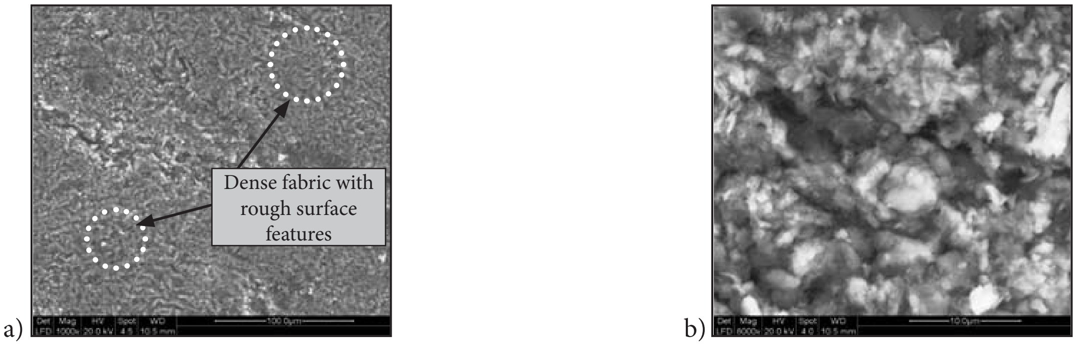

**Figure 6**. SEM images of S11 along horizontal (transverse) plane.

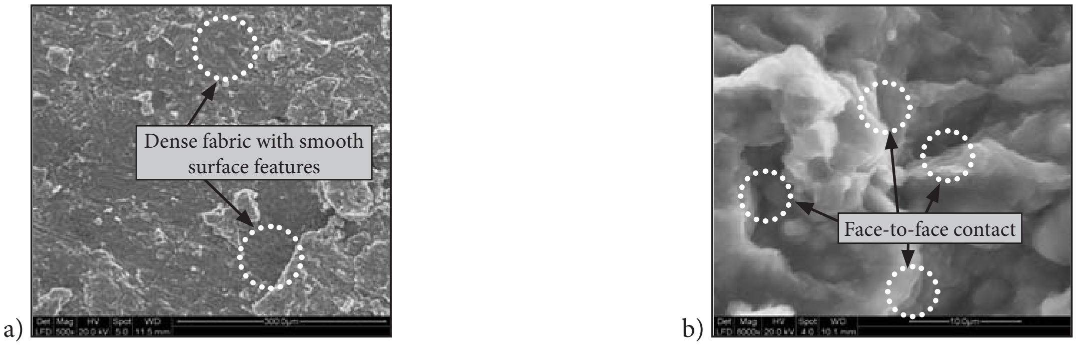

**Figure 7**. SEM images of S14 along horizontal (transverse) plane.

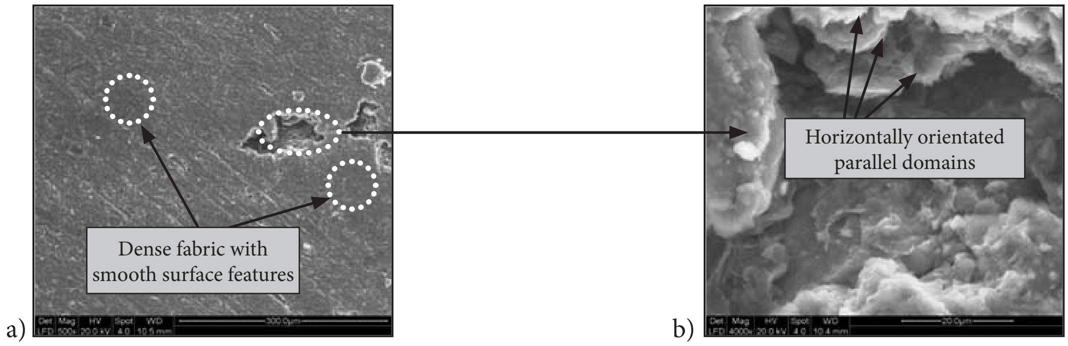

**Figure 8**. SEM images of S15 along horizontal (transverse) plane.

However, with a further increase in depth, the fabric acquires a dense structure with a specific orientation (face-to-face orientation) of particles with rough or smooth surface features and the presence of small pores), as depicted in Figures 6, 7 and 8, for the specimens S11, S14 and S15, respectively. This again can be attributed to the self-weight consolidation at deeper depths. Hence, the distinctive orientation of the clay platelets is observed to be in the transverse plane that is perpendicular to the direction of self-weight consolidation and which ultimately results in a 'face-to-face' contact between them [23]. These platelets increasingly become oriented parallel to each other, thereby making the fabric highly anisotropic. Thus, it can be concluded that with an increase in the depth, the particles and pores rearrange or reorient themselves into a new fabric that can be referred to as a 'dispersed' fabric.

In order to verify the above-mentioned findings, which are based on SEM, MIP studies were also conducted on the same specimens. The variation of the percentage cumulative volume of mercury intruded in the specimen, $V_{Hg}$, with respect to the pore diameter $d$ was plotted as depicted in Fig. 9, from which the percentages of micro-pores ($d$<0.01μm), meso-pores (0.01μm<$d$<0.05μm) and macro-pores (0.05μm<$d$<10μm) present in the specimen [58] were determined. In addition, for each specimen, $d_m$ which is the mean pore diameter and which corresponds to the pore diameter at which 50% of the pore volume gets intruded in the pore-size range considered [59], was also determined. The dominant pore diameter, $d_d$, which corresponds to the pore diameter at which the maximum incremental volume of mercury is intruded into the specimen (i.e., the maximum numbers of pores in the specimen are of this diameter), was determined as a diameter corresponding to the maximum (peak) incremental volume, $V_{HgI}$, in the plot between $V_{HgI}$ and pore diameter [34]. However, it should be noted that multiple peaks were observed in the plot between

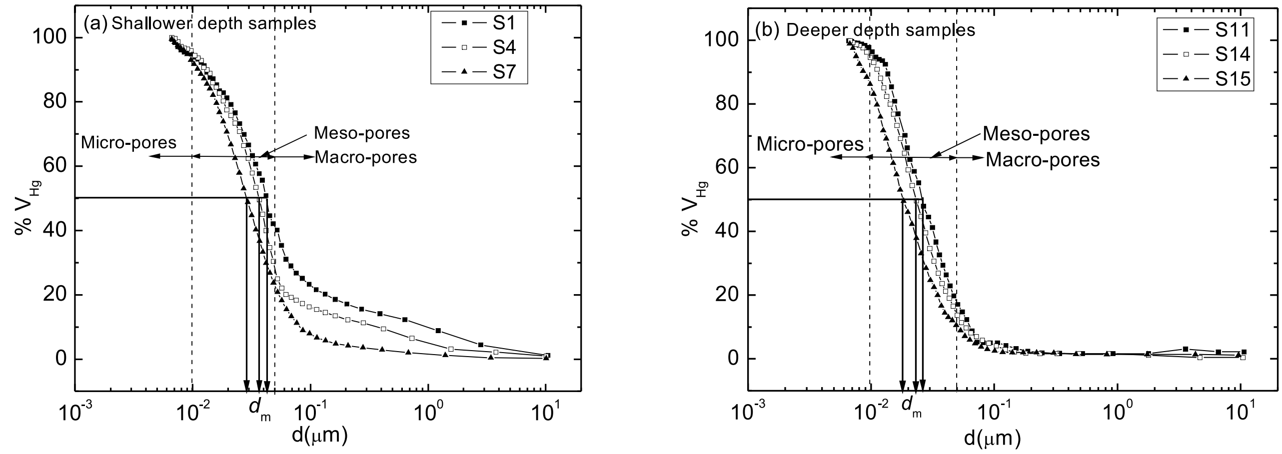

**Figure 9**. Pore size distribution w.r.t. % cumulative intrusion volume of mercury.

the $V_{HgI}$ and pore diameter, and hence the range of the dominant pore sizes can be defined as listed in Table 4. Furthermore, from the table it can be noted that as the depth increases, the percentage of macro-pores, and the value of $d_m$ , decreases. In contrast, an increase in the percentages of meso- and micro-pores can be observed with an increase in the depth. For instance, specimens S1, S4 and S7 at lower depths exhibit a higher volume of macro pores (23.4 to 42 %) and a moderate volume of meso pores (52.6 to 68.6%), which represents a poorly-to-moderately consolidated deposit that exhibits a flocculated fabric structure. In contrast, specimens S11, S14 and S15 at higher depths exhibit a relatively lower volume of macro pores (6.6 to 12.8%) and a higher volume of meso pores (78.7 to 84.7%), representing a dense and highly consolidated deposit that exhibits a dispersed fabric structure. In other words, it can be said that with an increase in depth, the dominance of intra-aggregate pores, $d$<1.5 μm [34] over inter-aggregate pores, $d$≥1.5 μm, increases. This can be attributed to the reorganization and reorientation of clay platelets with an increase in depth (i.e., due to self-weight consolidation), which is responsible for the alteration of the randomly oriented fabric to the dispersed fabric. Hence, it can be inferred that the change in the fabric anisotropy, which in turn depends on alterations in the fabric structure, is related to a change in the size of the pores.

Furthermore, in order to highlight the importance of the study, the results obtained from the IS, SEM and MIP were superimposed in Fig. 10. It is clear from this figure, and Tables 1, 3 and 4, that the specimens S1, S4 and S7 exhibit a value of $A_e$ between 1.61 and 1.82 and $d_m$ values between 0.029 to 0.043 μm. The lower values of $A_e$ and the relatively higher values of $d_m$ indicate a honeycomb-type or matrix-type flocculated structure [60]. The analysis of the SEM images of these specimens (see Figs. 4 and 5), as described earlier, also qualitatively confirms the flocculated structure. In addition, it can be seen that for specimens S11, S14 and S15, $A_e$ lies between 1.97 and 2.27 and the dm values are observed to be between 0.018 to 0.026 μm. Hence, it can be inferred that the higher $A_e$ (≥ 2.0) and lower $d_m$ would be representative of the dispersed structure. These fabric arrangements could be qualitatively observed in their SEM images (see Figs. 6 to 8). Hence, it can be hypothesized that Fig. 10 presents guidelines for determining the fabric (i.e., its type and the corresponding $d_m$) of the marine clays, if their $A_e$ is known. It must be appreciated that a determination of $A_e$ is relatively easy and less time consuming as compared to the SEM and MIP techniques. However, for a generalization of these findings, exhaustive investigations should be conducted on marine clays obtained from different locations and that too in the depth ranges beyond those covered in the present study.

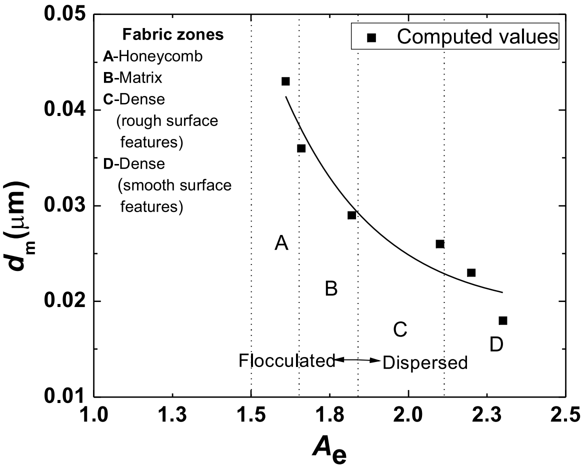

**Figure 10**. Variation in the fabric structure for Marine clay.

Incidentally, it is worth mentioning here that the marine clay samples, which were retrieved from the offshore environment and transported to the laboratory, might have undergone changes from their undisturbed in-situ state due to various factors, such as sampling disturbance, relief of stresses from the sample during and after soil sampling, and smearing effects [61]. Also, the extraction of the sample from deeper locations would cause stress relaxation due to the removal of overburden and confining stresses and might result in a swelling of the samples [62, 63]. Furthermore, the soil below the drilled borehole might be subjected to higher vertical stresses, which might lead to localized compaction and disturbance of the soil layer beneath. Also, the mechanical disturbance caused by driving the sampler causes shear distortion and subsequent compression or remoulding of the soil (i.e., smearing) very close to the inner face of the sampler [63, 64]. These effects of stress relaxation, smearing and local disturbances could be different depending on the sampling depth and the overall characteristics of the soil (i.e., physical, chemical and mineralogical properties). The authors would like to reiterate that though the above mentioned factors might result in changes in the pore and fabric structure of the soils, which is responsible for changes in their anisotropy, the sampling procedure adopted in this study (i.e., the use of a sampler with an area ratio less than 10% for undisturbed soil sampling and careful extrusion of specimens for MIP, IS and SEM studies) ensures that these effects are minimal.

## 4 CONCLUDING REMARKS

In this study efforts were made to investigate the variation of the fabric of marine clays that were obtained from different depths below the seabed, in their undisturbed state. To achieve this, the anisotropy coefficient, $A_e$, was determined with the help of Impedance Spectroscopy and the same was found to vary from 1.5 to 2.25, for samples obtained from depths of 5 m to 65 m. This variation can be attributed to the self-weight consolidation, which alters the fabric of these samples and renders them increasingly anisotropic, with an increase in the depth. This hypothesis was substantiated by observing the scanning electron micrographs of some selected samples from different depths and by determining their pore size distribution characteristics with the help of Mercury Intrusion Porosimetery. It was demonstrated that with an increase in depth, the fabric alters from randomly oriented (or flocculated) to oriented in a preferred direction (or dispersed) and there is a reduction in the mean pore diameter (from 0.05 μm to 0.015 μm). As such, it can be stated that Impedance Spectroscopy is an effective tool to investigate (and quantify) the fabric of marine clays, easily and quickly.

## REFERENCES

[1] Katagiri, M., Imai, G. (1994). A new in-laboratory method to make homogeneous clayey samples and their mechanical properties. Soils Found. 34, 2, 87-93.

[2] Imai, G. (1980). Settling behavior of clay suspension. Soils Found. 20, 2, 61-77.

[3] Been, K., Sills, G.C. (1981). Self-weight consolidation of soft soils: an experimental and theoretical study. Geotechnique 31, No. 4, pp. 519-535.

[4] Lee, K., Sills, G. C. (1981). The consolidation of a soil stratum, including self-weight effects and large strains. Int. J. Numer. Anal. Methods Geomech. 5, 4, 405-428.

[5] Toorman, E.A. (1996). Sedimentation and self-weight consolidation: general unifying theory. Geotechnique 46, 1, 101-113.

[6] Toorman, E.A. (1999). Sedimentation and self-weight consolidation: constitutive equations and numerical modeling. Geotechnique 49, 6, 709-726.

[7] Sridharan, A., Prakash, K. (2003). Self-weight consolidation: compressibility behavior of segregated and homogeneous fine-grained sediments. Marine Georesources and Geotechnology 21, 73-80.

[8] Bjerrum, L. (1973). Geotechnical problems involved in foundation of structures in North sea. Geotechnique 23, 3, 319-358.

[9] Bryant, W. R., Cernock, P., Morelock, J. (1967). Shear strength and consolidation characteristics of marine sediments from the western Gulf of Mexico. In: Richards, A.F. (Ed.), Marine Geotechnique. University of Illinois Press, Urbana, IL, 41-61.

[10] Richards, A.F. (Ed.), (1967). Marine Geotechnique, University of Illinois Press, Urbana, IL., 237.

[11] Gillot, J. E. (1968). Clay in Engineering Geology. Elsevier, London.

[12] Rashid, M.A., Brown, J.D. (1974). Influence of marine organic compounds on the engineering properties of a remoulded sediment. Engg. Geol. 9, 141-154.

[13] Katti, R.K. (1975). Regional soil deposits of India. Proceedings 5th Asian Regional Conf. on SM and FE, Bangalore, India, 11, 1-98.

[14] Penner, E., Burn, K.N. (1978). Review of engineering behavior of marine clays in eastern Canada. Can. Geotech. Journal 15, 2, 269-282.

[15] Egashira, K., Ohtsubo, M. (1982). Smectite in marine quick clays of Japan. Clays Clay Miner. 30, 4, 275-280.

[16] Torrance, J.K. (1975). On the role of chemistry in the development and behaviour of the sensitive marine clays of Canada and Scandinavia. Can. Geotech. Journal 12, 3, 326-335.

[17] Rajasekaran, G., Murali, K., Srinivasaraghavan, R. (1999). Microfabric, chemical and mineralogical study of Indian marine clays. Ocean Engineering, 26, 5, 463-483.

[18] Yanjun, D., Shenglin, L., Shigenori, H. (1999). Swelling-shrinkage properties and soil improvement of compacted expansive soil, Ning-Liang Highway, China. Engg. Geol. 53, 351-358.

[19] Lambe, T.W. (1958). The structure of compacted clay. Journal of the Soil Mechanics and Foundations Division, Proceedings of the American Society of Civil Engineers, Paper 1654 SM2, 1-34.

[20] Lafeber, D. (1962). Aspects, of stress-induced differential movements of fabric elements in mineral soils. Australian Road Research Board 1, 1059-1067.

[21] Ingles, O.G., Lafeber, D. (1966). The influence of volume defects on the strength and strength isotropy of stabilized clays. Engineering Geology 1, 305-310.

[22] Diamond, S. (1970). Pore Size Distribution in Clays. Clays Clay Miner. 18, 7-23.

[23] McConnachie, I. (1974). Fabric changes in consolidated Kaolin. Geotechnique 24, 207-222.

[24] Brewer, R. (1976). Fabric and Mineral Analysis of Soils. Robert E. Krieger Publishing, Huntinton, NY.

[25] Murphy, C.P., Bullock, P., Biswell, K.J. (1977). The measurement and characterization of voids in soil thin sections by image analysis: Part II. Applications. Journal of Soil Science 28, 509-518.

[26] Collins, K. (1983). Scanning electron microscopy of engineering soils. Geoderma 30, 1-4, 243-252.

[27] Delage, P., Lefebvre, G. (1984). Study of the structure of a sensitive Champlain clay and its evolution during consolidation. Can. Geotech, J. 21, 1, 21-35.

[28] Griffiths, F.J., Joshi, R.C. (1989). Change in pore size distribution due to consolidation of clays. Geotechnique 39, 1, 159-167.

[29] Mitchell, J.K. (1993). Fundamentals of Soil Behavior, John Wiley & Sons, New York.

[30] Basma, A. ., Azm, S. A., Malkawi, A.I.H., Mohamed, A.A.B. (1996). Swelling-shrinkage behavior of natural expansive clays. App. Clay Sci. 11, 2-4, 211-227.

[31] Rao, S.M., Revanasiddappa, K. (2005). Role of microfabric in matrix suction of residual soils. Engng. Geol. 80, 1-2, 60-70.

[32] Dolinar, B., Trauner, L. (2007). The impact of structure on the undrained shear strength of cohesive soils, Engng. Geol. 92, 1-2, 88-96.

[33] Wang, Y.H., Xu, D. (2007). Dual Porosity and Secondary Consolidation. J. Geotech. Geoenviron. Engng., ASCE, 133, 7, 793-801.

[34] Souli, H., Fleureau, M., Trabelsi Ayadi, M., Besnard, M. (2008). Physicochemical analysis of permeability changes in the presence of zinc. Geoderma 145, 1-2, 1-7.

[35] Yong, R. N., and Warkentin, B. P. (1966). Introduction to Soil Behaviour. MacMillan, New York.

[36] Ospiv, V.I. (1983). Methods of studying clay microstructure. Geotech. Test. J. ASTM 6, 1, 10-17.

[37] McManis, J., Ferrel, R.E.Jr., Arman, A. (1983). Interpreting the physical properties of a clay using microanalysis technique. Geotech. Test. J., ASTM 6, 2, 87-92.

[38] Tovey, N.K. (1975). A mineralogical and microfabric study of Chek Lap Kok marine clay. Research Report No. Rr.3/85, Geotech. Control Office, Hong Kong, 138.

[39] Tovey, N.K. (1986). Microfabric, chemical and mineralogical studies of soils: techniques. J. Geotech. Engng, ASCE 17, 131-166.

[40] Jones, M. (1994). Mechanical principles of sediment deformation. In: Maltman, A. (Ed.), The Geological Deformation of Sediment. Chapman and Hall, London, 37-71.

[41] ASTM D 5550 (2000). Standard test method for specific gravity of soil solids by gas pycnometer. Annual Book of ASTM Standards 04.08, ASTM International, West Conshohocken, PA, USA.

[42] Kulkarni, M.P., Patel, A., Singh, D.N. (2010). Application of shear wave velocity for characterizing clays from coastal regions. J. Civil Eng. KSCE. 3, 14, 307-321.

[43] ASTM D 422-63 (1994). Standard test method for particle size analysis of soils. Annual Book of ASTM Standards 04.08, ASTM International, West Conshohocken, PA, USA.

[44] ASTM D 4318-93 (1994). Standard test methods for liquid limit, plastic limit, and plasticity index of soils. Annual Book of ASTM Standards 04.08, ASTM International, West Conshohocken, PA, USA.

[45] ASTM D 2487-06e1, (2006). Standard practice for classification of soils for engineering purposes (Unified Soil Classification System). Annual Book of ASTM Standards 04.18, ASTM International, West Conshohocken, PA, USA.

[46] Mousseau , R.J., and Trump, R. (1967). Measurement of electrical anisotropy of clay-like materials. Journal of Applied Physics 38, 11, 4375-4379.

[47] McCarter, W.J., Blewett, J., Chrisp, T.M., Starrs, G. (2005). Electrical property measurements using a modified hydraulic oedometer. Can. Geotech. Journal 42, 2, 655-662.

[48] Gumaste, S.D., Singh, D.N. (2010). Application of impedance spectroscopy for determining fabric anisotropy of fine grained soils. J. Test. Eval., ASTM 38, 3, 309-319.

[49] Arulanandan, K., Smith, S.S. (1973). Electrical dispersion in relation to soil structure. J. Soil Mech. Foundation Engineering, ASCE 99, 1113-1133.

[50] McCarter, W.J., Desmazes, P. (1997). Soil Characterization Using Electrical Measurements. Geotechnique 47, 1, 179-183.

[51] Rinaldi, V.A., Francisca, F.M. (1999). Impedance analysis of soil dielectric dispersion (1 MHz–1GHz), J. Geotech. Geoenviron. Eng., ASCE 125, 2, 111-121.

[52] Shah, P.H., Singh, D.N. (2004). A Simple Methodology for Determining Electrical Conductivity of Soils. J. ASTM Int. 1, 5, 1-11.

[53] Leon, A.C. (1998). New perspectives in mercury porosimetry, Advances in Colloid and Interface Science 76-77, 341-372.

[54] Guidi, G., Poggio, G., Petruzzell, G. (1985). The porosity of soil aggregates from bulk soil and from soil adhering to roots. Plant and Soil 87, 311-314.

[55] Anandrajah, A., Kuganenthira, N., and Zhao, D. (1996). Variation of fabric anisotropy of kaolinite

in triaxial loading. J. Geotech. Engg., ASCE 122, 8, 633-640.

[56] Collins, K., McGown, A. (1974). The form and function of microfabric features in a variety of natural soils. Geotechnique 24, 2, 223-254.

[57] Gorokhova, I.M. (1966). Theoretical fundaments for the evaluation of sedimentary rocks for engineering geological purposes. Nauka Publ., Moscow.

[58] Moon, H. Y., Kim, H. S., Choi, D. S. (2006). Relationship between Average Pore diameter and chloride diffusivity in various concretes. Const. Build. Mater. 20, 725-732.

[59] Li, S., Roy, D.M. (1986). Investigation of relations between porosity, pore structure, and C1– diffusion of fly ash and blended cement pastes. Cement Concrete Research 16, 5, 749-759.

[60] Gumaste, S. (2010). Determination of fabric of fine-grained soils, PhD thesis submitted to Civil Engineering Department, IIT Bombay.

[61] Blomqvist, S. (1991). Quantitative sampling of soft-bottom sediments: problems and solutions. Marine Ecology Progress Series 72, 295-304.

[62] Hvorslev, M.J. (1949). Subsurface exploration and sampling of soils for civil engineering purposes. U. S. Army Corps of Engineers, Waterways Experimental Station, Vicksburg, Mississippi.

[63] Bashar, M.A., Siddique, A., Safiullah, A.M.M. (1997). Effect of stress relief disturbance on undrained shear properties of Chittagong coastal soils. Journal of Civil Engineering, The Institution of Engineers, Bangladesh 25, 1, 65-77.

[64] Schjetne, K. (1971). The measurement of pore pressure during sampling. Proc. Speciality on Quality in Soil Sampling, 4th Asian Conference, ICSMFE, Bangkok, 12-16.

# U KORELACIJA MED TOČKOVNIM TRDNOSTNIM INDEKSOM $I_{s(50)}$ IN ENOOSNO TLAČNO TRDNOSTJO APNENCA IZ COMUNIDAD VALENCIANE (ŠPANIJA)

MANOLO GALVÁN, JORGE PRECIADO in JOSE SERÓN

## o avtorjih

**vodilni avtor**
Manolo Galván
University of Valle,
School of Civil and Geomatics Engineering,
Ciudad Universitaria Melendez, Cali, Kolumbija
E-pošta: manolo.galvan@correounivalle.edu.co

Jorge Preciado
Polytechnic University of Valencia,
Department of Geotechnical Engineering,
Camino de Vera S/N, Valencia, Španija
E-pošta: jpreciado@trr.upv.es

Jose Serón
Polytechnic University of Valencia,
Department of Geotechnical Engineering,
Camino de Vera S/N, Valencia, Španija
E-pošta: jbseron@trr. upv.es

## izvleček

*V mehaniki kamnin je enoosna tlačna trdnost ena od najpomembnejših lastnosti trdih kamnin, ki se uporablja za njihovo opisovanje in preučevanje obnašanja. Enoosno tlačno trdnost je mogoče oceniti tudi posredno iz točkovnega trdnostnega indeksa. V primeru dobre korelacije med obema parametroma je slednja metoda zelo uporabna, saj omogoča hitrejše in cenejše preizkušanje kamnin kot ostale metode. Prvi korak pri izpolnitvi te korelacije je izbira ustrezne metode za merjenje točkovne trdnosti kamnin. Le to je zanesljivejše, če obstaja zadostno število preiskav istovrstnih vzorcev, kar pa ni običajno, zato je potrebno uvesti ustrezen korekcijski faktor velikosti* $F = (D_e / 50)^{\alpha}$*, z* $\alpha = 0.45$*. Prispevek obravnava rezultate preiskav apnenca iz Comunidad Valenciane (Španija), ki predstavlja velik delež njihovih kamnin. V okviru študije je bilo izvedenih več kot 700 terenskih in laboratorijskih preiskav, med njimi 255 preiskav točkovnega trdnostnega indeksa in 45 preiskav enoosne tlačne trdnosti kamnin. Na vzorcih so bile določene še poroznost in specifična teža, vodoodpornost in ultrasonična hitrost.*

## ključne besede

odpor na točkovno obtežbo, točkovna trdnost, Franklin-ov preizkus, korekcijski faktor velikosti, enoosna tlačna trdnost

# CORRELATION BETWEEN THE POINT LOAD INDEX, $I_{s(50)}$, AND THE RESISTANCE TO UNCONFINED COMPRESSION IN LIMESTONE FROM THE COMUNIDAD VALENCIANA, SPAIN

MANOLO GALVÁN, JORGE PRECIADO and JOSE SERÓN

**about the authors**

**corresponding author**
Manolo Galván
University of Valle,
School of Civil and Geomatics Engineering,
Ciudad Universitaria Melendez, Cali, Colombia
E-mail: manolo.galvan@correounivalle.edu.co

Jorge Preciado
Polytechnic University of Valencia,
Department of Geotechnical Engineering,
Camino de Vera S/N, Valencia, Spain
E-mail: jpreciado@trr.upv.es

Jose Serón
Polytechnic University of Valencia,
Department of Geotechnical Engineering,
Camino de Vera S/N, Valencia, Spain
E-mail: jbseron@trr. upv.es

**Abstract**

*Unconfined compression strength is one of the most important engineering parameters in rock mechanics; it is used to characterize and study the behavior of solid rocks. A good correlation between the unconfined compression strength test (UCS) and the point load strength (PLS) can be very useful because it allows for faster and cheaper testing than others with the same security to calculate the structures and performances of solid rocks. A preliminary step to implement the correlation is to have a good method to determine resistance to point load. This determination is quite correct if you have a sufficient number of tests on specimens of the same nature, but usually it does not occur and it is necessary to apply a size correction factor,* $F = (D_e / 50)^{\alpha}$*, with* $\alpha = 0.45$*. This paper is based on limestone from Comunidad Valenciana (Spain) because it represents a very high percentage of their rocks. The implementation has been conducted over 700 field and laboratory tests of which 255 are PLT test, 45 are UCS test, and the rest are other parameters like: porosity and specific weight, Slake Durability, and ultrasonic velocity, among others.*

**keywords**

resistance to point load, point load strength, Franklin test, size correction factor, unconfined compression

## 1 INTRODUCTION

The unconfined compression strength (UCS) is a fundamental parameter that is often costly, difficult, or even impossible to determine through normalized testing [1, 2, 3]; however, it may be determined with a simple geologist hammer or with the Schmidt hammer, among others [3]. But for more approximate values it may be obtained via simple in situ or laboratory tests, like the Brazilian traction test or the Point Load Test (PLT).

The different field and/or laboratory test methods to obtain more or less precisely, or at least estimate, the unconfined compression strength, $\sigma_c$, are summarized in Table 1.

**Table 1**. Methods for determining the unconfined compression strength, [4]

| Application | Method | Is obtained by |
|---|---|---|
| Field Test | Organoleptic tests | Subjective estimate |
| | Schmidt hammer | Objective estimation |
| Laboratory test | Point load test | Correlation |
| | Brazilian Traction | |
| | Unconfined compression strength | Direct measurement |

The Point Load Test (PLT) allows us to determine the Point Load Resistance Index or Point Load Strength, ($I_{s(50)}$). It is useful in classifying rocks by their resistance. Ever since its emergence, Franklin and other researchers have proposed a correlation with UCS [5], but this value should be adjusted according to the genesis of the different rock masses.

The PLT uses specimens formed by regular and irregular rock fragments or cylindrical specimens [6, 7] (generally from probes) that are not subjected to strict requirements to be admissible. This test may take place *in situ* or in the laboratory. This work presents the most appropriate values correlating PLT and UCS in limestone from a broad zone in eastern Spain, and proposing a value.

## 2 EXPERIMENTAL WORK

The samples tested in this research were collected from eight different locations in the Comunidad Valenciana, Spain, and come from healthy limestone masses that present a maximum equidistance of 140 km and a mean equidistance of 95 km. The largest excavations were conducted on Roadway CV-13, Torreblanca section (Castellón) and in the probes for the Project for the Cullera Tunnel (Valencia). The other investigations took place on the access road to the Loriguilla Reservoir (Valencia), Roadway N-332, Gandia section (Valencia), the Sierra Gorda quarry in Bellús (Valencia), the Guerola quarry in Onteniente (Valencia), a slope in Puebla de Arenoso (Castellón), and on the clearings to broaden Roadway A–7 in the Port of Albaida (Alicante).

With the samples from Roadway CV-13-Torreblanca, 44 Point Load (PL) tests were carried out in the laboratory, on controls carved into regular block shapes or cylinders, subjected to axial or diametric loads (diameters of 45 and 54 mm). To determine the UCS, we conducted ten tests (five with measurement of deformations through strain gauges) for diameters of 45 and 54 mm. The study zone exhibited limestone with karst evidence of the Upper Cretaceous, the rocky mass showed fractured sections and others that clearly revealed the structure of the mass.

For the Cullera Tunnel, 103 PL tests were conducted *in situ* with cylindrical controls, having diameters between 45 and 85 mm. For the UCS, 21 tests were performed (nine with strain gauges) using controls with diameters between 47 and 84 mm. Geologically, the zone crossed by the probes is fundamentally comprised of formations from the Upper Cretaceous: crystalline dolomite, limestone, polygamous breccias and marlstone.

On the access to the Loriguilla Reservoir, 10 PL tests were carried out in the laboratory, with irregular controls and carved with a regular block form and a cylinder (45-mm diameter). For the UCS, three tests were made with a measurement of the deformation through strain gauges (45-mm diameter). Lithologically, these were pisolitic and/or oolitic limestone from the Jurassic period.

With the samples from the roadworks being conducted to broaden the roadway surface on Roadway N-332 between Gandía and Xeresa, eight PL tests were conducted between the field and the laboratory, with controls in regular block form and cylindrical form using a diametric load (49-mm diameter). For the UCS, four tests were carried out, using controls with a 49-mm diameter. The zone is on a fringe of beige micritic limestone and Cretaceous age, massive but affected by some fracturing and karst processes.

At the Sierra Gorda quarry in Bellús, 65 samples were extracted from the same block for PLT (regular blocks) and four for UCS (with measurement via strain gauges). The zone is located in sandy marls with limestone intercalations, most frequently towards the top part, which contain worm, hedgehog, and Inoceramus tracks (bioturbations).

Seeking a better correlation with the limestone subjected to the study, the research was broadened to include the following sites:

Guerola quarry in Onteniente, where eight PL tests were carried out along with a UCS test. The lithostratigraphic series presented great continuity of the sedimentation since the Neocomian to the Pliocene, given that practically all the floors are represented in which, currently, the Cretaceous and the Tertiary periods are divided.

Slope in Puebla de Arenosa with nine PL tests and one UCS test. The geology in the zone has an alternating series, sometimes metric, massive and marl limestone or marlstone less highlighted. This unit loses carbonate laterally with the appearance of alternations that have a lower content of limestone which have been denominated alternations of marls, marl limestone and limestone.

Clearings in the broadening of A–7 in the Port of Albaida, with eight PL tests and one UCS test. The study zone has a geology composed of a 100-m thickness, comprising microcrystalline limestone clay processes quite similar to the prior, but displaced in a fine, wavy, and sometimes leafy stratification, yellowish marl interbanks are very frequent, particularly towards the upper part of the package.

The numbering system shown in Table 2 will be used for the whole text.

**Table 2**. Location of the study sites in the Comunidad Valenciana

| SITE | PROJECT / WORK |
|---|---|
| 1 | Excavations on roadway CV–13 |
| 2 | Specimens of the Cullera tunnel project |
| 3 | Access slope to the Loriguilla reservoir |
| 4 | Slope on N–332 in Gandía – Xeresa |
| 5 | Sierra Gorda quarry in Bellús |
| 6 | Clearing in Puebla de Arenoso |
| 7 | Causeway on A–7 (Port of Albaida) |
| 8 | Guerola quarry in Onteniente. |

# 3 TESTS PERFORMED

For a better follow up of the results obtained, the following briefly reviews the tests performed in this research.

## 3.1 INDEX AND ALTERABILITY PROPERTIES

The samples subjected to PLT and UCS were measured and weighed in terms of their volume, density, specific weight, humidity, and the specific relative weight of the particles in order to know with a good approximation the total porosity of the samples. Likewise, their alterability was analysed via static and dynamic immersion tests, through the Dusseault test [8], and the Slake-Durability test [9], respectively, which determines their alterability against water immersion cycles with pounding. The values obtained were used for an upcoming publication.

## 3.2 POINT LOAD TEST (PLT)

The Point Load Test is also known as the Franklin test. The first reference is by Reichmuth, D. (1968) [10], who proposed obtaining the resistance to a point load and a determination of the unconfined compression strength via correlation, regardless of whether they are irregular, regular, or cylindrical rock controls [11]. This test has not been designed for soft rocks or with anisotropy, although its application according to the norm permits an "anisotropy index" ($I_a$) in terms of the function of the results obtained with the application of the load in a parallel and perpendicular manner to the anisotropy planes.

The PLT has two clear advantages: one is the portability of the press, which permits its use in the laboratory and *in situ* (outcrops, probing, or excavations); the other advantage, and the main one, is the requirement level on the samples to be tested, only requiring some geometric minimums (Table 3), with an indispensible condition that the rupture of the specimen is produced by a fracture plane (or several) that contain the two points of the load application (Figure 1).

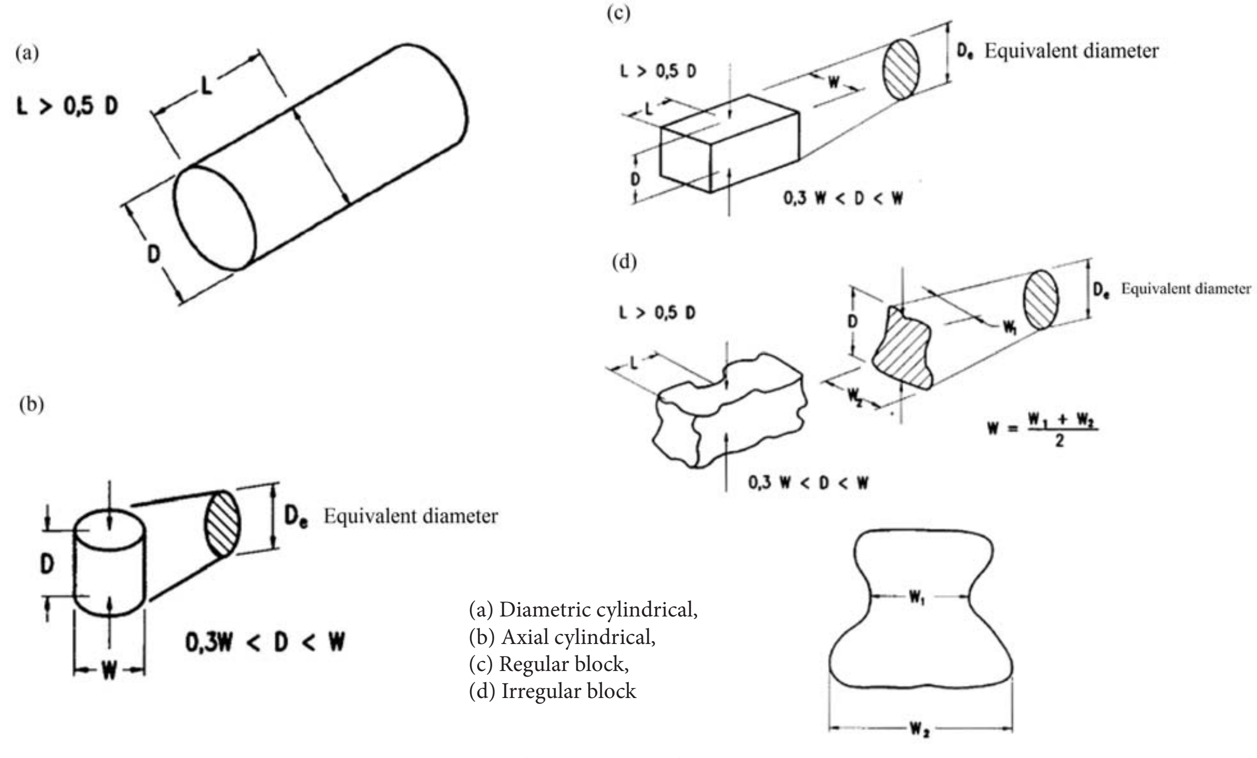

(a) Diametric cylindrical,
(b) Axial cylindrical,
(c) Regular block,
(d) Irregular block

**Figure 1**. Geometric requirements of the specimens for the Point Load Test (UNE 22950-5:1996).

**Table 3**. Geometric requirements of the specimens for the Point Load Test (Source: author's work).

| Type of test | Distance between load points (D) | Length of the specimen (L) | Width of the specimen | | |
|---|---|---|---|---|---|
| | | | Less ($W_1$) | Higher ($W_2$) | Medium (W) |
| Diametric cylindrical | D | L > 0.5 D | - | - | - |
| Axial cylindrical | 0.3 W < D < W | - | - | - | W |
| Regular block | 0.3 W < D < W | L > 0.5 D | - | - | W |
| Irregular block | 0.3 W < D < W | L > 0.5 D | $W_1$ | $W_2$ | ½ ($W_1$+$W_2$) |

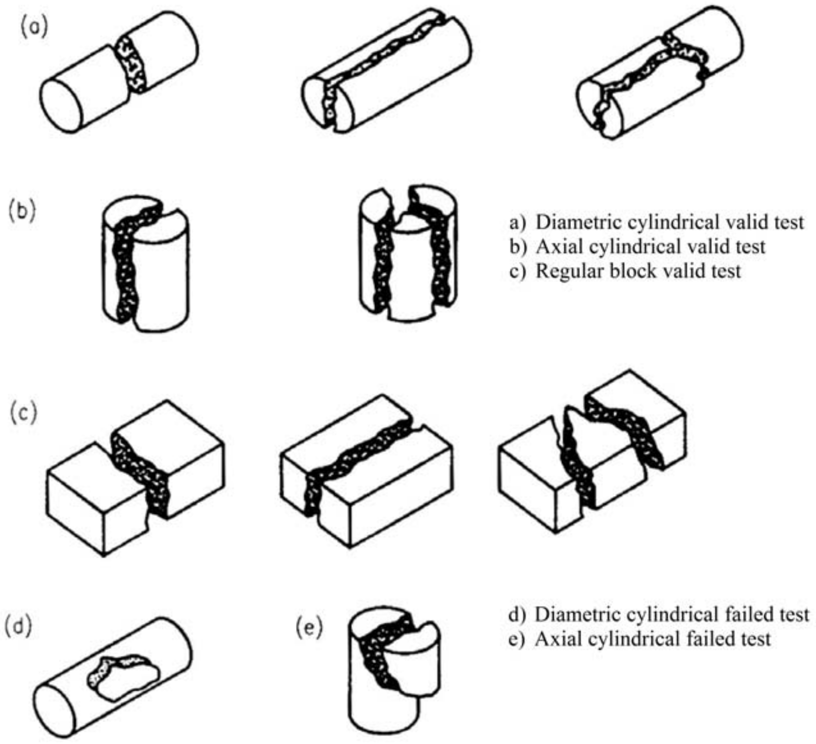

**Figure 2**. Rupture forms for valid and null tests [7].

The PLT is normalized for cylindrical specimens that are 50 mm in diameter, obtaining the Point Load resistance index, $I_{s(50)}$. When the diameter of the sample subjected to a diametric load (or the equivalent diameter, $D_e$, for other types of specimens and loads) differs from 50 mm, we should correct by size.

This correction by size is carried out by testing the samples with diverse sizes, whose breaking loads are represented against $D_e^2$, in double logarithmic scale, obtaining for $D_e^2$ = 2.500 mm$^2$ the value of $P_{50}$, by interpolation or extrapolation. The points represented in this graphic should be aligned along a straight line, ignoring (although not suppressing) those deviating substantially from the line.

When few controls are available to conduct a curve for the correction by size, we can use the following correction factor *F*, proposed in the norm:

$$F = \left(\frac{D_e}{50}\right)^{0.45} \qquad (1)$$

where $D_e$ is the equivalent diameter.

In this case, the Point Load resistance index is obtained as:

$$I_{s(50)} = \frac{P_{50}}{50^2} \qquad (2)$$

where $I_{s(50)}$ is the Point Load index normalized to a cylindrical specimen of 50 mm in diameter, subjected to a diametric test.

$P_{50}$ is the tensile strength to the point load for a diametric test with a cylindrical specimen of 50 mm in diameter or rather with the correction by size:

$$I_{s(50)} = F \cdot I_s = F \cdot \frac{P}{D_e^{\,2}} \qquad (3)$$

The resistance to the point load is also an identifying parameter for the geomechanic characteristics of the rock, similar to how they are classified according to their unconfined compression strength. (Table 4).

The habitual ranges of the Point Load Index for diverse types of rocks are shown in Figure 3; this scale is one of the most used in rock mechanics.

## 3.3 TEST OF UNCONFINED COMPRESSION STRENGTH (UCS)

The unconfined compression strength was determined directly through a “Test of the unconfined compression resistance” (UCR).

**Table 4**. Classification of rocks in terms of their resistance to a point load [12].

| $I_{s(50)}$ (MPa) | Resistance to point load | |
|---|---|---|
| | Author: Garnica et al, 1997 | Author: Carol, 2008 |
| < 0. 03 | Extremely low | Very low |
| 0.03–0.1 | Very low | |
| 0.1–0.3 | Low | Low |
| 0.3–1.0 | Moderate | Medium |
| 1.0–3.0 | High | High |
| 3.0–10.0 | Very high | Very high |
| > 10.0 | Extremely high | Extremely high |

The test consists of applying an axial force $F_c$ to a cylindrical specimen of area $A$, bringing it to rupture with a press. The resistance is given by the equation:

$$\sigma_c = \frac{F_c}{A} \qquad (4)$$

The requirements according to the UNE 1990 norm [2] for the specimens to be tested are:

1. Cylindrical shape with dimensions:
    - Height/diameter ratio from 2.5 to 3.0.
    - Diameter, over 10 times the rock’s maximum grain size.
    - Diameter, not less than 50 mm.

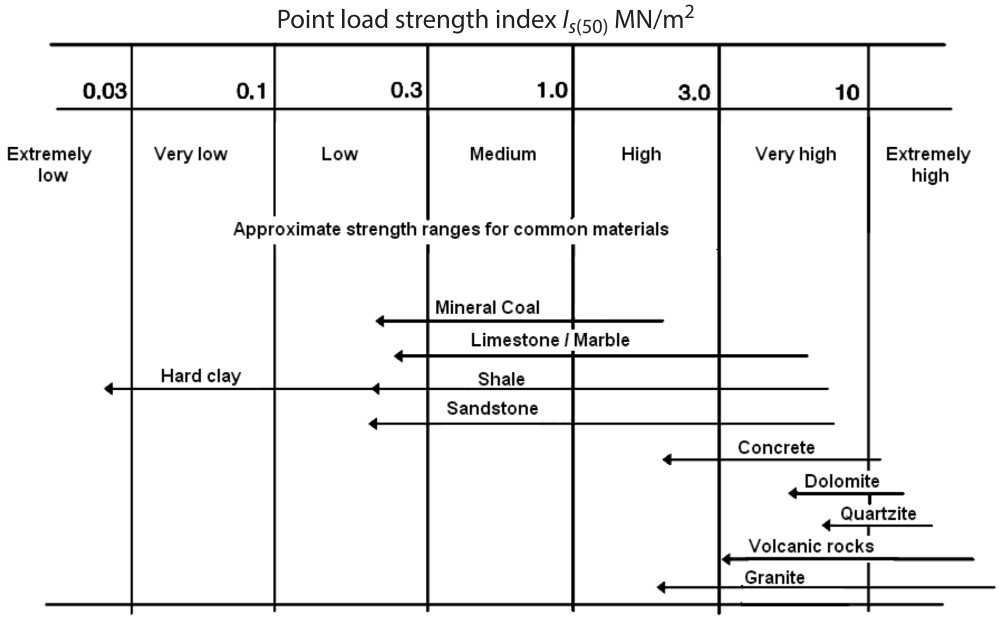

**Figure 3**. Variation of the Point Load Indexes for different types of rocks [4].

2. The specimens will be elaborated through perforation, turned cuts and polishing or any other appropriate method, so that:
    - The lateral surface of the specimen is smooth and free of irregularities.
    - The bases must be flat and form a straight angle with the axis of the specimen.
    - Avoid using coating materials as equalizers to achieve the parallelism required for the bases of the test specimen. If it was necessary to deviate from this norm due to the characteristics of the material to be tested, this must be indicated in the test protocol.

The tolerances of their elaboration will be those indicated in Table 5.

**Table 5**. Tolerance of the elaboration of rock specimens for the unified compression test [2].

| Tolerance for | Deformability of the rock | | |
|---|---|---|---|
| | Little | Medium | High |
| Deviation of the generatrix with respect to the axial direction | ±0. 3 mm | ±0.4 mm | ±0.5 mm |
| Flatness of the base | ±0.02 mm | ±0.5 mm | ±0.1 mm |
| Deviation with respect to right angle, the angle of the axis of the cylinder with the base | 10´ | 20´ | 30´ |

Hence, the requirements regarding the sample to be tested are not easy to fulfil and are sometimes impossible, as described in the following.

*Regarding the elaboration of the specimens:*

### 3.3.1 Tolerance

Regarding the tolerance on the surface finishes (primarily on the lateral surfaces), it is habitual for the perforation systems and the nature of the rocks leads to us not being able to meet the requirements (Table 5).

### 3.3.2 Equipment

Special equipment is required for drilling and cutting, and above all for polishing; costly equipment, as well as the consumables are used (diamond dust, etc.), which are practically not available in any laboratory.

### 3.3.3 Facing

The facing issue is of special importance. The ISRM recommendations did not permit any system that was not mechanical; the current Spanish norm, [2], preserves that imposition, but indicates that: "If it were necessary to deviate from this norm due to the characteristics of the material to be tested, it must be indicated in the test protocol", leading to the generalization of the already-extended custom of facing the specimens with sulphur.

*Regarding specimen dimensions:*

### 3.3.4 Length

Discontinuities of the rocky core may hinder the obtaining of rock cylinders with sufficient length ($L$>125 to 150 mm, between two planes perpendicular to the axis, for 50-mm diameter).

### 3.3.5 Grain size

In rocks formed by thick grains (> 5 mm) the diameter of the specimen must be over 50 mm; in cases of some rocks with centimetre grains or clasts, the proportions of the specimens are practically impossible to obtain (and in the case of it being possible, it may not be broken with just a conventional press).

### 3.3.6 Correction of the size and shape of the specimen

Also, even if all the recommendations of the norms are fulfilled, no general and unique formulation is available to permit extrapolating the results of the tests of the real in situ conditions of the rocky core. The variation of the compression strength of the matrix depends on the size (diameter) and form (height/width) of the specimen.

It has been observed that the resistance diminishes as the specimen size increases, given that, among other things, when the size increases it is more likely for a structural defect to appear and develop the rupture of the rock.

Figure 4 shows the results of the unconfined compression tests performed on samples from different lithologies [13]. The values from these tests were divided by the resistance of a rock specimen that awas 50 mm in diameter, for each lithology presented. In this way, the data presented are dimensionless and, furthermore, differences due to humidity content, load rate, etc., are eliminated.

The unconfined compression strength, $\sigma_c$ , for a sample of diameter $d$, is related to that corresponding to a 50-mm diameter ($\sigma_{c50}$) with:

$$\frac{\sigma_c}{\sigma_{c50}} = \left(\frac{0.05}{d}\right)^{0,18} \qquad (5)$$

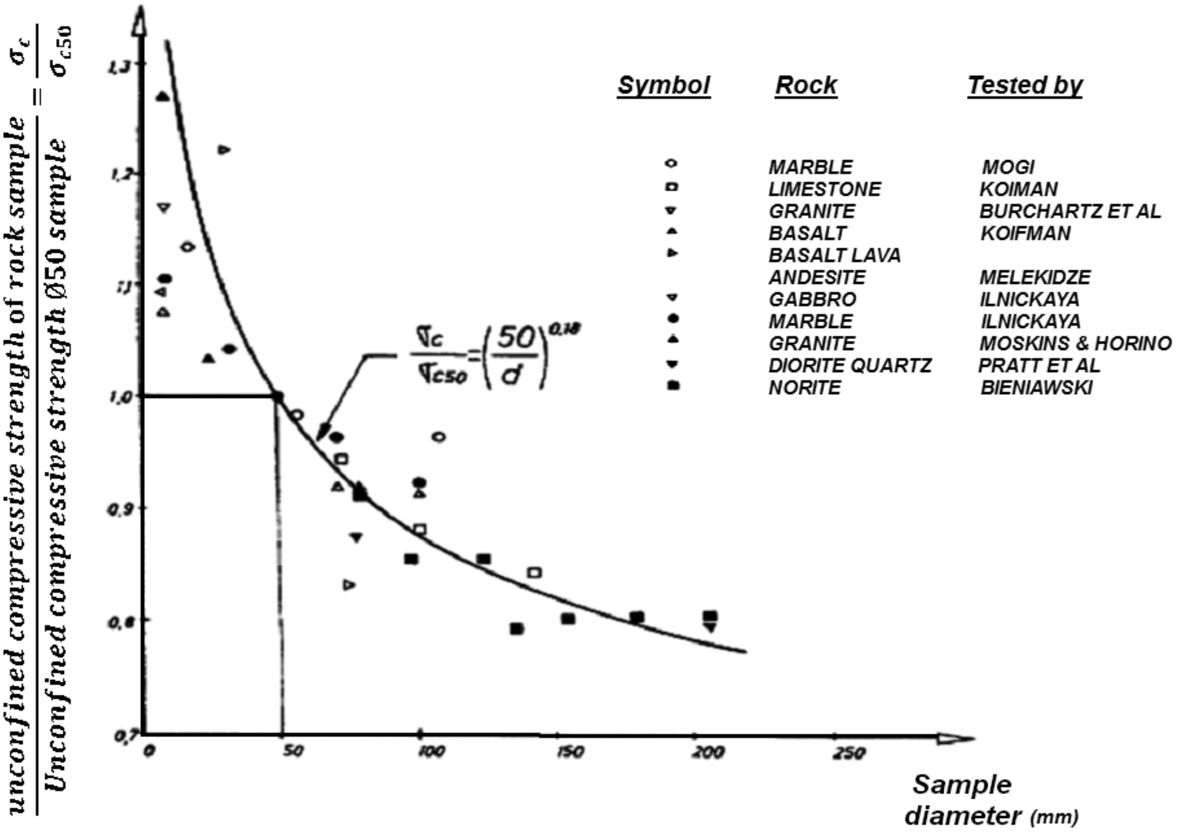

**Figure 4**. Variation of UCS with specimen diameter [13], in [14].

Likewise, the resistance increases with a diminished height/width ratio and it is greater when the confinement of the control increases. The critical size is defined as a specimen size for which an increase in its dimensions does not result in an appreciable decrease of its resistance. However, this test is the most widely accepted value to know the resistance to compression of a rocky core.

In tests for UCS in this research, loads were applied from 11.4 to 161.2 MPa, at a rate of 0.5 MPa/s, for six different types of diameters (83, 71, 63, 54, 48, 45 mm) for a total of 45 tests. The highest value found for the unconfined compression strength in the limestone tested was 161.2 MPa for a 45-mm diameter; the lowest was 11.4 MPa for a 71-mm diameter.

## 4 RESULTS

A total of 255 point load resistance tests were performed, in situ and in the laboratory, on all types of specimens, brought to rupture through an axial and diametric load. The tests were executed with equivalent diameters from 24 to 82 mm and $I_{s(50)}$ values were obtained from 1.21 to 6.40 MPa. The results were studied for four resistance sub-groups. For this, a statistical analysis was performed of the measurements by lithology groups (Table 5).

## 5 STATISTICAL TREATMENT

As mentioned in Section 2, there are eight points in the Comunidad Valenciana (Table 2), and this numbering system will continue to be used.

In the first place, the comparison of the samples tested by works (site) was conducted with the $I_{s(50)}$ variable, shown in the box-and-whisker chart in Figure 5.

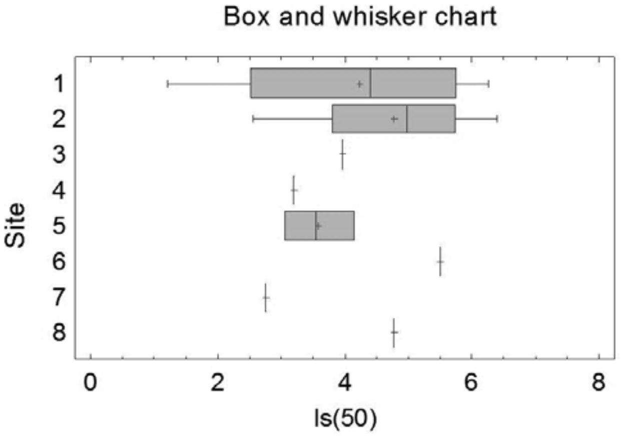

**Figure 5**. $I_{s(50)}$ box-and-whisker chart (all tests).

With this procedure we compared the values obtained via a statistical test; F-test in the analysis of variance chart (Table 6) tests for any significant difference among the measurements.

**Table 6**. Analysis of variance for $I_{s(50)}$.

| Variance analysis | | | | | |
|---|---|---|---|---|---|
| Source | Sums of Squares | DF | Mean Square | Coefficient-F | P-Value |
| Among groups | 9.55454 | 7 | 1.36493 | 0.67 | 0.6925 |
| Within the groups | 54.7059 | 27 | 2.02615 | | |
| Total | 64.2605 | 34 | | | |

The $I_{s(50)}$ analysis of variance chart breaks down the variance of data into two components: a component among groups and a component within each group. The F-ratio, which in this case is equal to 0.67, is the quotient of the estimation among the groups and the estimation within the groups. Given that the p-value of the F-test is above 0.05, there is no statistically significant difference among the measurements from the 8 points in the Comunidad Valenciana with a 95% confidence index. In the multiple range contrast analysis for $I_{s(50)}$ , no statistically significant differences were noted between any pair of measurements at the 95% confidence level. It was also noted that all the groups are homogeneous.

Then the measurements were compared with the σc variable and Figure 6 (box-and-whisker chart) shows the mean, median, and the first and third quartiles.

The analysis of variance chart F-test (Table 7) tests for any significant difference among the measurements.

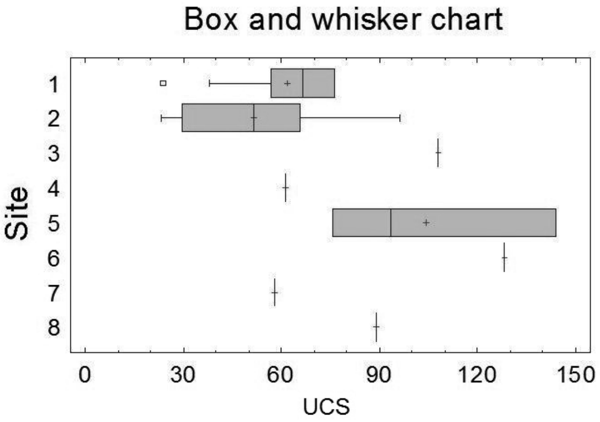

**Figure 6**. $\sigma_c$ box-and-whisker chart (all tests).

The coefficient F in Table 7, which in this case is equal to 4.33, is the quotient of the estimation among the groups and the estimation within the groups. Given that the p-value for the F-test is below 0.05, indicating statistically significant differences among the measurements from the 8 points in the Comunidad Valenciana at a 95% confidence level.

**Table 7**. Analysis of variance for $\sigma_c$.

| Variance analysis | | | | | |
|---|---|---|---|---|---|
| Source | Sums of Squares | DF | Mean Square | Coefficient-F | P-Value |
| Among groups | 13465.5 | 7 | 1923.7 | 4.33 | 0.0025 |
| Within the groups | 11981.9 | 27 | 443.7 | | |
| Total | 25447.8 | 34 | | | |

**Table 8**. Multiple range contrast for $\sigma_c$.

| Method: 95 LSD percentage | | | | | |
|---|---|---|---|---|---|
| Site | Frequency | Mean | Homogeneous groups | | |
| 1 | 15 | 61.8 | X | | |
| 2 | 12 | 51.4 | X | | |
| 3 | 1 | 108.0 | | X | X |
| 4 | 1 | 61.2 | X | X | |
| 5 | 3 | 104.3 | | X | X |
| 6 | 1 | 128.3 | | | X |
| 7 | 1 | 57.9 | X | X | |
| 8 | 1 | 88.9 | X | X | X |

In conclusion, to make a correlation between the resistance to ultimate compression and $I_{s(50)}$ , it is necessary to perform a multiple range test for the UCS and group them thus (Table 8).

Table 8 applies a multiple comparison procedure to determine the measurements that are significantly different from the others. It may also be noted that three homogeneous groups were identified, according to the alignment of the X sign in the column, meaning that no significant Fisher (LSD) differences exist among the homogeneous groups.

## 6 UCS REGRESSION ANALYSIS AGAINST PLT

Initially, a linear regression was performed, defining the ratio between the independent and dependent variables. The correlations were made for the three types of homogeneous groups (Table 8), obtaining the four main homogeneous subgroups according to the multiple contrast for $\sigma_c$ , which are shown in the following:

**Table 9**. Correlation for subgroup 1.

| Series | Homogeneous Groups |
|---|---|
| 🟨 | 1 y 2 |
| ▲ | 4, 7 y 8 |
| ◆ | 3, 5 y 6 |

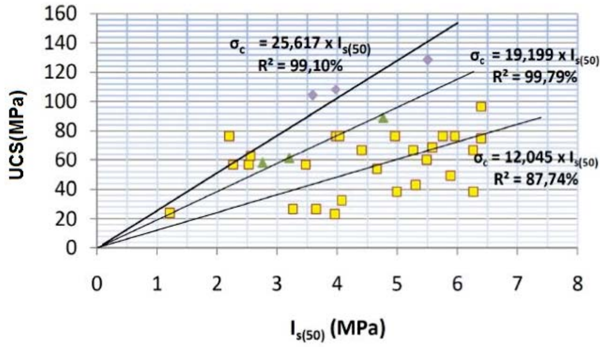

**Figure 7**. $\sigma_c$ regression and the $I_{s(50)}$ (Subgroup 1).

**Table 10**. Correlation for subgroup 2.

| Series | Homogeneous Groups |
|---|---|
| 🟨 | 1 y 2 |
| ▲ | 3, 4 y 7 |
| ◆ | 5, 6 y 8 |

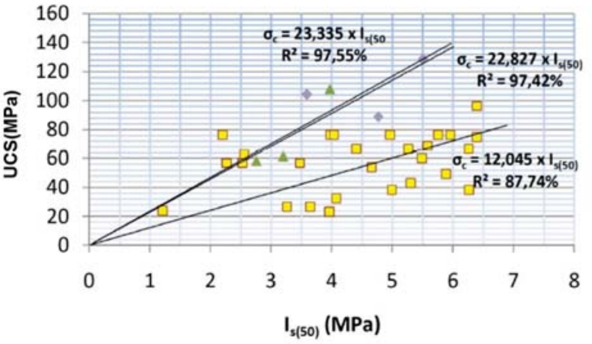

**Figure 8**. $\sigma_c$ regression and the $I_{s(50)}$ (Subgroup 2).

**Table 11**. Correlation for subgroup 3.

| Series | Homogeneous Groups |
|---|---|
| 🟨 | 1, 2 y 7 |
| ▲ | 4, y 8 |
| ◆ | 3, 5 y 6 |

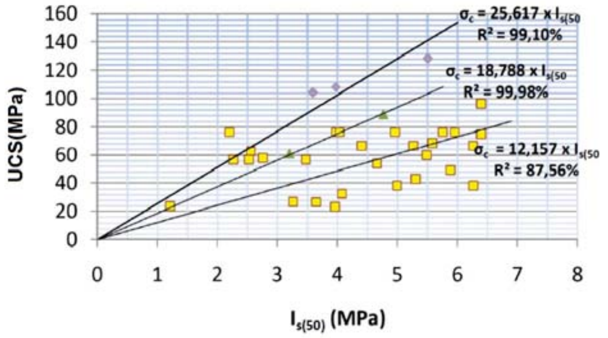

**Figure 9**. $\sigma_c$ regression and the $I_{s(50)}$ (Subgroup 3).

**Table 12**. Correlation for subgroup 4.

| Series | Homogeneous Groups |
|---|---|
| 🟨 | 1 y 2 |
| ▲ | 3, 5 y 7 |
| ◆ | 4, 6 y 8 |

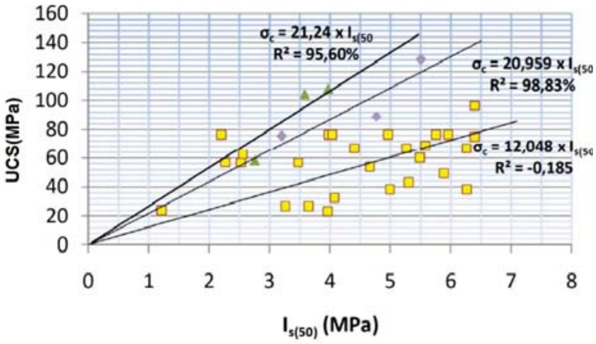

**Figure 10**. $\sigma_c$ regression and the $I_{s(50)}$ (Subgroup 4).

In general, the summary of the correlations for the four subgroups is shown in Table 13.

**Table 13**. Summary of correlations for the 4 subgroups.

| Subgroup | $R^2$ | UCS |
|---|---|---|
| 1 | 99.79% | 19.199 x $I_{s(50)}$ |
| 2 | 97.55% | 23.335 x $I_{s(50)}$ |
| 3 | 99.98% | 18.788 x $I_{s(50)}$ |
| 4 | 98.83% | 20.959 x $I_{s(50)}$ |

## 7 CONCLUSIONS AND DISCUSSION

The indirect methods used to estimate the stress parameters in the rocky core are numerous and varied, but if the norms are followed and all the procedures are performed, the values may be coherent and close to reality.

One of the most common methods is the linear correlation between UCS and $I_{s(50)}$, the latter is obtained in the PLT (Equation 6).

$$\sigma_c = \beta \times I_{s(50)} \qquad (6)$$

It was proven that there is no unique value of $\beta$ for all rocks (Table 14), as initially proposed by Broch and Franklin [11]; the results herein show that for the same type of rock (limestone) the obtained values of $\beta$ are between 12 and 26.

Table 14 summarizes the most important results of the $\beta$ factor for all the conducted tests.

**Table 14**. Summary of correlations.

| $\beta$ | $R^2$ (%) | Places of the C.V. |
|---|---|---|
| 13.612 | 84.48 | 8 points of C.V |
| 12.045 | 87.74 | CV-13 and Cullera |
| 12.157 | 87.56 | CV-13, Cullera and Puerto Albaida |
| 19.199 | 99.79 | N-332, Puerto Albaida and Onteniente |
| 22.827 | 97.42 | Loriguilla, N-332 and Puerto Albaida |
| 18.788 | 99.98 | N-332 and Onteniente |
| 20.959 | 98.83 | Loriguilla, Bellús and Puerto Albaida |
| 25.617 | 99.10 | Loriguilla, Bellús and Puebla de Arenoso |
| 23.335 | 97.55 | Bellús, Puebla de Arenoso and Onteniente |
| 21.240 | 95.60 | N-332, Puebla de Arenoso and Onteniente |

Table 14 shows the set of subgroups statistically separate. The subgroups that have a better correlation (shaded in grey) have $R^2$ values greater than 87%.

Other researchers have found similar values of $\beta$ for various types of rocks (Table 15).

**Table 15**. Estimated values of the coefficient to apply in the point load strength [17].

| Rock types | Strength | $C_0/I_{s(50)}$ |
|---|---|---|
| Igneous, compact | Medium-High | 20-25 |
| Foliated metamorphic | Medium-High | 16-22 |
| Foliated metamorphic | Low | 12-16 |
| Well-cemented calcareous | Medium-High | 18-24 |
| Well-cemented sedimentary | Low | 10-15 |
| Poorly cemented sedimentary | Low | 6-10 |

However, when $\beta$ is obtained for a concrete lithology (subgroups 1, 2, 3, 4) of Table 14, a correlation coefficient above 87% is presented. This suggests the existence of an adequate $\beta$ for a specific lithology, but when seeking to widely use the determination of $\sigma_c$ with $I_{s(50)}$, it is convenient to carry out a prior "calibration" with a UCS test to permit establishing the most appropriate $\beta$.

Here we found that when having to use a value of $\beta$ for "limestone-type" rocks from the Comunidad Valenciana the "mean" value is $\beta$=13.6.

Finally, for future research, we suggest investigating the correlation of σc with the $I_{s(50)}$, controlling the humidity content of each sample to be tested, given that a high impact has been detected in the results.

## REFERENCES

[1] ASTM International (2009). D 7012-04 Standard test method for compressive strength and elastic modulus of intact rock core specimens under varying states of stress and temperatures, West Conshohocken, USA.

[2] UNE (1990). Parte 1, ensayos para la determinación de la resistencia: Resistencia a la compresión uniaxial 22-950-90, AENOR. Madrid, España.

[3] Çobanoğlu, İ., Çelik, S.B. (2008). Estimation of uniaxial compressive strength from point load strength, Schmidt hardness and P-wave velocity. Bull Eng. Geol. Environ. 67, 491-498. DOI 10.1007/s10064-008-0158x.

[4] Serón, J.B. (1997). Propiedades básicas de las Rocas. Aplicación a las clasificaciones geomecánicas. I Curso sobre tecnología de métodos modernos de sostenimiento de Túneles, Valencia. España, 17.

[5] Romana, M. (1999). Correlation between uniaxial compressive and Point Load (Franklin test)

strength for different rock classes. In: 9th ISRM Congress, Paris, France, 1, 673-676l.
[6] ASTM International (2009). D 5731-05 Standard test method for determination of the point load index of Rock, West Conshohocken. U.S.A.
[7] UNE (1995). Parte 5, ensayos para la determinación de la resistencia: resistencia a Carga Puntual, AENOR, 22-950-95,Madrid, España.
[8] Normas del Laboratorio de Transportes NLT. Estabilidad de áridos y fragmentos de roca frente a la acción de desmoronamiento en agua 255/99, Madrid, España.
[9] International Society for Rock Mechanics ISRM. Test al desmoronamiento (Slake durability) 21997, Lisboa, Portugal.
[10] Reichmuth, D.R. (1968). Point-load testing of brittle materials to determine tensile strength and relative brittleness. Proceedings of the ninth symposium on Rock Mechanics. University of Colorado, 134-159.
[11] Broch, E., Franklin, J.A. (1972). The point load test. International Journal Rock Mechanics, Mining and Science 9, 669-697.
[12] Garrido, M.E., Hidalgo, C., Preciado, J.I. (2010). Prácticas de laboratorio geotecnia y cimientos I. Departamento de Ingeniería del Terreno. Universidad Politécnica de Valencia, Ref.:2010.418, Editorial UPV.
[13] Hoek and Brown (1980). Underground excavations in Rock. Institution of Mining and Metallurgy, London.
[14] Instituto Tecnológico Geominero de España (ITGE) (1991). Mecánica de rocas aplicada a la minería metálica subterránea. Ministerio de Industria, Comercio y Turismo. Secretaria general de la Energía y Recursos Minerales, 160.
[15] Preciado, J.I. (2008). Ensayos de laboratorio, Geotecnia y Cimientos II [Diapositiva]. Valencia, España: Universidad Politécnica de Valencia.
[16] Serón, J.B., Preciado, J. (2007). Instrumentación geotécnica [Apuntes de clase]. Ref. 2007.113, Valencia, Universidad Politécnica de Valencia.
[17] Romana, M. (1994). Test de compresión puntual de Franklin. Revista de Ingeniería Civil, 116-120.

# EKSPERIMENTALNA RAZISKAVA VARIIRANJA PRITISKA PORNE VODE S KONSOLIDACIJSKIM TESTOM PRI KONSTANTNIH SPECIFIČNIH DEFORMACIJAH

HOJJAT AHMADI, HASSAN RAHIMI, ABBAS SOROUSH in CLAES ALÉN

## o avtorjih

Hojjat Ahmadi
Urmia University,
Water Engineering Department
Urmia, Iran
E-pošta: hojjat.a@gmail.com

Hassan Rahimi
University of Tehran,
Irrigstion Department, Soil & Water Eng. College
Teheran, Iran

Abbas Soroush
Amirkabir University of Technology,
Civil and Environmental Engineering Department
Teheran, Iran

Claes Alén
Chalmers University of Technology,
Civil Engineering Department
Gothenburg, Švedska

## izvleček

*Konsolidacija pri konstantnih specifičnih deformacijah je preiskava, ki se uporablja za hitro določanje stisljivosti glinenih zemljin. Pri preiskavi se izbere primerno stopnjo specifične deformacije glede na razmerje med pornim pritiskom in totalno napetostjo. Da bi raziskali učinek stopnje specifične deformacije na variiranje pornega tlaka, so bili preiskani štirje vzorci gline različno plastične gline. Rezultati preizkusov so pokazali, da je tendenca variiranja pritiska porne vode odvisna od režima odtekanja vode, ki je lahko Darcyev ali ne-Darcyev, prav tako pa tudi, da plastičnost glin nima upoštevanja vrednega učinka na variiranje pritiska porne vode.*

## ključne besede

konstantne specifične deformacije, konsolidacija, stopnja pornega vodnega tlaka, plastičnost zemljin, Darcyjev in ne-Darcyjev tok

# EXPERIMENTAL RESEARCH ON VARIATION OF PORE WATER PRESSURE IN CONSTANT RATE OF STRAIN CONSOLIDATION TEST

## HOJJAT AHMADI, HASSAN RAHIMI, ABBAS SOROUSH and CLAES ALÉN

### about the authors

Hojjat Ahmadi
Urmia University,
Water Engineering Department
Urmia, Iran
E-mail: hojjat.a@gmail.com

Hassan Rahimi
University of Tehran,
Irrigstion Department, Soil & Water Engineering College
Tehran, Iran

Abbas Soroush
Amirkabir University of Technology,
Civil and Environmental Engineering Department
Tehran, Iran

Claes Alén
Chalmers University of Technology,
Civil Engineering Department
Gothenburg, Sweden

### Abstract

*Constant rate of strain (CRS) consolidation is a rapid test method which is used for determination of compressibility of clayey soils. In a CRS test, the appropriate strain rate is selected based on pore water pressure ratio, i.e. the ratio of pore pressure to total stress. In the present study, to investigate the effect of strain rate on variation of pore water pressure ratio, four different clay samples of different plasticity were tested by CRS apparatus. The results of the experiments showed that the trend of variation of pore water pressure is dependent on the drained water flow regime which may be either Darcy or non-Darcy. The results also indicated that the plasticity of clay does not have considerable effect on variation of pore water pressure.*

### Keywords

constant rate of strain, consolidation, pore water pressure ratio, soil plasticity, Darcy and non-Darcy flow

## 1 INTRODUCTION

In the standard CRS consolidation test a soil sample with thickness ranging from 10 to 30 mm (normally 20 mm), is contained within a consolidation cell, and compressed while subjected to a constant rate of displacement using a standard triaxial loading apparatus. During the test, specimen is drained from one side and developed excess pore pressure measured at the other side. Selection of appropriate displacement rate strongly depends on the development of pore pressure in the specimen. The theory of constant rate of strain consolidation or CRS was developed for the first time by Hamilton and Crawford [1] to overcome the constrains of ordinary consolidation test. They conducted several experiments using by strain rates of 0.015%/min to 0.005% /min and despite of such slow rates, were able to record noticeable pore water pressure development during the test. Theory and practice of CRS consolidation test were further developed, using simplifying assumptions similar to Terzaghi's ordinary consolidation test [2,3]. The most important assumptions were constant value for the ratio of permeability to compressibility and validity of Darcy's Law for water flow through the soil specimens [4]. The seepage flow velocity in porous media according to Non-Darcy flow is given by:

$$V = ki^n \quad (1)$$

where $k$ is hydraulic conductivity, $i$ is hydraulic gradient and $n$ is a constant value which depends on the soil characteristics. When $n$ is equal to 1, the flow regime is considered as Darcian.

Lee et al.(1993) employed theories of moving boundary and large strains and proposed a new method for selection of appropriate rate of strain and for determination of coefficient of consolidation under constant rate of strain [5]. Almeida et al (1996) conducted some laboratory tetsts on Rio De Janeiro Clay and showed that the method proposed based on moving boundary and large strains is not suitable for selection of the strain rate in CRS test [6].

During consolidation process, rate of dissipation of pore water pressure is the most important factor, which itself is a function of flow regime through the soil [7]. Several researchers have proposed the ratio of pore water pressure at the bottom of sample to total pressure ($u/\sigma$, known as pore water pressure ratio) as a criterion for selection of appropriate strain rate. The first criterion was first proposed by smith & Wahls in 1969 when they suggested a 50% as the maximum acceptable value for pore water pressure ratio [2]. Based on the results of experiments conducted by Wissa et al. [3], the maximum acceptable value for pore pressure ratio is 5%. Sallfor [8] recommended a value between 10% to 15% as acceptable pore water pressure ratio, while Gromen et al. [9] suggested values in the range of 30% to 50% . Sheahan and Watters [10] were able to achieve results similar to the ordinary consolidation test using a high pore water pressure ratio of 70%. Experiments conducted by Sheahan and Watters [10] showed a parabolic distribution of the pore water pressure in a CRS test.

Regarding the trend of variation of pore pressure ratio versus total stress, two patterns have been observed. One with a decreasing trend of pore pressure ratio with increasing total stress while in the other it initially decreases to some point, then increases to a peak and decreases again [11,12,13,14]. The wide range of values of strain rate of CRS test recommended by different researchers indicates a serious disagreement among the presented criteria for selection of a suitable strain rate in CRS test. This parameter is highly dependent on compressibility and hydraulic properties (permeability) of the soil specimen which both are considered as two major factors in consolidation process. The pore water flow during CRS consolidation test highly depends on the applied strain rate and may cause change in flow regime from Darcy to Non-Darcy besides its impacts on permeability and drainage rate of the soil [14].

The main objective of the present work is to investigate the effect of strain rates on pore water pressure in CRS consolidation test of clayey soils having different plasticity. Two goals are being investigated, firstly to check the validity of assumed flow regime (Darcy) in the relations referring to CRS consolidation and secondly to find a scientific justification and/or interpretation for the existing differences among the various available criteria.

## 2 MATERIALS AND METHOD

In the present study, several consolidation tests were conducted using two CRS apparatuses. To consider the effect of plasticity on consolidation behavior in CRS tests, four different clay samples of low to high plasticity from Karaj and Moghan provinces of Iran and Goteborg area in Sweden were employed.

The clay samples from Iran were prepared using slurry method. In this method, natural air dried soil samples from Moghan and Karaj were sieved through an appropriate sieve size. Then the soil powder was mixed with 200% water content in a mould of 400 mm internal diameter and 800 mm height. The prepared slurry was stirred for 24 hours and let to settle for 48 hours. After settling of the slurry, some excess water at the top of the slurry was drained and it was thoroughly mixed again for 30 minutes. The prepared slurry was used to fill a cylindrical chamber with inner diameter and height of 650 mm and 300 mm, respectively. A filter paper and geotextile sheet were placed at the bottom of the chamber to facilitate drainage of water. The Slurry was left to self-weight consolidation for 2 weeks, during which it was able to be drained from both top and bottom faces. Water level at the top of the chamber was regulated by a drainage tap. To increase the rate of consolidation, a 20 kg stainless steel rigid plate was placed on the top of the slurry and left for one week and the settlement was recorded to confirm completion of consolidation. At the end of preparation period, thickness of the sample was reduced to 72 mm. Figure 1 shows steps of preparation of the initial sample. Finally the test specimens were retrieved by silicon oil coated cutter ring which was fitted into the retaining ring of CRS apparatus. Then, the specimens were trimmed at the top and bottom faces. The consolidation chamber was submerged at all times. Before starting the tests, saturation of the specimens were checked by Skempton's B value. The average value of B parameter for all specimens were about 0.97, hence, they were considered as being saturated.

The samples from Sweden were taken by thin wall Shelby tube under groundwater table and thus were assumed to be undisturbed and fully saturated. To prevent any change in the moisture content of the samples, they were kept in closed tube container in a moist room at a temperature of 7 degrees Celsius. Table 1 shows the physical properties of the clay samples under investigation. Figures 2 and 3 depict the schematic diagrams of the two CRS consolidation apparatuses employed for tests in Iran and Sweden, respectively. The testing methods employed in the two apparatuses were nearly the same. In both apparatuses, the soil sample is allowed to drain at the top end and the valves at the bottom end were closed during the test. Since back pressure was not required, the cell was not filled with any fluid. The pore water pressure at the bottom end was measured using an accurate, calibrated diaphragm type pressure transducer with an accuracy of 0.02% F.S. (The most accurate device available in the Iranian market).

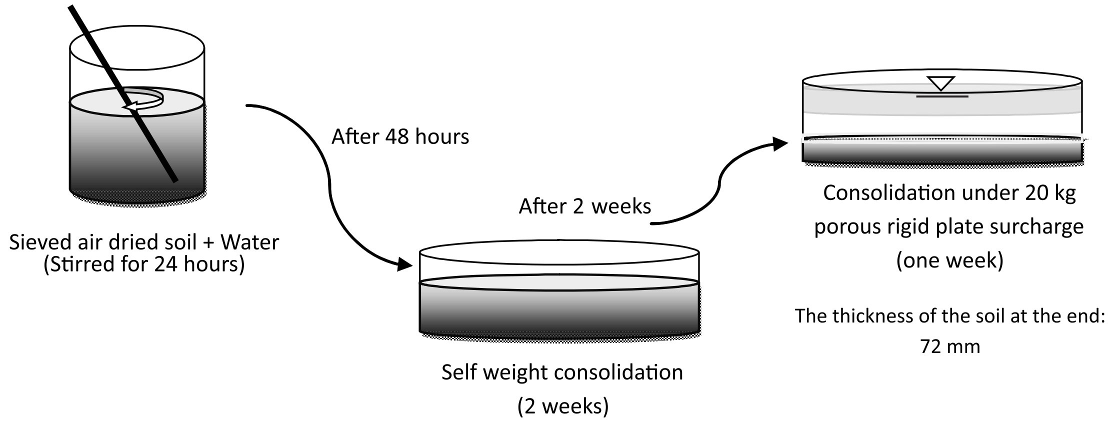

**Figure 1**. Steps of preparing reconstituted sample using slurry method.

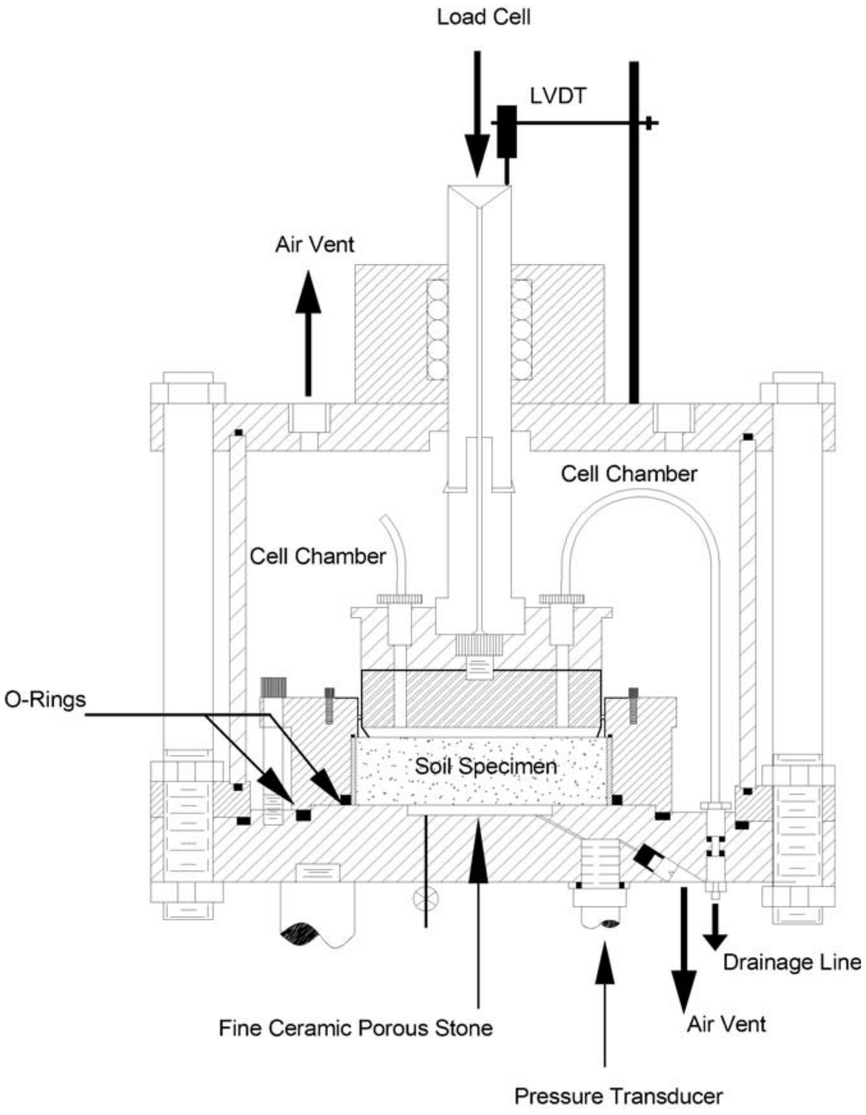

**Figure 2**. Schematic diagram of CRS apparatus employed in Iran.

**Table 1**. Physical properties of samples.

| Sample | Sampling location | Gs | Sand (%) | Silt (%) | Clay (%) | LL (%) | PL (%) | PI (%) | USCS Class | Diameter (mm) | Height (mm) |
|---|---|---|---|---|---|---|---|---|---|---|---|
| A | Moghan | 2.67 | 6 | 54 | 30 | 35.5 | 16.5 | 19.0 | CL | 100 | 20 |
| B | Karaj | 2.71 | 4 | 59 | 37 | 41.5 | 19 | 22.5 | CL | 100 | 20 |
| C | Goteborg | 2.64 | 0 | 7 | 93 | 75 | 15 | 60.0 | CH | 50 | 20 |
| D | Goteborg | 2.68 | 0 | 5 | 95 | 82 | 16 | 66.0 | CH | 50 | 20 |

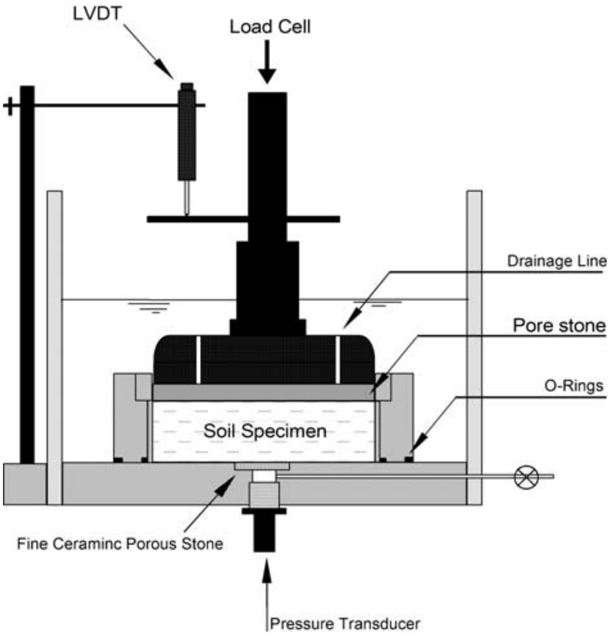

**Figure 3**. Schematic diagram of CRS apparatus employed in Sweden.

**Table 2**. Specifications of the samples and strain rates of different CRS tests.

| Sample | Strain Rate %/min | Initial Water Content (%) | $e_0$ | Maximum Pore Pressure (kPa) |
|---|---|---|---|---|
| A1 | 0.025 | 74.20 | 1.78 | 7.24 |
| A2 | 0.050 | 70.02 | 1.80 | 94.00 |
| A3 | 0.250 | 68.10 | 1.76 | 245.00 |
| A4 | 0.375 | 68.10 | 1.77 | 446.00 |
| B1 | 0.025 | 67.40 | 1.83 | 9.40 |
| B2 | 0.050 | 66.20 | 1.81 | 132.60 |
| B3 | 0.250 | 70.10 | 1.87 | 253.00 |
| B4 | 0.375 | 68.40 | 1.80 | 432.00 |
| C1 | 0.001 | 89.00 | 2.40 | 2.00 |
| C2 | 0.006 | 88.00 | 2.40 | 14.00 |
| C3 | 0.012 | 89.00 | 2.40 | 22.00 |
| C4 | 0.024 | 84.00 | 2.50 | 50.60 |
| D1 | 0.001 | 33.00 | 0.9 | 1.70 |
| D2 | 0.006 | 35.50 | 0.95 | 9.60 |
| D3 | 0.012 | 33.00 | 0.93 | 22.00 |
| D4 | 0.024 | 33.00 | 0.92 | 35.50 |

Vertical deformations and applied stresses were measured using LVDT and load cell, respectively and recorded via a data logger. Constant strain rate was applied to the soil samples through a precision pressure controller. The tests were carried out in accordance with ASTM D4186-2000 [4]. Due to full saturation of the samples backpressure was not applied to the specimens [10,5].

To investigate the effect of different testing speeds, the samples from Iran (having higher permeability) were tested at higher speeds and samples from Sweden (having lower permeability), were tested at lower speeds. For this purpose, four strain rates of 0.001%/min, 0.006%/min, 0.012%/min and 0.024%/min were applied to samples from Sweden and strain rates of 0.025%/min, 0.050%/min, 0.250%/min and 0.375%/min were applied to samples from Iran. Table 2 shows the applied strain rates for different samples.

## 3 RESULTS

### 3.1 VARIATION OF PORE WATER PRESSURE

Variation of the pore water pressure at the bottom end of the samples with time indicates that the pore pressure increases gradually and reaches to a maximum value at the end of the test. Figures 4 to 7 present the results of the tests conducted on different samples. As these figures show, magnitudes of the pore water pressure at the bottom of the samples depend on the strain rate. As the strain rate increases, the pore pressure increases accordingly. This is due to lesser available time for dissipation of the developed pore water pressure. While, for the same samples tested under lower strain rates, there is enough time for dissipation of pressure, and thus, lower magnitudes of pore water pressure were recorded. The maximum pore water pressure developed in each test is given in Table 2.

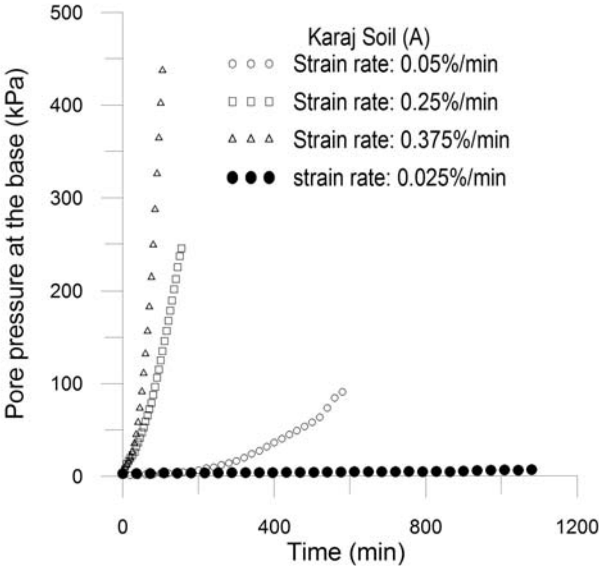

**Figure 4**. Variation of pore pressure with time for sample A (PI=22.5%).

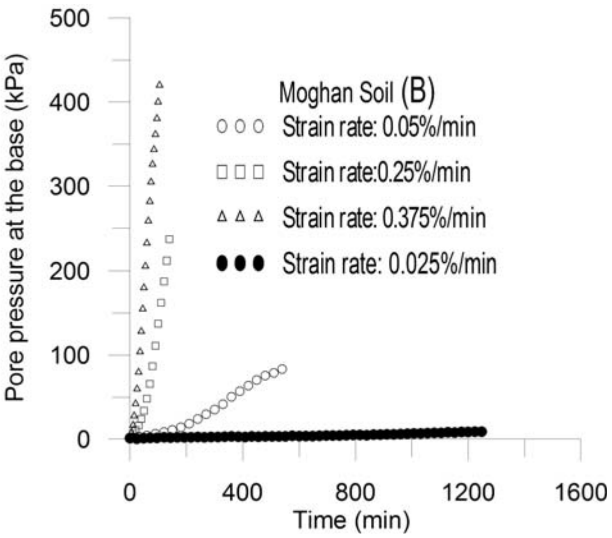

**Figure 5**. Variation of pore pressure with time for sample B (PI=19%).

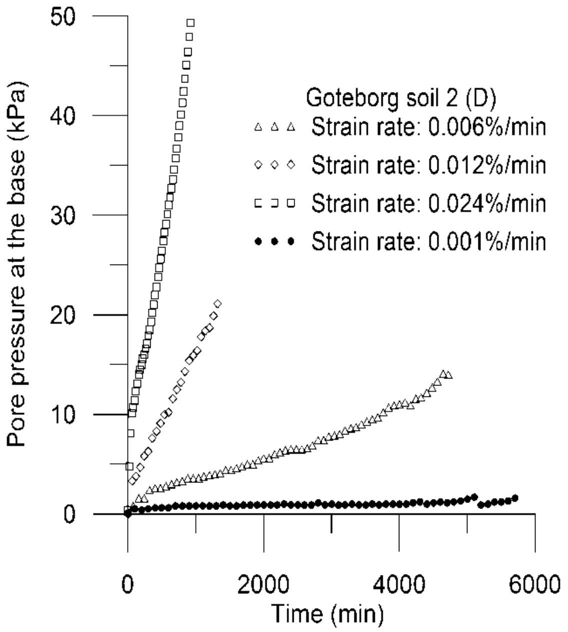

**Figure 6**. Variation of pore pressure with time for sample C (PI=60%).

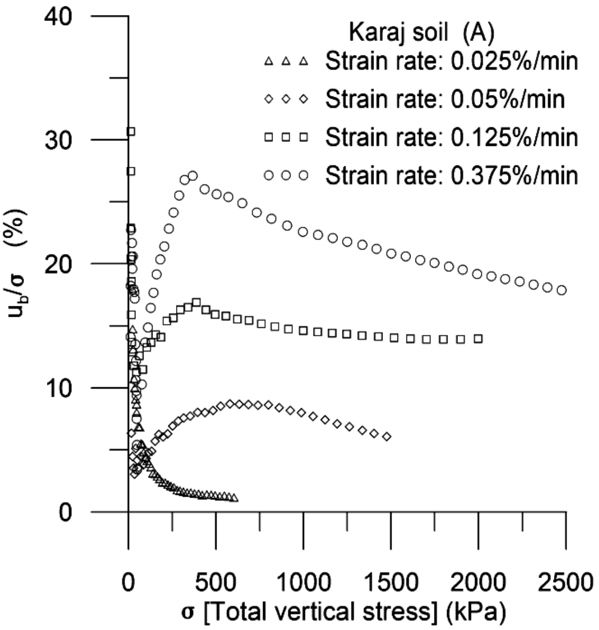

**Figure 7**. Variation of pore pressure with time for sample D (PI=66%).

## 3.2 RELATIONSHIP BETWEEN TOTAL STRESS AND PORE WATER PRESSURE

The main reason for development and increasing of pore pressure in a CRS consolidation test is the applied total vertical stress which gradually increases during the course of the test (due to very slow process of pore pressure dissipation). To study the trend and pattern of variation of pore pressure in different samples, the ratio of developed pore water pressure at the bottom of sample to the total stress ($u/\sigma$) versus total stress ($\sigma$) has been depicted in Figures 8 to 11. Figures 8 and 9 depict such variations for samples A and B which are less plastic and have been tested at higher strain rates. As these figures show, the curves at the very beginning indicate a sharp drop. The reason for such a drop is the fact that at the very beginning there is some residual pore water pressure due to the weight of the sample itself, while the total stress is still zero and thus, their ratio is a large value. After starting of the test, the total stress increases

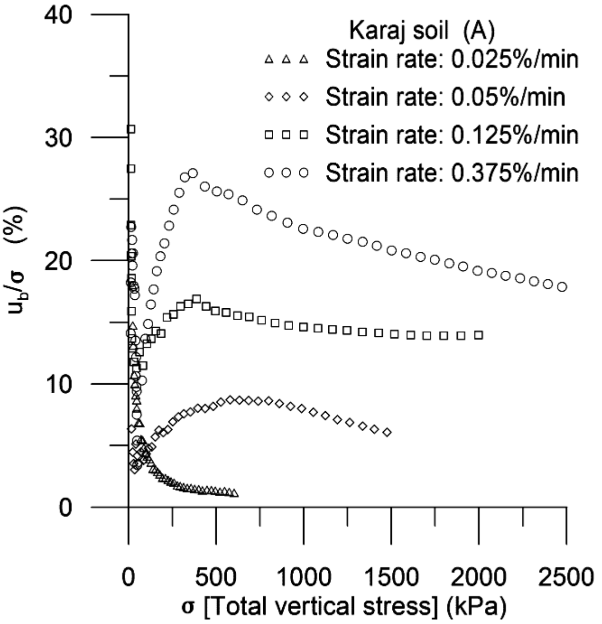

**Figure 8**. Variation of relative pore pressure versus total stress for sample A.

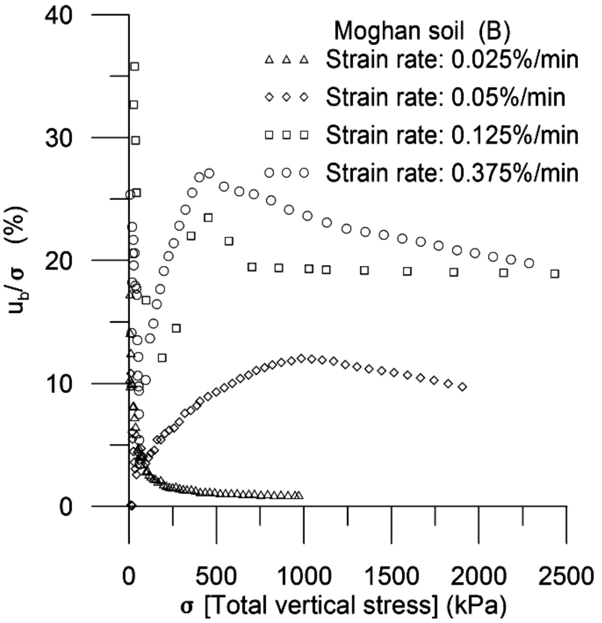

**Figure 9**. Variation of relative pore pressure versus total stress for sample B.

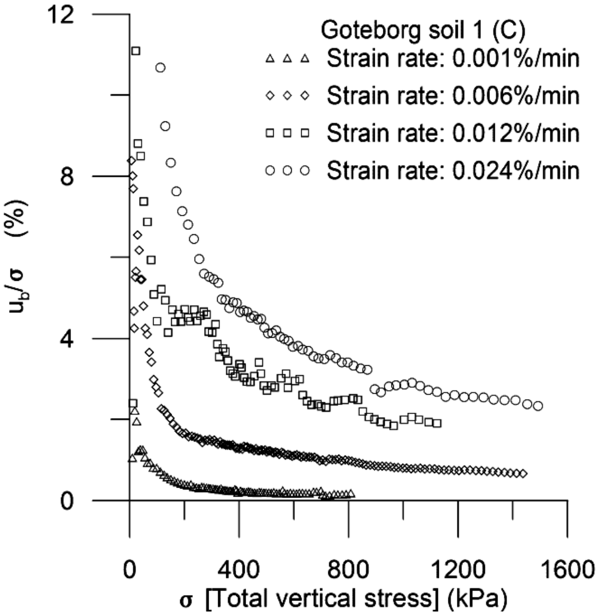

**Figure 10**. Variation of relative pore pressure versus total stress for sample C.

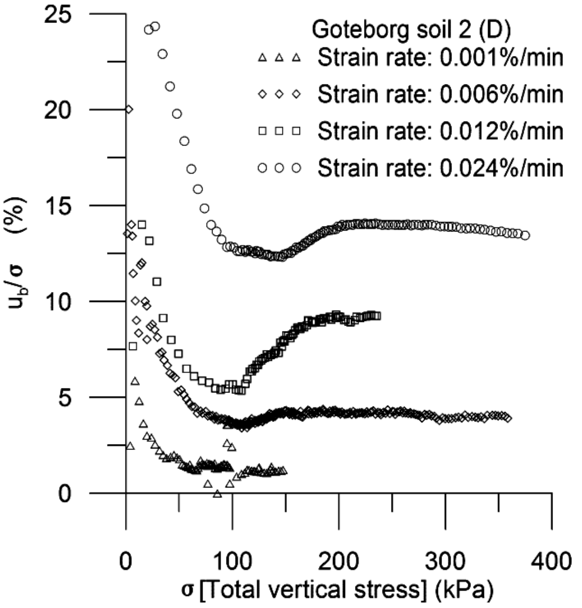

**Figure 11**. Variation of relative pore pressure versus total stress for sample D.

and the pore pressure ratio decreases sharply for a short period of time. For samples A and B, which were tested at higher strain rates, there is not enough time for the built-up pore water pressure to dissipate and thus the curves indicate an increasing trend up to a peak point, beyond which the pore pressure ratio drops gradually due to increase in total stress.

Figures 10 and 11 depict the test results for samples C and D which were of higher plasticity, and tested at lower strain rates. According to these figures, the pore water pressure ratio decreases by increasing total stress. The trend of the curves for all applied strain rates show a steep slope at the beginning, which becomes less towards the end of the test, showing no maximum or minimum value. The reason for such a continuously decreasing trend is lower strain rates which provide the opportunity for the samples to be drained. However, there are some differences between the results of samples D and C, due to their different water content and void ratio. Sample D is more plastic and has less void ratio in comparison with sample C and thus, dissipation of pore pressure is slower for the former. This fact causes an increasing trend in pore water pressure ratio at some stages of the tests.

## 3.3 FLOW REGIME IN CRS CONSOLIDATION TEST

In a CRS consolidation test, by increasing the applied total stress, excess pore water pressure is developed and dissipated gradually as the sample is drained. If similar to a trixial CD test, the load is applied slowly; pore pressure has the opportunity to dissipate in a short period of time and thus, the ratio of pore pressure to total stress would decrease. However, in a CRS test, since increasing rate of the total pressure is not constant and in the mean time the permeability of the soil sample decreases due to its compression, thus, dissipation of the pore pressure is much slower [7]. This would cause an increase in the ratio of pore pressure to total stress. After some times, the rate of increase in this ratio becomes slower which is indicative of an ease in draining of the sample and it means the hydraulic conditions through the specimen changes. Since the resistance against flow is always higher in a non-Darcy flow than a Darcy flow [15], thus, easier dissipation of pore pressure, in spite of lower void ratio and lower permeability, is due to the change in flow regime. This means that during the course of a CRS consolidation test, the flow regime changes from non-Darcy to Darcy. In fact, for those samples, where the trend of variation of pore pressure ratio versus total stress at the beginning is ascending and then descending, the flow regime changes from non-Darcy to Darcy. The peak point on the curve of pore pressure ratio versus total stress shows the moment at which the flow regime changes from Non-Darcy to Darcy.

For better understanding of the flow regime during the tests, variation of hydraulic gradient against velocity is normally plotted. Since in a CRS consolidation test the velocity of outflow is equal to the strain rate, thus, it should always be constant. Due to compression of the sample, its void ratio and consequently permeability is decreasing and thus, it is not possible to plot the variation of hydraulic gradient against velocity for a given permeability, unless to stop the test and measure coefficient of permeability at a given time. In such a case, variation of hydraulic gradient against velocity will be indicated by a horizontal line (dashed line on Figure 12). If the hydraulic gradient and velocity are plotted on horizontal and vertical axes respectively, then every point on the plotted line is indicative of a given permeability. As shown in Figure 12, for any given value of coefficient of permeability, a single curve can be plotted which crosses the dashed horizontal line at the given point (given hydraulic gradient and velocity). As the time passes and consolidation progresses, the curve of hydraulic gradient versus velocity moves towards left. This is similar to the findings of Hansbo [16,17,18] who plotted hydraulic gradient versus velocity in an ordinary consolidation test, by measuring coefficient of permeability of the sample at each loading stage.

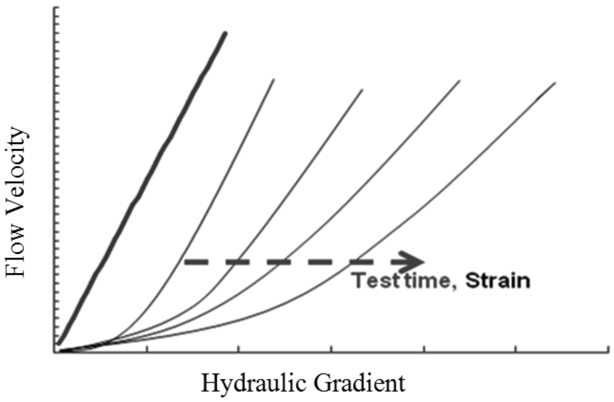

**Figure 12**. Variation of hydraulic gradient versus velocity in a CRS test.

In a CRS consolidation test, the thickness of the sample and pore pressure at both ends at any time are known and thus, the mean hydraulic gradient at any time can be determined by dividing the difference between pore pressures at the top and bottom faces of the sample to its height. The exit velocity of water in CRS test is equal to speed of the compressing piston or compression [13]. Therefore, considering the four applied strain rates, for each given void ratio one point is found. Thus, in total four points related to four strain rates are found which are used to plot the trend curve.

In the present study, variation of hydraulic gradient (*i*) versus flow velocity (*v*) has been plotted by conducting the CRS consolidation tests at different strain rates for samples C and D. The linearity or non-linearity of the plotted curves is indicative of flow regime. A linear relationship is indicative of Darcy flow and non-linear depicts a non-Darcy flow. Figures 13 and 14 show the curves obtained in CRS tests conducted on soil samples from Sweden. As these figures show, the relationship between i and v is non-linear, which is indicative of a non-Darcy flow. The same behavior was observed for two other soil samples as well.

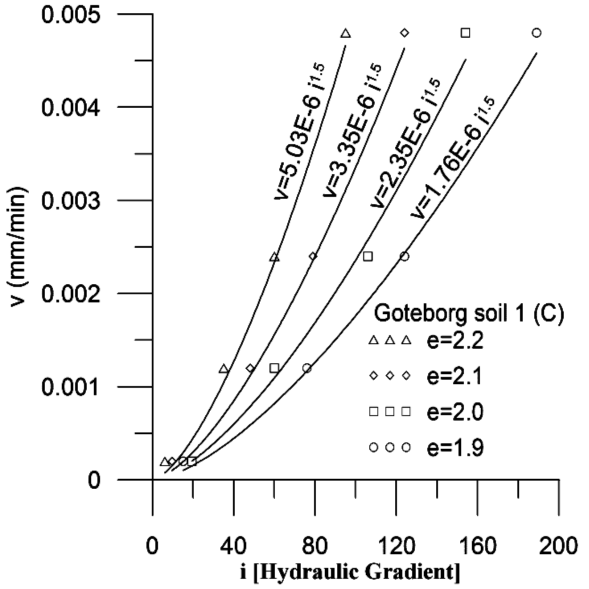

**Figure 13**. Variations of hydraulic gradient versus flow velocity for sample C.

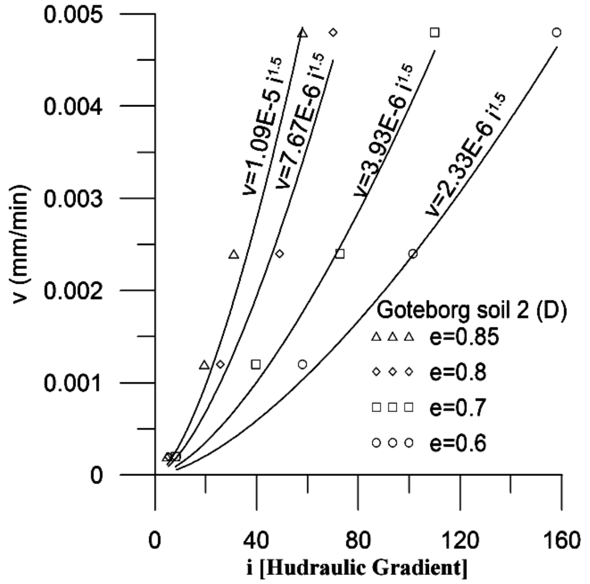

**Figure 14**. Variations of hydraulic gradient versus flow velocity for sample D.

These curves are related to the middle time period of the tests. An exponential curve with exponent of 1.5 has shown a good correlation with obtained data, though other types of curves may also be satisfactory. However, in general, the trend s of the curves show that relationship is not linear and the flow is considered as non-Darcy.

In a CRS consolidation test, the flow regime may be Darcy, non-Darcy or both, depending on the strain rate which is equal to the velocity of the drained water flow. The non-Darcy flow during a consolidation test occurs due to continuous blockage of flow channels or changes in the direction of flow [19]. All relationships obtained for CRS consolidation in the past, were developed by assuming a Darcy flow for the whole duration of the test. While, the results of the present study show that the flow regime in a CRS test could be non-Darcy, and thus, it is necessary to develop the relevant relationships. In other words, to obtain more accurate results in a CRS test, the consolidation parameters should be determined using the appropriate relationships relevant to the expected flow regime. To develop such a proper consolidation equation, the non-Darcy flow regime (Eq. 1, $n \neq 1$) should be considered in Darcy's Equation to develop the required realtionships. The development of such equation is out of the scope of this paper.

## 3.4 STRESS-STRAIN BEHAVIOR

In a CRS consolidation test the normal stress in compression curve is often presented by effective stress. Based on parabolic distribution of pore water pressure in sample during CRS consolidation, the mean effective stress is determined as follows [3]:

$$\bar{\sigma}' = \sigma - \frac{2}{3}u_b \quad (2)$$

During consolidation, the pore water pressure distribution in the sample is also parabolic, when non-Darcy flow rule is applied [20]. Therefore, to determine the effective stress, equation 2 is employed. The compression curves for tested samples are presented in Figures 15 to 18.

Figures 15 and 16 show the compression behavior of the two samples having lower plasticity. These curves resemble similarity to the behavior of remolded samples, though the samples were reconstituted. This behavior is due to high water content and high softness of the samples. These figures also show a shift to the right of compression curves for the three rapid tests in comparison with slower tests. This is more evident in Moghan sample. The compression curves for all rapid tests show almost the same trend (Figures 17 and 18). It means that during primary consolidation, creep has not occurred, which is in agreement with findings of Leroueil [21].

In samples with high plasticity, similar behavior has been observed and the compression curves for rapid tests were shifted to the right in comparison with the slow tests. This is more evident in sample D. Thus it can be concluded that in these samples also creep was negligible. The virgin curves of these samples have steep slope which is indicative of their higher sensitivity [22]. However, the compression behavior of all samples is similar and effect of strain rate on pore water pressure is considerable.

As it was shown in the previous section, the trend of curves of pore pressure ratio versus total stress in sample C differs from other samples, while there was no differ-

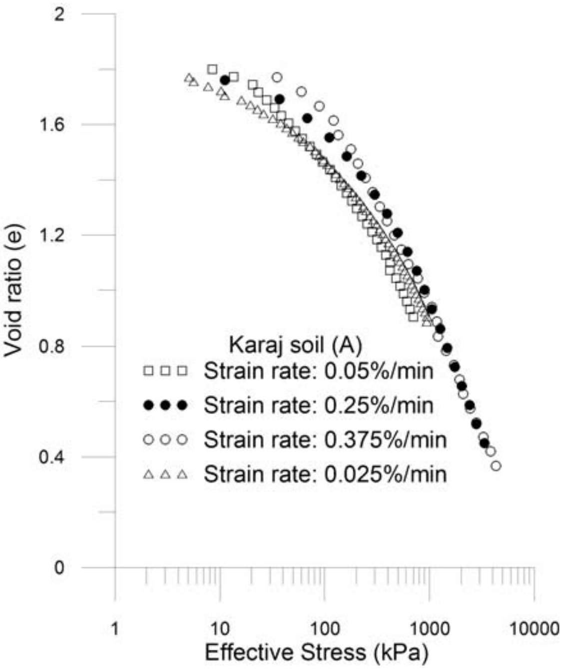

**Figure 15**. Compression curve for different rate of strains, Sample A (PI=22.5).

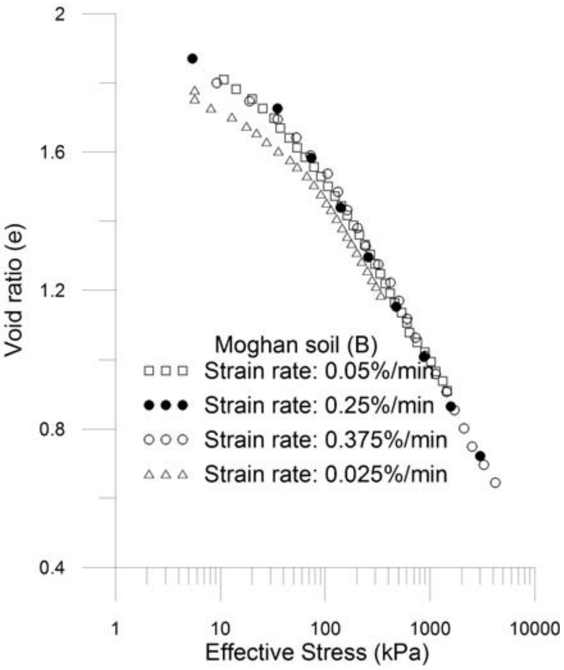

**Figure 16**. Compression curve for different rate of strains, Sample B (PI=19).

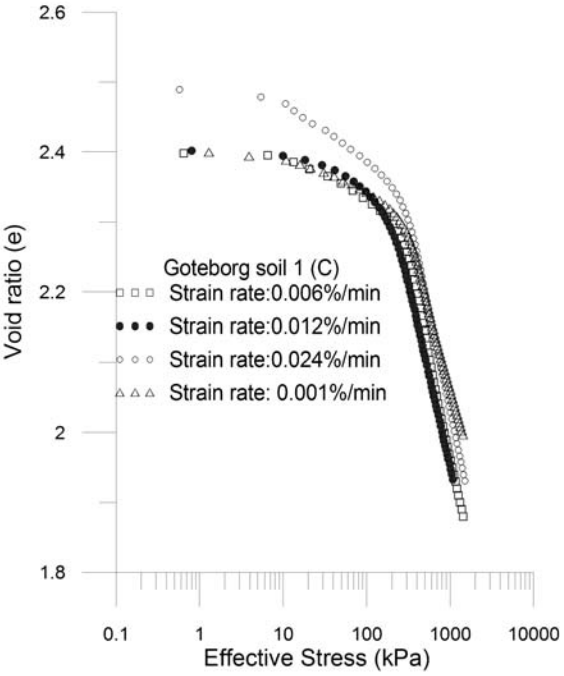

**Figure 17**. Compression curve for different rate of strains, Sample C (PI=60).

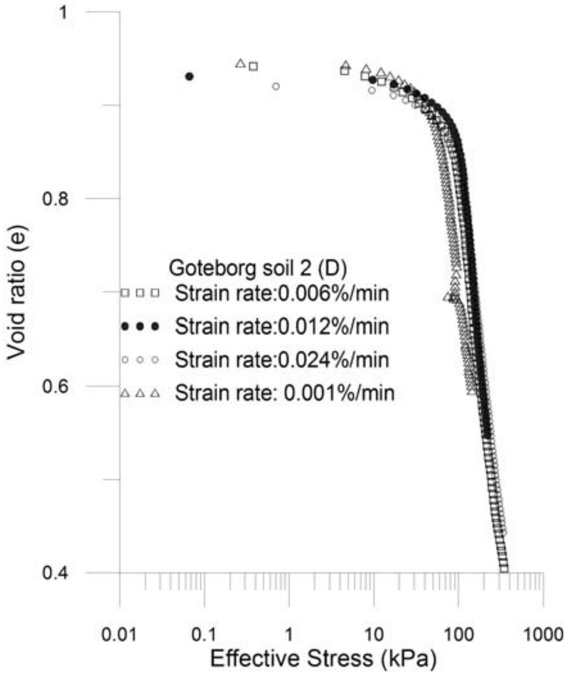

**Figure 18**. Compression curve for different rate of strains, Sample D (PI=66).

ence among the compression curves. It is believed that the different impact of strain rate on variation of relative pore pressure versus total stress is not related to the stiffness of the samples, rather it is due to flow regime during consolidation process.

## 4 CONCLUSIONS

Based on the results of the present study, the following conclusions are made:

- The pore pressure induced at the bottom of the sample in a CRS consolidation test is variable and depends on the strain rate. The higher soil plasticity, the higher is the induced pore pressure.
- For both low and high plastic samples, the relation between pore water pressure and time for a given strain rate is almost linear; however, at the beginning of the tests some nonlinearity was observed.
- Variation of pore pressure ratio ($u_b/\sigma$) against total stress ($\sigma$) in CRS test is related to the strain rate. In smaller strain rates, the pore pressure has the opportunity to be dissipated easily, and thus no excess pore pressure is developed. While for higher strain rates, the induced pore water pressure does not have enough time to be dissipated and thus, excess pressure is developed in early stages of the test, but will gradually decrease during final stages due to change in the flow regime.
- Variation of pore pressure ratio is related to the flow regime. The increasing trend is indicative of non--Darcy flow, while the decreasing trend is indicative of Darcy flow. The point of maximum on the curve of pore pressure ratio versus total stress shows the moment at which the flow regime changes from Non-Darcy to Darcy.
- Plotting hydraulic gradient against flow velocity in the CRS tests conducted in the present study, has very well demonstrated that the flow regime is mostly non-Darcy. This is an important fact which should be considered in analysis of the results of CRS consolidation tests.
- In both low and high plasticity samples, the pore pressure behavior was almost the same. However, due to lower permeability of the high plasticity samples, the impact of strain rate is comparatively more evident and considerable variation were observed in the drainage behavior at lower strain rates.
- As shown, validation of Darcian flow through specimens under CRS consolidation test is in question and developing new equations based on more realistic Non-Darcian flow is essential.

## REFERENCES

[1] Hamilton, J.J., Crawford, C.B. (1959). Improved determination of preconsolidation pressure of a sensitive clay. Papers on Soils, ASTM Spec. Tech. Pub. 1, 254-270.

[2] Smith, R. E., Wahls, H. E. (1969). Consolidation under constant rate of strain., Journal of Soil Mech. Found. Div. 95 (SM 2).

[3] Wissa, A. E. Z., Christian, J. T., Davis, E. H., Heiberg, S. (1971). Consolidation testing at constant rate of strain. Journal of Soil Mechanic and Foundation Div., ASCE 97 (10), 1393-1413.

[4] ASTM, (2002). Annual Book of ASTM Standards. American Society for Testing and Materials, Soil and Rock, D4186-89, 500-505.

[5] Lee, K., Choa, V., Lee, S. H., Quek, S. H. (1993). Constant rate of strain consolidation of Singapore Marine Clay. Geotechnique 43 (3), 471-488.

[6] Almeida, M. S. S., Martins, I. S., Carvalho S. R. L. (1995). Constant rate of strain consolidation of Singapore Marine Clay, Discussion to paper (Lee, K. et. al.). Geotechnique 45 (2), 333-336.

[7] Dobak, P. (2003). Loading velocity in consolidation analysis. Geological Quarterly 47 (1), 13-20.

[8] Sallfor, G. (1975). Perconsolidation pressure of soft highly plastic clays. Chalmers Univ. Tech. Goteborg.

[9] Gorman, C. T., Hopkins, T. C., Deen, R. C., Drenvich, V. P. (1978). Constant rate of strain and controlled gradient consolidation testing. Geotech. Testing Journal1(1), 3-15.

[10] Sheahan, T. C., Watters, P. J. (1997). Experimental verification of CRS consolidation theory. Journal of Geotechnical and Geoenvironmental Eng. 123, 5, 430-437.

[11] Armour, D. W. Jr., Dernevich, V. P. (1986). Improved techniques for the constant rate of strain consolidation test, Consolidation of Soils: Testing and Evaluation, ASTM STP 892, R. N. Yong and F. C.

[12] Seah, H. T., Juirnarongrit, T. (2003). Constant rate of strain consolidation with radial drainage. Geotechnical Testing Journal 26,4, 1-12.

[13] Yune, Y. C., Chung, K. C. (2005). Consolidation test at constant rate of strain for radial drainage. Geotechnical Testing Journal 28, 1, 71-78.

[14] Ahmadi.H, Rahimi. H., Soroush. A. (2011) Investigation on the Characteristics of pore water flow during CRS consolidation test. Geotechnical and Geological Engineering 29, 6, 989-997.

[15] Mitchell, K. J, Younger, J. S. (1967). Abnormalities in hydraulic flow through fine-grained soils. In Idriss, I., M. (Ed) (2001). Selected geotechnical papers of James K. Mitchell, ASCE, 142-178.

[16] Hansbo, S. (1960). Consolidation of clay, with special reference to influence of vertical sand drains. A study made in connection with full scale investigations at Skä-Edeby. Doctoral thesis, Swedish Geotechnical Institute.

[17] Hansbo, S. (2001). Consolidation equation valid for both Darcian and non-Darcian flow. Geotechnique 51, 1, 51-54.

[18] Hansbo, S. (2003). Deviation from Darcy's Law observed in one-dimensional consolidation. Geotechnique 53, 3, 601-605.

[19] Mitchell, K. J., Soga, K. (2005). Fundamental of Soil Behaviors. Third Edition, John Wiley and Sons, New York, N.Y.

[20] Ing, C. T., Xiaoya, N. (2002). Coupled consolidation with non-Darcian flow. Computers and Geotechnics 29, 169-209.

[21] Leroueil, S. (1988). Recent developments in consolidation of natural clays. Tenth Canadian Geotechnical Colloquium. Canadian Geotechnical Journal 25, 85-107.

[22] Bowles, E. J. (1979). Physical and Geotechnical Properties of Soils. McGraw-Hill Book Company, New York, NY.

# OCENITEV UČINKOV NOTRANJE EROZIJE V ZEMELJSKIH JEZOVIH IN NASIPIH Z UPORABO SPLOŠNIH NEVRONSKIH MREŽ

XINHUA XUE, XINGGUO YANG in XIN CHEN

## o avtorjih

Xinhua Xue
Sichuan University,
State Key Laboratory of Hydraulics and Mountain River Engineering,
College of Water Resource and Hydropower
No.24 South Section 1, Yihuan Road, Chengdu, Sichuan, 610065, Kitajska
E-pošta: scuxxh@163.com

Xingguo Yang
Sichuan University,
State Key Laboratory of Hydraulics and Mountain River Engineering,
College of Water Resource and Hydropower
No.24 South Section 1, Yihuan Road, Chengdu, Sichuan, 610065, Kitajska
E-pošta: 89022251@163.com

Xin Chen
Sichuan University,
State Key Laboratory of Hydraulics and Mountain River Engineering,
College of Water Resource and Hydropower
No.24 South Section 1, Yihuan Road, Chengdu, Sichuan, 610065, Kitajska
E-pošta: chenxin_scu@163.com

## izvleček

*Notranja erozija, ki vodi do izpiranja materiala in nastanka zveznih kanalov, je glavni vzrok za napake in nesreče pri zemeljskih jezovih. Za oceno tveganja ob pojavu takih napak je nujno razumeti delovanje in učinke notranje erozije in razviti znanstveno izpeljane analitične modele, ki so enostavnejši, lažji za izvedbo in bolj natančni od tradicionalnih metod. V študiji je bila za oceno nevarnosti notranje erozije uporabljena tehnika splošne regresijske nevronske mreže (GRNN) zaradi njene sposobnosti prilagajanja kompleksnim nelinearnim modelom. Delovanje splošne regresijske nevronske mreže je bilo preverjeno z uporabo metode k-kratnega navzkrižnega preverjanja. Izkazalo se je, da ima GRNN model zelo dobre sposobnosti predvidevanja, zato je pričakovati, da bo zelo zanesljiv za ocenjevanje nevarnosti notranje erozije.*

## ključne besede

notranja erozija, splošna nevronska mreža, navzkrižno preverjanje, BP nevronska mreža

# ESTIMATING PIPING POTENTIAL IN EARTH DAMS AND LEVEES USING GENERALIZED NEURAL NETWORKS

XINHUA XUE, XINGGUO YANG and XIN CHEN

**about the authors**

Xinhua Xue
Sichuan University,
State Key Laboratory of Hydraulics and Mountain River Eng.,
College of Water Resource and Hydropower
No.24 South Section 1, Yihuan Road, Chengdu, Sichuan
610065, P.R.China
E-mail: scuxxh@163.com

Xingguo Yang
Sichuan University,
State Key Laboratory of Hydraulics and Mountain River Eng.,
College of Water Resource and Hydropower
No.24 South Section 1, Yihuan Road, Chengdu, Sichuan
610065, P.R.China
E-mail: 89022251@163.com

Xin Chen
Sichuan University,
State Key Laboratory of Hydraulics and Mountain River Eng.,
College of Water Resource and Hydropower
No.24 South Section 1, Yihuan Road, Chengdu, Sichuan
610065, P.R.China
E-mail: chenxin_scu@163.com

## Abstract

*Internal erosion and piping in embankments and their foundations is the main cause of failures and accidents to embankment dams. To estimate the risks of dam failure phenomenon, it is necessary to understand this phenomenon and to develop scientifically derived analytical models that are simpler, easier to implement, and more accurate than traditional methods for evaluation of piping potential. In this study, a generalized regression neural network (GRNN) technique has been applied for the assessment of piping potential, as well, due to its ability to fit complex nonlinear models. The performance of GRNN has been cross validated using the k-fold cross validation method technique. The GRNN model is found to have very good predictive ability and is expected to be very reliable for evaluation of piping potential.*

**Keywords**

piping, generalized neural network, cross validation, BP neural network

## INTRODUCTION

In recent years, dam safety has drawn increasing attention from the public. This is because floods resulting from the breaching of dams can lead to devastating disasters with tremendous loss of life and property, especially in densely populated areas [1]. Past dam-failure disasters showed that the loss of life is directly related to the evacuation time available, should failures occur. It is therefore very important to understand the process of dam breaching, and if possible, to obtain the key breaching parameters required to quantitatively describe the dam-breaching process.

Earth and rockfill dams are widely used throughout the world, and most past dam failures involved such dams. Piping is the most common cause of dam failures. According to statistics, approximately half of all the world's dam failures are attributed to piping phenomena [2-3]. Possible piping-phenomena modes include heave, internal erosion and backwards erosion. While the most common piping-failure mode is internal erosion, most often associated with conduits or other structural penetrations through dams, up to one-third of all piping failures can be attributed to backwards-erosion piping [4].

Piping phenomena have been studied by a large number of researchers and the list of publications on this topic is voluminous. For instance, in the early twentieth century, Terzaghi [5] performed experiments on heave-type piping, and developed a theoretical framework for the prediction of heave. Based on this framework, an equation for the factor of safety against heave was later adopted by practitioners for all piping-failure modes, such as backward-erosion piping and piping along internal fractures (concentrated leak erosion), although the theoretical basis for this adaptation of Terzaghi's equations has not been confirmed with laboratory experiments. Bligh [6] and later Lane [7] recognized a fundamental difference in the piping mechanisms between the seepage occurring through intergranular flow and the seepage along soil/structure boundaries. Modern practitioners define these piping mechanisms as backwards-erosion piping (for the intergranular-flow case), and concentrated leak erosion for the case of flow along pre-existing openings (either soil-structure openings or cracks through an embankment), and so on. However, more research is still needed to fill in the gaps in our understanding of piping. Many existing structures were constructed without filters or with inadequate filters. Current methods for the evaluation of piping potential are based on theories that were developed almost 100 years ago, which have proven to be inadequate, when one considers the range of mechanisms that fall under the heading "piping"[8]. Therefore, many scholars and experts have attempted to develop scientifically derived analytical models that are simpler, easier to implement, and more accurate than traditional methods for the evaluation of piping potential.

In recent years, due to pervasive developments in computational software and hardware, several alternative computer-aided pattern-recognition approaches have emerged [9]. An artificial neural network (ANN) is a sophisticated computational approach capable of modelling a highly complex function [10]. It is frequently employed to mimic a nonlinear function with a large number of variables that cannot be modelled with a classical linear function. The theory, design and application of ANNs have been advancing a great deal during the past 20 years in order to solve complicated problems in different fields, including structural and earthquake engineering [11-12], construction engineering [13], geotechnical engineering [14], signal processing [15] and geosciences [16]. The neural network is well known as a parallel information-processing structure that consists of simple processing units with a high degree of interconnection between each unit. Each neuron performs a relatively simple job: receive impulses from input cells or neurons, carry out some types of transformation of the inputs and pass on the weighted products to the other cells or other neurons. The function of a neural network replicates that of a biological brain, which is basically composed of a very large number of massively interconnected neurons. Neural networks exhibit a mapping capability, learn from examples and possess the capability to generalize. They are robust systems that attempt to mimic the fault-tolerance and can process information in parallel with high speed. For these outstanding capabilities, neural networks are designed for pattern-recognition and classification applications.

There are different types of neural networks that can be employed for pattern recognition, e.g., generalized neural network (GRNNs), multi-layer perceptron and recurrent network, and so on. In this study, a GRNN has been chosen to predict the occurrence of a seepage piping disaster in terms of selected factors. The performance of the GRNN was cross-validated using the *k*-fold cross-validation technique. The main purpose of this paper is to determine the scope and suitability of the GRNN for the prediction of piping disasters in embankments.

## 2 MECHANISM OF PIPING

Piping is a process whereby internal voids are created by seepage flow. Erosion in earth structures due to water flow occurs when the erosion-resistant forces are less than the seepage forces that tend to produce it, in such a way that the soil particles are removed and carried with the water flow (Fig.1).

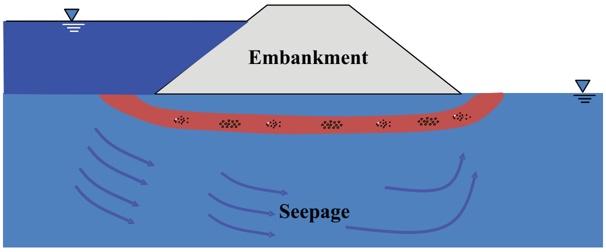

**Figure 1**. Illustration of piping leakage.

The resistant forces depend on the cohesion, the interlocking effect, the weight of the soil particles and the kind of protection they have downstream, if any. Since the seepage through an earth structure is not uniform, the erosion phenomenon increases where there is a concentration of seepage and water velocity; in places where this concentration emerges at the downstream side, the erosive forces on the soil particles might become very significant. This accentuates the subsequent concentration of seepage and erosive forces there. The seepage water has a velocity and force such that it is able to remove soil particles from the ground surface at the point of exit. As the soil particles are removed, the length of the seepage path decreases, resulting in a higher hydraulic gradient. The increased hydraulic gradient induces a higher seepage velocity and force, which in turn moves ever larger soil particles (Fig.2).

Piping in earth dams can be categorized based on the erosion process, i.e., concentrated leak erosion, backward erosion, suffusion and soil contact erosion [17]. This is shown in Fig.3 (a) and (b) for piping through the foundation, and from the embankment to the foundation. Concentrated leak erosion is defined as the erosion of soil in a crack or a system of interconnecting voids in an earth dam or its foundation [17]. The initial cracks generated by differential settlement, desiccation or

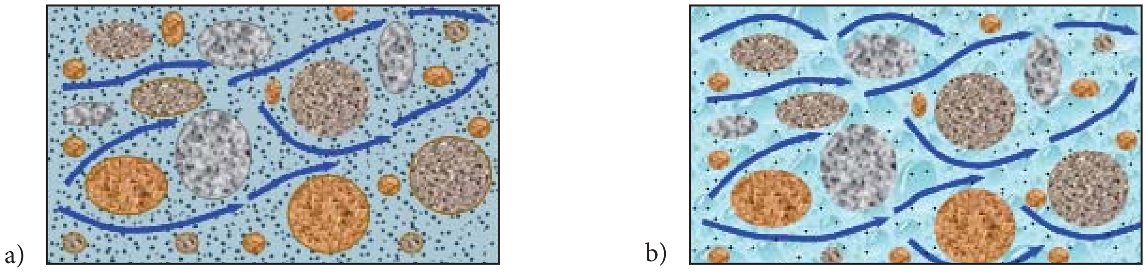

**Figure 2**. Illustration of sand content and seepage flow during piping leakage. a) Before piping. b) After piping.

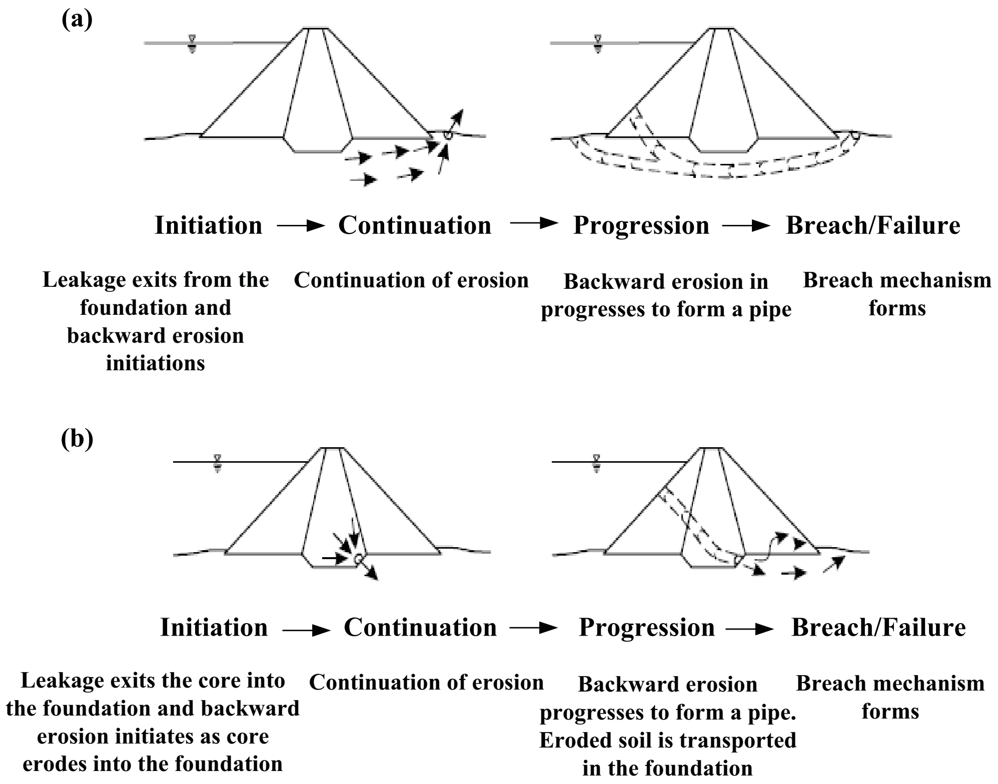

**Figure 3**. Models for the development of failure by piping in the foundation and from the embankment to the foundation [18]. a) Piping in the foundation initiated by backwards erosion. b) Piping from the embankment to foundation initiated by backwards erosion.

freezing may be shut by the swelling or softening of the soil, but remain to be a serious problem for dams with unfavourable internal stress conditions.

The above process can be described briefly as follows [19]:

1) Initiation. Cracks or defects providing potential seepage paths in the dam or foundation may result from a number of causes: differential settlement, desiccation, backward erosion, earthquake shaking, high-permeability zones due to poor compaction or segregation of the fill during placement, suffusion (internal instability) of gap graded soils, or hydraulic fracture. Erosion begins when the hydraulic gradient in the seepage path becomes large enough to move the soil particles. Thus, the requirements for this phase are: 1) a path for concentrated flow (usually a crack of some kind) and 2) the initiation of erosion along the seepage path.

2) Continuation. The requirements for the continuation of erosion are the lack of an effective filter and the ability for the eroding particles to be removed at the downstream end of the seepage path. While a designed filter is obviously the most reliable means for stopping the removal of particles along a seepage pathway, other fill zones and native soil deposits may also provide restraint, even if they do not meet modern filter-design criteria. In such cases, some erosion of the base soil may take place before the filtering material becomes effective.

3) Progression. In the progression phase the seepage pathway enlarges to form a pipe or open eroded conduit through the embankment. This requires sufficient flow through the leak to maintain the eroding velocities, and the ability of the surrounding soil to support a pipe without collapse, as illustrated in Fig.3. The flow-limiting ability of the upstream and downstream zones can control the flow volume through the leak. In addition, crack fillers can migrate from upstream zones into defects within the seepage barriers and seal off concentrated leaks.

   Soils with the ability form and hold an arch (soils with plastic fines and cemented granular soils are likely to have the highest arching ability) are capable of supporting a pipe [20, 21]. It is also possible for a pipe to be supported by bedrock or competent soil above the eroding soil.

4) Breach. Breach mechanisms may include the gross enlargement of the pipe, crest settlement, unravelling of the downstream slope, and slope instability leading to an open flow channel through the embankment.

From the above it can be seen that the extent and severity of the piping is dependent on the embankment-soil type. A soil that allows bridging, or a "roof" to form over the void, will allow piping to develop to a large extent and remain unnoticed from above. Piping often causes sinkholes to form at isolated points along its path through the embankment. If the soil mass over the pipe is unable to bridge, or the pipe enlarges to such an extent that the overlying soil mass collapses, a sinkhole will be created. Seepage may exit the downstream face of an embankment or its foundation at any point. Therefore, piping may develop on the embankment slope, along the toe of the foundation or at some distance beyond the toe. Generally, underseepage that exits closer to the toe of the embankment is potentially more critical than seepage that initially exits at some distance away.

## 3 ARTIFICIAL NEURAL NETWORKS (ANNS) OVERVIEW

Artificial neural networks (ANNs) is a computational approach inspired by the human nervous system [22, 23]. Its data-processing paradigm is made up of highly interconnected nodes (neurons) that map a complex input pattern with a corresponding output pattern. They are known for their generalization ability and ease of working with highly dimensional and nonlinear data.

There are many types of neural network structures (architectures) and training algorithms, e.g., generalized regression neural networks (GRNNs), back-propagation network (BPs), etc. This section briefly describes the above two neural networks.

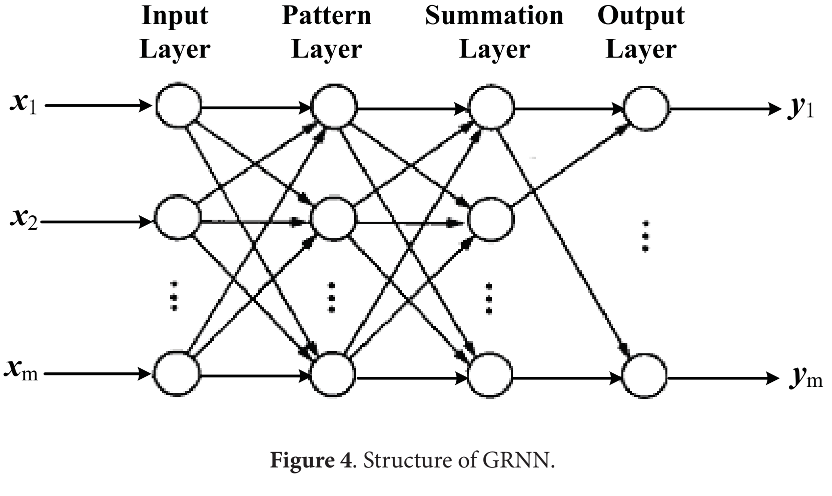

**Figure 4**. Structure of GRNN.

### 3.1 GENERALIZED REGRESSION NEURAL NETWORKS (GRNNS)

In 1991, Specht [24] proposed the generalized regression neural network (GRNN) as a variation of the radial basis function kernel (RBF) neural network, which approximates a function between the input and output vectors based on a standard statistical technique called kernel regression. The training time for the GRNN is relatively short, as the bandwidths of all the parameters are calculated, unlike the initial setting of the learning parameters. As the size of training set becomes larger, the estimation error approaches zero, while only minor restrictions are imposed on the function. The typical structure of a GRNN is shown in Fig.4.

Assume that *f*(*x*,*y*) represents the known joint continuous probability density function of a vector random variable, *x*, and a scalar random variable, *y*. Let ***X*** be a particular measured value of the random variable *x*. The conditional mean of *y* given ***X*** (also called the regression of *y* on ***X*** is given by

$$E[y\,|\,X]=\frac{\int_{-\infty}^{+\infty} yf(X,y)\,\mathrm{d}y}{\int_{-\infty}^{+\infty} f(X,y)\,\mathrm{d}y} \qquad (1)$$

When the density *f*(*x*,*y*) is not known, it must usually be estimated from a sample of observations of *x* and *y*. For a nonparametric estimate of *f*(*x*,*y*), we will use the class of consistent estimators proposed by Parzen [25] and shown to be applicable to the multi-dimensional case by Cacoullos [26]. As noted in Specht [27], these estimators are a good choice for estimating the probability density function, if it can be assumed that the underlying density is continuous and that the first partial derivatives of the function evaluated at any x are small. The probability estimator $\hat{f}(X,Y)$ is based upon the sample values $X_i$ and $Y_i$ of the random variables *x* and *y*, where *n* is the number of sample observations and *p* is the dimension of the vector variable *x*:

$$\hat{f}(X,Y)=\frac{1}{(2\pi)^{\frac{p+1}{2}}\sigma^{(p+1)}n}\sum_{i=1}^{n}\exp\left[-\frac{(X-X_i)^{\mathrm{T}}(X-X_i)}{2\sigma^2}\right]\cdot\exp\left[-\frac{(Y-Y_i)^2}{2\sigma^2}\right] \qquad (2)$$

A physical interpretation of the probability estimate $\hat{f}(X,Y)$ is that it assigns a sample probability of width *σ* for each sample $X_i$ and $Y_i$, and the probability estimate is the sum of those sample probabilities. Substituting the joint-probability estimate $\hat{f}(X,Y)$ in Equation (2) into the conditional mean, (1), gives the desired conditional mean of *y* given ***X***. In particular, combining Equation (1) and (2) and interchanging the order of integration and summation yields the desired conditional mean, designated $\hat{Y}(X)$:

$$\hat{Y}(X)=\frac{\sum_{i=1}^{n}\exp\left[-\frac{(X-X_i)^{\mathrm{T}}(X-X_i)}{2\sigma^2}\right]\int_{-\infty}^{+\infty} y\cdot\exp\left[-\frac{(y-Y_i)^2}{2\sigma^2}\right]\mathrm{d}y}{\sum_{i=1}^{n}\exp\left[-\frac{(X-X_i)^{\mathrm{T}}(X-X_i)}{2\sigma^2}\right]\int_{-\infty}^{+\infty}\exp\left[-\frac{(y-Y_i)^2}{2\sigma^2}\right]\mathrm{d}y} \qquad (3)$$

Defining the scalar function $D_i^2$,

$$D_i^2=(X-X_i)^{\mathrm{T}}(X-X_i) \qquad (4)$$

and performing the indicated integrations yields the following:

$$\hat{Y}(X)=\frac{\sum_{i=1}^{n}Y_i\exp\left(-\frac{D_i^2}{2\sigma^2}\right)}{\sum_{i=1}^{n}\exp\left(-\frac{D_i^2}{2\sigma^2}\right)} \qquad (5)$$

The resulting regression, (5), which involves summations over the observations, is directly applicable to problems involving numerical data.

The estimate $\hat{Y}(X)$ can be visualized as a weighted average of all of the observed values, $Y_i$, where each observed value is weighted exponentially according to its Euclidean distance from ***X***. When the smoothing parameter *σ* is made large, the estimated density is forced to be smooth and in the limit becomes a multivariate Gaussian with the covariance $\sigma^2\boldsymbol{I}$. On the other hand, a smaller value of *σ* allows the estimated density to assume non-Gaussian shapes, but with the hazard that wild points may have too great an effect on the estimate. As *σ* becomes very large, $\hat{Y}(X)$ assumes the value of the sample mean of the observed $Y_i$, and as *σ* goes to 0, $\hat{Y}(X)$ assumes the value of the $Y_i$ associated with the observation closest to ***X***. For intermediate values of *σ*, all the values of $Y_i$ are taken into account, but those corresponding to points closer to ***X*** are given greater weight.

When the underlying parent distribution is not known, it is not possible to compute an optimum *σ* for a given number of observations *n*. It is therefore necessary to find *σ* on an empirical basis. This can be done easily when the density estimate is being used in a regression equation because there is a natural criterion that can be used for evaluating each value of *σ*, i.e., the mean-squared error between $Y_i$ and the estimate $\hat{Y}(X_i)$. This procedure is used to avoid an artificial minimum error as $\sigma \to 0$ that results when the estimated density is allowed to fit the observed data points, that is

$$E=\frac{1}{n}\sum_{i=1}^{n}\left[\hat{Y}\left(X_i\right)-Y_i\right]^2 \qquad (6)$$

The principal advantages of the GRNN are the rapid learning and the convergence to the optimum regression surface as the number of samples becomes very large. The GRNN is particularly advantageous with sparse data in a real-time environment, because the regression surface is instantly defined everywhere, even with just one sample.

## 3.2 BACK-PROPAGATION NETWORK (BP)

The back-propagation neural is a multilayered, feed-forward neural network and is by far the most extensively used [28]. Back-propagation works by approximating the non-linear relationship between the input and the output by adjusting the weight values internally. A supervised learning algorithm of back-propagation is utilized to establish the neural network modelling. A normal back-propagation (BP) neural model consists of an input layer, one or more hidden layers, and an output layer (Fig.5).

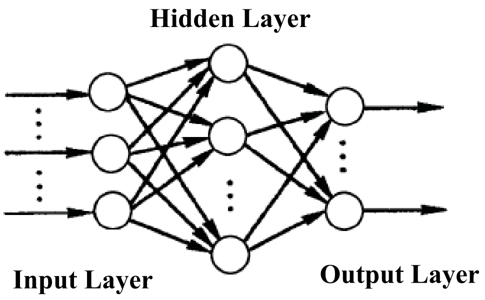

**Figure 5**. The back-propagation neural network model.

The BP technique is only outlined in this section, and for more details, the reader is referred, for example, to Freeman and Skapura [29].

1) Apply the input vector, $\mathbf{X}_p=\left(x_{p1},x_{p2},\cdots,x_{pN}\right)^{\mathrm{T}}$ to the input units.

2) Calculate the net-input values to the hidden layer units:
$$\mathrm{net}_{pj}^{h}=\sum_{i=1}^{N}w_{ji}^{h}x_{pi}+\theta_j^h \qquad (7)$$

3) Calculate the outputs from the hidden layer:
$$i_{pj}=f_j^h\left(\mathrm{net}_{pj}^h\right) \qquad (8)$$

4) Move to the output layer. Calculate the net-input values to each unit:
$$\mathrm{net}_{pk}^{o}=\sum_{j=1}^{L}w_{kj}^{o}i_{pj}+\theta_k^o \qquad (9)$$

5) Calculate the outputs:
$$o_{pk}=f_k^o\left(\mathrm{net}_{pk}^o\right) \qquad (10)$$

6) Calculate the error terms for the output units:
$$\delta_{pk}^{o}=\left(y_{pk}-o_{pk}\right)f_k^{o'}\left(\mathrm{net}_{pk}^o\right) \qquad (11)$$

7) Calculate the error terms for the hidden units:
$$\delta_{pj}^{h}=f_j^{h'}\left(\mathrm{net}_{pj}^h\right)\sum_k \delta_{pk}^o w_{kj}^o \qquad (12)$$
Notice that the error terms on the hidden units are calculated before the connection weights to the output layer units have been updated.

8) Update weights on the output layer:
$$w_{kj}^o\left(t+1\right)=w_{kj}^o\left(t\right)+\eta\delta_{pk}^o i_{pj} \qquad (13)$$

9) Update weights on the hidden layer:
$$w_{ji}^h\left(t+1\right)=w_{ji}^h\left(t\right)+\eta\delta_{pj}^h x_i \qquad (14)$$

where $i$ is the unit node in the input layer, $j$ is the unit node in the hidden layer, $p$ is the pattern and $k$ is related to the output layer, $\eta$ is the learning rate, $t$ is the $t^{\mathrm{th}}$ iteration, $\delta_{pk}^o$ and $\delta_{pj}^h$ are the error terms (which encompass a derivative part) for the output units and hidden units, respectively. $w_{ji}^h$ and $w_{kj}^o$ are the weights for the hidden units and output units, respectively.

## 4 CROSS-VALIDATION

Cross-validation is a technique for assessing how the results of statistical analyses can be generalized to an independent dataset. This technique is mainly used in situations where the goal is prediction, and one wants to estimate how accurately a predictive model will perform in practice [30].

This study adopts a *k*-fold cross-validation technique that randomly partitions the original sample into *k* subsamples. A single subsample is retained as validation data for testing the model, and the remaining *k*—1 subsamples are used as training data. The cross-validation process is repeated *k* times (the folds), with each of the *k* subsamples used exactly once as the validation data. The *k* results from the folds can be averaged (or otherwise combined) to produce a single estimation. Fig.6 provides an example of a *k*-fold cross-validation procedure.

Fig.7 shows the *k*-fold cross-validation error versus *k* for a large dataset, and indicates that a *k* value between 4

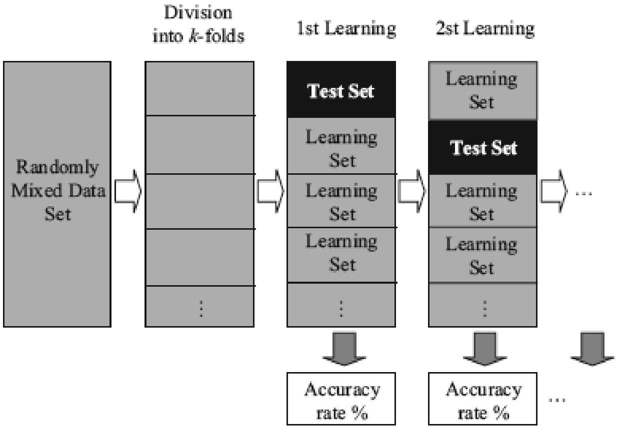

**Figure 6**. A *k*-fold cross-validation procedure [30].

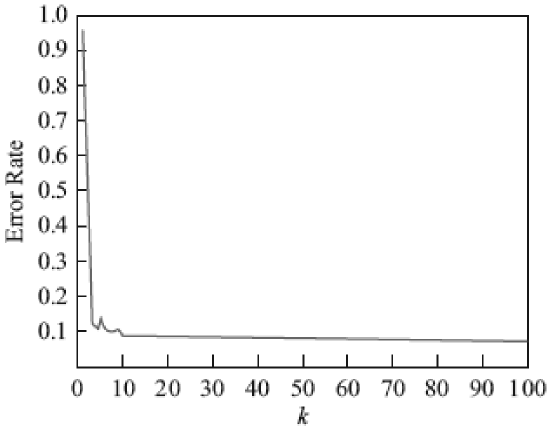

**Figure 7**. A plot of *k*-fold cross-validation errors vs. *k* [31].

and 10 is a good trade-off: increasing this value significantly increases the computation time and does not significantly improve the results [31]. Thus, this study adopts a 10-fold cross-validation. This approach may not be useful in achieving high training accuracy, but it can prevent the over-fitting problem.

In order to select the optimum value of $\sigma$, Specht [24] suggested the holdout method. The holdout method is the simplest kind of cross-validation. The data set is separated into two sets, called the training set and the testing set. The function approximator fits a function using the training set only. Then the function approximator is asked to predict the output values for the data in the testing set (it has never seen these output values before). The errors it makes are accumulated as before to give the mean absolute test-set error, which is used to evaluate the model. The advantage of this method is that it is usually preferable to the residual method and takes no longer to compute. However, its evaluation can have a high variance. The evaluation may depend heavily on which data points end up in the training set and which end up in the test set, and thus the evaluation may be significantly different depending on how the division is made. As a step further, in this paper the 10-fold cross-validation method was used. After the selection of a fixed value of $\sigma$, the model was trained using the training dataset. Then the model was evaluated using the test dataset. This process was repeated for each $k$=10 folds (90% for training and 10% for testing) and then many times using different values of the smoothing coefficient. Finally, the best value of $\sigma$ that should be used was selected as the value that minimized the error that was estimated as the average error rate on these cross-validation examples. The advantage of this method over repeated random subsampling (which is also known as the Monte Carlo variation, meaning that the results will vary if the analysis is repeated with different random splits) is that all the observations are used for both training and validation, and each observation is used for the validation exactly once. The main drawback of this method is that it requires intense computation.

## 5 CASE STUDIES

### 5.1 MODEL VALIDATION WITH EXPERIMENTAL DATA

Model development (i.e., model “training”) should be followed by a model validation to assess the predictive capability [32]. To evaluate the overall performance of the GRNN model, we compared the predictions against the experimental data. The case records listed in Table 1 are evaluated using the GRNN model. The database includes 25 experimental data from ref. [33]. And then, seven selected factors, which include various characteristic particle sizes, such as $d_{85}$, $d_{15}$, $d_5$, $d_{60}$, $d_{30}$, $d_{10}$, and the porosity $\Phi$ of non-cohesive soils, were taken into account as the input parameters of the GRNN model. Moreover, the seepage failure types of non-cohesive soils are also listed in Table 1; it is 1 for piping and 0 for soil flow.

As can be seen from Table 1, the predictions from the GRNN model agree well with the experimental data, and it has a high success rate (100%). These results indicate that our GRNN model seems to be a good tool for predicting the piping potential.

**Table 1**. Experimental data.

| | No. | $d_{85}$/mm | $d_{15}$/mm | $d_5$/mm | $d_{60}$/mm | $d_{30}$/mm | $d_{10}$/mm | $\Phi$ | Test results | Predicted results |
|---|---|---|---|---|---|---|---|---|---|---|
| Calibration | 1 | 7.00 | 0.37 | 0.20 | 3.50 | 0.60 | 0.29 | 0.44 | 0 | 0.0124 |
| | 2 | 5.90 | 0.29 | 0.15 | 2.10 | 0.50 | 0.20 | 0.28 | 0 | 0.0235 |
| | 3 | 4.40 | 0.15 | 0.11 | 2.70 | 1.10 | 0.13 | 0.28 | 1 | 0.9891 |
| | 4 | 5.10 | 0.22 | 0.12 | 2.60 | 1.13 | 0.14 | 0.28 | 1 | 0.9867 |
| | 5 | 7.00 | 0.21 | 0.12 | 4.10 | 2.60 | 0.16 | 0.28 | 1 | 0.9895 |
| | 6 | 6.68 | 0.21 | 0.11 | 4.00 | 2.10 | 0.16 | 0.28 | 1 | 0.9989 |
| | 7 | 5.00 | 0.20 | 0.11 | 2.20 | 1.05 | 0.13 | 0.34 | 1 | 0.9856 |
| | 8 | 5.60 | 0.25 | 0.12 | 3.30 | 2.00 | 0.20 | 0.31 | 1 | 0.9687 |
| | 9 | 4.30 | 0.19 | 0.12 | 3.70 | 2.30 | 0.15 | 0.35 | 1 | 0.9888 |
| | 10 | 5.00 | 0.26 | 0.16 | 3.50 | 2.10 | 0.18 | 0.29 | 1 | 0.9886 |
| | 11 | 5.00 | 0.30 | 0.11 | 3.20 | 2.10 | 0.18 | 0.33 | 1 | 0.9883 |
| | 12 | 5.00 | 0.23 | 0.15 | 3.10 | 2.10 | 0.17 | 0.34 | 1 | 0.9889 |
| | 13 | 7.00 | 0.25 | 0.17 | 4.10 | 2.30 | 0.19 | 0.29 | 1 | 0.9888 |
| | 14 | 6.00 | 0.20 | 0.15 | 3.40 | 2.00 | 0.17 | 0.30 | 1 | 0.9885 |
| | 15 | 5.00 | 0.21 | 0.15 | 3.00 | 1.70 | 0.18 | 0.30 | 1 | 0.9887 |
| | 16 | 7.50 | 0.23 | 0.16 | 2.00 | 0.40 | 0.19 | 0.28 | 0 | 0.0104 |
| | 17 | 5.30 | 0.23 | 0.16 | 2.30 | 0.50 | 0.19 | 0.30 | 0 | 0.0125 |
| | 18 | 0.42 | 0.14 | 0.04 | 0.37 | 0.24 | 0.12 | 0.40 | 0 | 0.0061 |
| | 19 | 0.30 | 0.02 | 0.01 | 0.12 | 0.06 | 0.02 | 0.43 | 0 | 0.0053 |
| | 20 | 0.19 | 0.02 | 0.01 | 0.10 | 0.07 | 0.02 | 0.39 | 0 | 0.0105 |
| Validation | 21 | 0.22 | 0.05 | 0.01 | 0.16 | 0.09 | 0.03 | 0.38 | 0 | 0.0054 |
| | 22 | 0.18 | 0.02 | 0.01 | 0.10 | 0.07 | 0.02 | 0.42 | 0 | 0.0015 |
| | 23 | 0.22 | 0.05 | 0.01 | 0.19 | 0.11 | 0.05 | 0.41 | 0 | 0.0031 |
| | 24 | 0.21 | 0.05 | 0.01 | 0.17 | 0.09 | 0.04 | 0.40 | 0 | 0.0073 |
| | 25 | 0.22 | 0.07 | 0.01 | 0.20 | 0.13 | 0.04 | 0.38 | 0 | 0.0112 |

## 5.2 PRACTICAL PROJECTS

In this section, an attempt has been made to predict the seepage piping of embankments with the help of the GRNN and BP. With chosen network parameters, 23 case studies containing the most necessary information of embankment structures, materials and states of seepage piping are filtered and selected from ref. [34, 35]. The 23 case records are shown in Table 2. A total of nine selected factors, which include the height of the

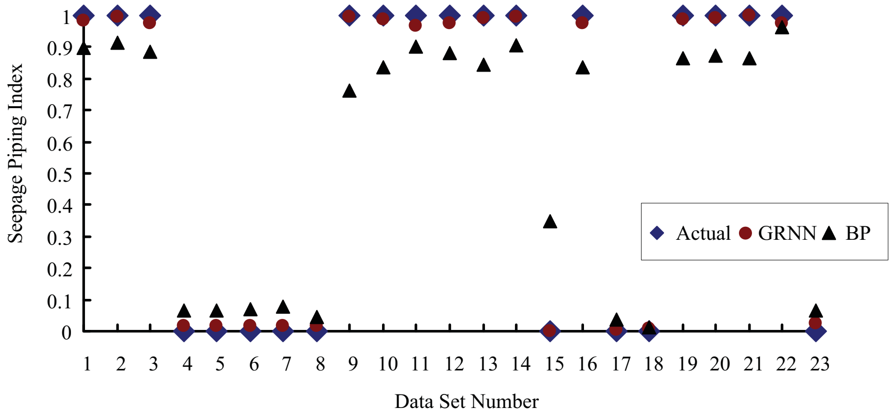

**Figure 8**. Comparison between forecasted and actual results.

**Table 2**. Practical projects data.

| | No. | H/m | $H_w$/m | $\lambda$ | $c$ /kPa | $\varphi$/° | $\gamma_{sat}$/kN/m$^3$ | $k$/cm/s | $d_b$/cm | $\delta$/° | Actual |
|---|---|---|---|---|---|---|---|---|---|---|---|
| Calibration | 1 | 133 | 123 | 0.455 | 40 | 27.0 | 21.3 | $3.0\times10^{-7}$ | 0.009 | 79.0 | 1 |
| | 2 | 87.5 | 80 | 0.4 | 12 | 28.9 | 21.2 | $3.5\times10^{-7}$ | 0.008 | 75.0 | 1 |
| | 3 | 35.5 | 31 | 0.295 | 60 | 15.6 | 20.5 | $1.0\times10^{-7}$ | 0.008 | 43.0 | 1 |
| | 4 | 31 | 29 | 0.249 | 20 | 26.7 | 20.8 | $4.0\times10^{-4}$ | 0.01 | 14.0 | 0 |
| | 5 | 31 | 29 | 0.249 | 15 | 26.7 | 20.1 | $7.8\times10^{-5}$ | 0.009 | 14.0 | 0 |
| | 6 | 29 | 25 | 0.435 | 30 | 31.6 | 20.8 | $2.0\times10^{-5}$ | 0.01 | 23.5 | 0 |
| | 7 | 39 | 35.5 | 0.466 | 109 | 21.2 | 20.7 | $5.1\times10^{-6}$ | 0.04 | 29.0 | 0 |
| | 8 | 39 | 35.5 | 0.466 | 76 | 13.8 | 20.7 | $5.1\times10^{-6}$ | 0.04 | 25.0 | 0 |
| | 9 | 28 | 25 | 0.286 | 157 | 13.2 | 20.3 | $3.6\times10^{-7}$ | 0.009 | 60.0 | 1 |
| | 10 | 28 | 25 | 0.286 | 153 | 24.8 | 21.2 | $4.8\times10^{-8}$ | 0.009 | 60.0 | 1 |
| | 11 | 96 | 90 | 0.417 | 20 | 26.0 | 21.0 | $3.5\times10^{-8}$ | 0.012 | 65.0 | 1 |
| | 12 | 56 | 49 | 0.364 | 30 | 29.0 | 19.5 | $2.0\times10^{-7}$ | 0.013 | 59.0 | 1 |
| | 13 | 51 | 47 | 0.308 | 42 | 34.5 | 21.2 | $2.2\times10^{-8}$ | 0.012 | 66.0 | 1 |
| | 14 | 133.1 | 126 | 0.476 | 41 | 32.0 | 21.7 | $1.3\times10^{-6}$ | 0.004 | 76.0 | 1 |
| | 15 | 13.0 | 10.5 | 0.364 | 44 | 38.4 | 22.9 | $1.0\times10^{-2}$ | 0.02 | 26.6 | 0 |
| | 16 | 6.7 | 5.5 | 0.4 | 109 | 21.2 | 20.7 | $5.1\times10^{-6}$ | 0.004 | 67.5 | 1 |
| | 17 | 6.0 | 4.75 | 0.5 | 51 | 38.5 | 20.9 | $7.0\times10^{-3}$ | 0.024 | 26.6 | 0 |
| | 18 | 87.5 | 80 | 0.256 | 14 | 27.0 | 21.2 | $4.0\times10^{-6}$ | 0.008 | 28.0 | 0 |
| | 19 | 51.5 | 46 | 0.455 | 100 | 19.3 | 21.0 | $2.9\times10^{-6}$ | 0.007 | 45.0 | 1 |
| Validation | 20 | 39.5 | 33 | 0.347 | 32 | 27.2 | 20.2 | $5.5\times10^{-8}$ | 0.01 | 67.0 | 1 |
| | 21 | 29.0 | 26 | 0.315 | 26 | 27.8 | 20.8 | $2.0\times10^{-5}$ | 0.01 | 65.0 | 1 |
| | 22 | 42.5 | 39 | 0.361 | 84 | 32.2 | 20.6 | $1.3\times10^{-8}$ | 0.004 | 53.1 | 1 |
| | 23 | 7.0 | 5.6 | 0.4 | 20 | 30.0 | 19.5 | $3.8\times10^{-5}$ | 0.017 | 26.6 | 0 |

**Table 3**. Comparison between forecasted and actual results.

| No. | Actual | GRNN | BP |
|---|---|---|---|
| 1 | 1 | 0.9845 | 0.8967 |
| 2 | 1 | 0.9971 | 0.9125 |
| 3 | 1 | 0.9764 | 0.8834 |
| 4 | 0 | 0.0164 | 0.0657 |
| 5 | 0 | 0.0183 | 0.0637 |
| 6 | 0 | 0.0171 | 0.0681 |
| 7 | 0 | 0.0157 | 0.0764 |
| 8 | 0 | 0.0162 | 0.0452 |
| 9 | 1 | 0.9967 | 0.7634 |
| 10 | 1 | 0.9863 | 0.8346 |
| 11 | 1 | 0.9657 | 0.9023 |
| 12 | 1 | 0.9753 | 0.8827 |
| 13 | 1 | 0.9912 | 0.8424 |
| 14 | 1 | 0.9961 | 0.9068 |
| 15 | 0 | 0.0013 | 0.3467 |
| 16 | 1 | 0.9735 | 0.8359 |
| 17 | 0 | 0.0054 | 0.0357 |
| 18 | 0 | 0.0067 | 0.0139 |
| 19 | 1 | 0.9893 | 0.8641 |
| 20 | 1 | 0.9931 | 0.8744 |
| 21 | 1 | 0.9987 | 0.8655 |
| 22 | 1 | 0.9734 | 0.9615 |
| 23 | 0 | 0.0258 | 0.0637 |

dam H, the water level $H_w$, the downstream slope ratio $\lambda$, the effective internal frictional angle $\varphi$, the effective cohesion $c$, the saturated unit weight $\gamma_{sat}$, the coefficient of permeability $k$, the maximum effective particle size $d_b$ and the inclination angle of the seepage filter $\delta$, were taken into account as the input parameters for the artificial neural network systems. The neural network output consisted of a single neuron representing the piping potential. The neuron was given a binary value of 1 for seepage piping occurrence. A comparison between the forecasted and actual results is shown in Table 3 and Fig.8. From the results obtained here, it can be said that the GRNN demonstrates superiority over the BP technology. These results suggest that the GRNN is potentially useful for predicting seepage-piping occurrence.

## 6 CONCLUSIONS

Piping is known to cause the catastrophic failures of levees and earthen dams and has been studied for nearly a century. The factors that influence the piping occurring in embankments are uncertain and random, and in the process of piping they turn out to be a nonlinear behaviour. In order to estimate the risks of dam failure phenomena, it is necessary to develop scientifically derived analytical models that are simpler, easier to implement, and more accurate than traditional methods for the evaluation of piping potential. In this paper, the GRNN technique was chosen to predict the seepage-piping potential. The performance of the GRNN was cross-validated using the *k*-fold cross-validation technique. From these studies, the following conclusions and recommendations may be drawn:

(1) The above results show that the GRNN model is efficient for predicting the occurrence of seepage piping with high accuracy and it is expected to be very reliable for the evaluation of the piping potential. Thus, the GRNN is a powerful piping-assessment tool worthy of promotion and support.

(2) The main factors that affect the erosion phenomenon are: 1) the erodibility of the soil; 2) the water velocity inside the soil mass; 3) the geometry of the earth structure, and so on. As can be seen, the mechanism of piping is very complicated and needs to be further investigated through laboratory and field tests. Meanwhile, the advanced digital photographic video tracing technique, image processing technology, etc., should also be introduced into the mechanism research of piping phenomenon.

(3) The performance of the GRNN is dependent on the smoothing parameter, and the appropriate smoothing parameter can minimize the misclassification rate or the error of the final network. Thus, to improve the prediction performance of GRNN models, it is necessary to study the optimization algorithms in future investigations.

## REFERENCES

[1] Xu, Y., Zhang, L.M.(2009). Breaching parameters of earth and rockfill dams, J. Geotech. Geoenviron. Eng., ASCE 135, 12, 1957-1970.
[2] Foster, M., Fell, R., Spannagle, M. (2000). The statistics of embankment dam failures and accidents, Can. Geotech. Journal 37, 5, 1000-1024.
[3] Zhang, L.M., Xu, Y., Jia, J.S. (2009). Analysis of earth dam failures-A database approach, Georisk 3, 3, 184 -189.
[4] Richards, K.S., Reddy, K.R. (2012). Experimental investigation of initiation of backward erosion piping in soils, Géotechnique 62, 10, 933-942.
[5] Terzaghi, K., Der. (1922). Grundbruch an Stauwerken und seine Verhütung, In From theory to practice in soil mechanics (1960), New York, NY, USA: John Wiley & Sons (in German), 445-449.
[6] Bligh, W.G. (1910).Dams, barrages and weirs on porous foundations, Eng. News 64, 26, 708-710.
[7] Lane, E.W. (1934). Security from under-seepage masonry dams on earth foundations, Trans. ASCE, 100, 1, 1235-1272.
[8] Kevin, S.R., Krishna, R.R. (2007). Critical appraisal of piping phenomena in earth dams, Bull. Eng. Geol. Environ. 66, 381-402.
[9] Xue, X.H.,Yang, X.G. (2013). Application of the adaptive neuro-fuzzy inference system for prediction of soil liquefaction, Nat. Hazards 67, 901-917.
[10] Saman, Y.S., Hing, H.T. (2011). A new site classification approach based on neural networks, Soil Dyn. Earthq. Eng., 31, 974-981.
[11] Kamali, M., Ataei, M. (2011). Prediction of blast induced vibrations in the structures of Karoun III power plant and dam, J. Vib. Control 17, 4, 541-548.
[12] Tesfamariam, S., Liu, Z. (2010). Earthquake induced damage classification for reinforced concrete buildings, Struct. Saf. 32, 2, 154-164.
[13] Senouci, A.B., Adeli, H. (2001). Resource scheduling using neural dynamics model of Adeli and Park, J. Constr. Eng. M., ASCE 127, 1, 28-34.
[14] Yang, Y., Rosenbaum, M.S. (2002). The artificial neural network as a tool for assessing geotechnical properties, Geotech. Geol. Eng. 20, 149-168.
[15] Cichocki, A., Zdunek, R. (2007). Multilayer nonnegative matrix factorization using projected gradient approaches, Int. J. Neural Syst. 17, 6, 431-446.
[16] Lakshmi, S.S., Tiwari, R.K. (2009). Model dissection from earthquake time series: a comparative analysis using modern non-linear forecasting and artificial neural network approaches, Comput. Geosci. 35, 2, 191-204.
[17] Fell, R., Fry. J.J. (2007). The state of art of assessing the likelihood of internal erosion of embankment dams, water retaining structures and their foundations, Internal Erosion of Dams and their Foundations, Taylor & Francis, London.
[18] Foster, M.A., Fell, R. (1999).A framework for estimating the probability of failure of embankment dams by piping using event tree methods. UNICIV Report No.R-377. The University of New South Wales, Sydney, Australia.
[19] Rice, J.D., Duncan, J.M. (2007).Davidson, R.R.: Identification of failure mechanisms associated with seepage barriers in dams. GSP 161 Embankments, Dams, and Slopes Geo-Denver 2007: New Peaks in Geotechnics, 1-11.

[20] Rice, J.D., Duncan, J.M. (2008).A study on the long-term performance of seepage barriers in dams. Virginia Tech Center for Geotechnical Practice and Research Publication 49.
[21] Rice, J.D., Duncan, J.M. (2010). Findings of case histories on the long-term performance of seepage barriers in dams. Journal of Geotechnical and Geoenvironmental Engineering, ASCE 136, 1, 2-15.
[22] Gholam, R.R., Mohammad, V., Mehdi, A.A. (2012). Forecasting groundwater level in Shiraz Plain using artificial neural networks, Arab.J.Sci.Eng. 37, 1871-1883.
[23] Seyed, S.E., Seyed, A.G.,Mohammad, J.Z., Alireza, F. (2012). Estimating Penman-Monteith reference evapotranspiration using artificial neural networks and genetic algorithm: a case study, Arab.J.Sci.Eng. 37, 935-944.
[24] Specht, D.F. (1991). A general regression neural network, IEEE T. Neural Network 2, 6, 568 -576.
[25] Parzen, E. (1962).On estimation of a probability density function and mode. Annals of Mathematical Statistics 33,1065-1076.
[26] Cacoullos, T. (1966). Estimation of a multivariate denstiy. Annals of the Institute of Statistical Mathematics 18, 2,179-189.
[27] Specht, D. F. (1967). Generation of polynomial discriminant functions for pattern recognition. IEEE Transactions on Electronic Computers (EC-16),308-319.
[28] Lee, M.C., To Chang (2010). Comparison of support vector machine and back propagation neural network in evaluating the enterprise financial distress, International Journal of Artificial Intelligence & Applications 1, 3, 31-43.
[29] Freeman, A.J., Skapura, M.D. (1991). Neural networks: Algorithms, Application and Programming Techniques. Addition Wesley Publications Company, Inc.
[30] Lee, C.Y., Chern, S.G. (2013). Application of a support vector machine for liquefaction assessment, J.Mar.Sci. Tech. 21, 3, 318-324.
[31] Sterkubm, P. (2007). Overfitting prevention with cross-validation, Paris.
[32] Oommen, T., Baise, L.G.,Vogel, R. (2010). Validation and application of empirical liquefaction models, J.Geotech.Geoenviron.Eng. 136, 12, 1618-1633.
[33] Zhao, Z.X., Chen, J.S., Chen L. (2008). Application of BP neural network to assessment of noncohesive piping-typed soils, Chinese J. Geot. Eng., 30, 4, 536-540. (in Chinese)
[34] Liu, J. (1992). Soil seepage stability and seepage control, China WaterPower Press, Beijing. (in Chinese)
[35] Zheng, W.L., Shen, M.S. (1995).A study of piping in earth dams, J. of Chinese Institute Civil and Hydraulic Engineering 7, 3, 283- 295. (in Chinese)

# OPTIMIZACIJA NAČRTOVANJA SIMETRIČNIH GRAVITACIJSKIH PODPORNIH ZIDOV

EROL SADOĞLU

## o avtorju

Erol Sadoğlu
Karadeniz Technical University,
Faculty of Engineering
Trabzon, Turčija
E-pošta: erolsadoglu@hotmail.com

## izvleček

*V članku je predstavljena optimizacija simetričnih gravitacijskih podpornih zidov različnih velikosti. Razvit je bil optimizacijski problem zveznih funkcij. Zvezne funkcije predstavljajo namenska funkcija, definirana kot območje prereza zidu in omejitvene funkcije, ki izpolnjujejo pogoje zunanje in notranje stabilnosti. Preverjeni so prevračanje, zdrs, nosilnost temeljnih tal ter strižna in upogibna nosilnost zidu. Za raziskavo oblike optimalnega prereza in vpliva višine zidu na obliko so bile izbrane višine zidov 2.0, 3.0 in 4.0 m. Upoštevane so bile konstantne fizikalne in mehanske lastnosti zemljine z namenom možnosti primerjav vpliva višine na geometrijo. Podrobno so navedene zgornje in spodnje meje območja rešitev, medtem ko minimalne dimenzije gravitacijskih podpornih zidov niso bile upoštevane. Pri optimalnem prerezu različno visokih zidov je običajno, da je zelo širok temelj zidu in tanjši vertikalni del. Pri optimalni vrednosti spremenljivk ni merodajen pogoj stabilnosti na zdrs ampak pogoj upogibne nosilnosti prereza.*

## ključne besede

gravitacijski podporni zidov, nelinearna optimizacija, zvezne spremenljivke, notranja točkovna metoda

# DESIGN OPTIMIZATION FOR SYMMETRICAL GRAVITY RETAINING WALLS

EROL SADOĞLU

## about the author

Erol Sadoğlu
Karadeniz Technical University,
Faculty of Engineering
Trabzon, Turkey
E-mail: erolsadoglu@hotmail.com

## Abstract

*The optimization for symmetrical gravity retaining walls of different heights is examined in this study. For this purpose, an optimization problem of continuous functions is developed. The continuous functions are the objective function defined as the cross-sectional area of the wall and the constraint functions derived from external stability and internal stability verifications. The verifications are listed as the overturning, the forward sliding, the bearing capacity, the shears in the stem and the bendings in the stem. The heights of the walls are selected as 2.0, 3.0, and 4.0 m in order to investigate the outline of the optimum cross-section and the effect of the wall height on the outline. Additionally, the physical and mechanical properties of the soil are kept constant in order to compare only the effect of the height on the geometry. The upper and lower bounds of the solution space are specified to be as wide as possible and the minimum dimensions suggested for the gravity retaining walls are not taken into account. A common feature of the optimum cross-sections of walls with different heights is to have a very wide lower part like a wall foundation and a slender stem. However, other than the forward sliding constraint, the bending constraints are active at the optimum values of the variables.*

## Keywords

gravity retaining wall, nonlinear optimization, continuous variables, interior point method

## 1 INTRODUCTION

A difference in the ground elevation over a random horizontal distance is usually confronted during the use of land for civil engineering purposes. The first solution to this situation is brought into being by organizing a slope. However, in some cases the proposed slope cannot support itself, and so another kind of solution called a retaining structure is required. Thus, earth-retaining structures are normally used to support soils and structures in order to maintain a difference in the elevation of the ground surface and are normally grouped into gravity walls, embedded walls, and reinforced earth walls [1].

The weight of the gravity wall provides the required stability against the effects of the retained soil and the ground water. This type of wall is generally constructed of plain concrete and masonry. In some cases, the provision of sand, gravel and cement are easier and cheaper than masonry, so it is preferable to use concrete as a construction material rather than masonry. Various cross-sections of gravity retaining walls are given in Fig. 1.

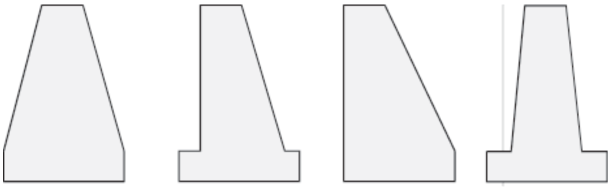

**Figure 1**. Cross-sections of gravity retaining walls.

The retained soil provides pressure, known as earth pressure, on the back face of the retaining wall, since the horizontal deformation of the soil is restricted by the retaining wall. One of the most crucial stages when designing a retaining wall is the determination of the earth pressure. There are several theories (Coulomb's theory [2], Rankine's theory [3], etc.) and approaches (Terzaghi-Peck Charts [4] and finite-element analysis [5,6,7,8,9]) to determine the earth pressures.

There have been a lot of studies to calculate the passive or active earth pressure since Coulomb's theory [2,3,10,11,12]. However, because of its simplicity, Rankine's theory [3] is still widely used for the determination of earth pressures acting on retaining walls. The theory is based on the assumptions that the soil is in a state of plastic equilibrium and that the Mohr-Coulomb failure criterion is valid [2]. Thus, Rankine obtained the formula below to calculate the lateral pressures on vertical planes within a mass of homogeneous, isotropic, and cohesionless soil behind a smooth wall:

$$\sigma_i = K_i \, \sigma_v = K_i \, \gamma_n \, z \qquad (i=a,\, p) \qquad (1)$$

$$K_a = \tan^2\left(45 - \frac{\phi}{2}\right) \qquad (2)$$

$$K_p = \tan^2\left(45 + \frac{\phi}{2}\right) \qquad (3)$$

where:

$K_a$ = Coefficient of earth pressure in the active state
$K_p$ = Coefficient of earth pressure in the passive state.
$\sigma_a$ = Lateral soil pressure in the active state
$\sigma_p$ = Lateral soil pressure in the passive state
$\sigma_v$ = Vertical pressure
$\phi$ = Internal friction angle

The proper design of a gravity retaining wall satisfies both the external and internal stability. The external stability is related to the interaction of the wall with the surrounding soil. The stability is ensured by verifying some failures, called sliding (on the ground), overturning, bearing capacity, and overall failures. In this way it is shown that the wall remains fixed in the desired place. The external stability verifications are carried out by defining a factor of safety, which is the ratio of the stabilizing forces (or moments) over the destabilizing forces (or moments).

The internal stability requirements are satisfied by developing a structural design with sufficient structural integrity to resist the applied loads safely [13]. The design of the wall may be carried according to the *Building Code Requirements for Structural Concrete* (ACI 318-99) [14]. The ACI code uses the ultimate strength design. Therefore, the computed loads are multiplied by the ACI load factors, which are equal to 1.6 for the earth pressure loads and 1.2 for the dead loads. However, this method uses a resistance factor (0.85) to the ultimate capacity for a strength-limit analysis. As a result, an evaluation between the factored forces and the nominal capacity is made. More obviously, the internal stability is checked in terms of the bending and shear verifications for some sections of the wall (Fig. 2).

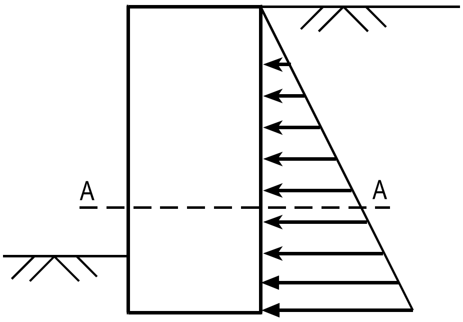

**Figure 2**. Shear and bending verifications.

Optimization is the process of obtaining the 'best', if it is possible to measure and change what is 'good' or 'bad'. Optimization practice, on the other hand, is the collection of techniques, methods, procedures, and algorithms that can be used to find the optima. Optimization problems are abundant in various fields of engineering, like electrical, mechanical, civil, chemical, and structural engineering. In recent decades, optimization methods have been widely applied to the problems of geotechnical engineering [15,16,17,18,19].

There are several general approaches to optimization, including analytical methods, graphical methods, experimental methods, and numerical methods. Analytical methods are based on the classical techniques of differential calculus and cannot be applied to highly nonlinear problems and problems involving more than two or three independent variables. Graphical methods require a plot of the function to be maximized and minimized. However, the number of independent variables does not exceed two. Experimental methods use a setup and change variables while the performance criterion is measured directly in each case (e.g., the Standard Proctor Test). Numerical methods can be used to solve highly complex optimization problems of the type that cannot be solved analytically. The discipline encompassing the theory and practice of numerical optimization methods has come to be known as mathematical programming. The branches of mathematical programming are linear programming, integer programming, quadratic programming, nonlinear programming, and dynamic programming.

The most general class of optimization problems that has both nonlinear objective functions and constraint functions is nonlinear programming. These problems can be solved using a variety of methods, such as penalty- and barrier-function methods, gradient projection methods, sequential quadratic-programming (SQP) methods, interior point methods, etc.

Rhomberg and Street [20] presented a method of proportioning for cantilever walls. The design variables were selected as the base size, the proportion of the stem to the base, the thickness and the reinforcing of the stem. Many combinations of the selected design parameters were evaluated to satisfy the basic design requirements for a minimum factor of safety, a maximum toe pressure and a minimum cost. Thus, the trial proportions were provided.

Alshawi et al. [21] proposed a new type of retaining wall called a tied-back retaining wall, for which the stem is tied to the base with inclined ties. The design bending moments were calculated for various dimensions of the retaining wall and various positions of the tie system. They found the position for the tie system where the design bending moment is a minimum. For this position of the tie system, the bending moments are greatly reduced with respect to that of the cantilever retaining wall. The design tables of the optimum cases were presented.

Other researchers also developed constrained nonlinear programming problems dealing with cantilever retaining walls [22,23]. The design variables were generally chosen as the total base width, the toe projection, the stem thickness at the bottom, the thickness of the base slab, the vertical steel area of the stem per unit length of the wall, the horizontal steel area of the toe per unit length of the wall, the horizontal steel area of the heel per unit length of the wall, etc. The total cost of the reinforced concrete wall was considered as the objective function for the analysis. The constraints were derived not only from structural safety and stability considerations but also some code provisions and practice. Sensitivity analyses were carried out to study the effect of the variation of problem parameters on the objective function.

In this work, a constrained nonlinear programming problem is defined and solved in order to find the general outline of a plain concrete gravity retaining wall in a cohesionless soil. The constraints are derived from external and internal stability criteria and the objective function is defined as the cross-sectional area of the wall. The nonlinear programming problem is solved using the interior point method.

## 2 OPTIMIZATION PROCEDURE

The engineering aspects that govern the design of a retaining wall are safety, stability, and cost. Safety and stability are interconnected concepts, i.e., the results of stability verifications provide information about safety, since safety is defined mostly on the results of stability verifications. Cost requires building with enough safety and usability for the least cost. Therefore, the cost of the wall should be minimized while some verifications are fulfilled. Consequently, the design of a gravity retaining wall can be thought of as an optimization problem. Clearly, a cost-related function emerges as an objective function and the constraints are derived from the stability verifications. The design variables of this optimization problem are chosen as the thicknesses of the gravity retaining wall at regular distances from the base (Fig. 3). The vertical distances between the thicknesses are chosen as one-sixth of the wall's height. Thus, the number of design parameters is prevented from becoming too large and sufficient points are determined in order to obtain the optimum outline of the concrete gravity retaining wall.

### 2.1 OBJECTIVE FUNCTION

An objective function is a mathematical expression that should be maximized or minimized in certain conditions and chosen as the volume, cost, weight, etc. in structural engineering [24]. The aim of this optimization problem is to determine the cross-section of the wall that minimizes the cost. Therefore, the objective function is chosen as the cross-sectional area, because the cost of the formwork and the scaffolding is mainly dependent on the wall's height. Thus, the wall with

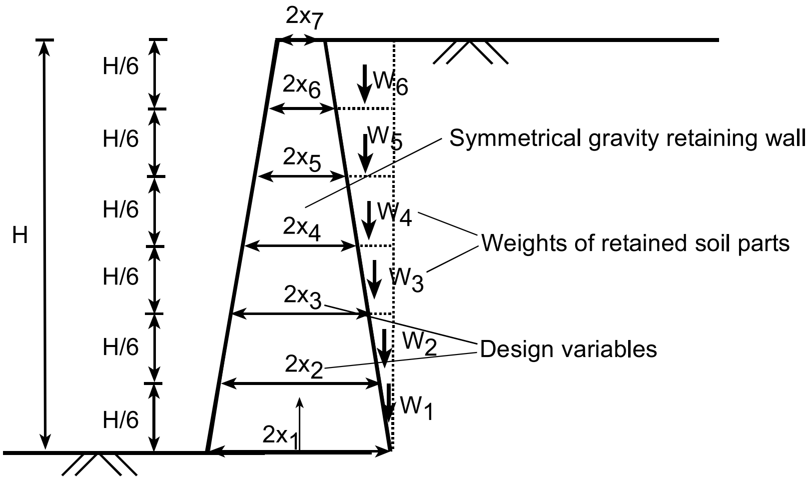

**Figure 3**. Design variables of gravity retaining wall.

minimum cross-sectional area can be considered to have the lowest cost.

$$f(x)=\frac{H}{6}(x_1+2x_2+2x_3+2x_4+2x_5+2x_6+x_7) \quad (4)$$

## 2.2 CONSTRAINTS

The design of a gravity retaining wall must ensure that the wall has enough external and internal stability. External stability is satisfied if the wall remains fixed in its desired position, except for small movements causing active and passive states in the nearby soil. The forces causing instability are the resultant of earth pressures in this case. The earth pressures are calculated according to Rankine's Theory [3]. Duncan et al. [25] proposed the following external stability criteria for granular backfill and foundation soils:

a) $N$ within the middle third of the base ($N$ = the sum of vertical forces acting on the wall),
b) $q_{\text{allowable}} \geq q_{\max}$, ($q_{\text{allowable}}$ = allowable bearing capacity, $q_{\max}$ = maximum base pressure)
c) Safe against sliding,
d) Settlement within tolerable limits

Overturning about the toe criterion is often met in the design stage in addition to the foregoing criteria. The settlement criterion is mainly related to the layers beneath the wall, and therefore it is neglected in this study.

Internal stability guarantees that the wall carries the loads acting on it without rupturing. In other words, a gravity retaining wall must be capable of resisting the internal shear forces and bending moments caused by earth pressures and for other reasons. Apparently, the distribution and magnitude of lateral earth pressures should be known to find the internal forces and moments to evaluate the internal stability criteria. The lateral earth pressure is calculated according to Rankine's theory, because it is widely used and easily adapted to this optimization study [3].

### 2.2.1 overturning constraint

The factor of safety against overturning is determined by dividing the resisting moments by the driving moments. The resisting moments are caused by the weight of the wall and the weight of the retained soil above the base of the wall (Fig 3.). The driving moment is the overturning effect of the active earth pressure. However, the factor of safety depends on the point around which we compute the moments. The overturning stability is evaluated only around the toe point in practice [13]. The constraint from overturning about the toe is derived as below.

$$\begin{aligned}
g_1(\mathrm{x}) = {} & \mathrm{FS_o}\cdot\frac{\gamma_n}{6}\cdot H^3\cdot K_a-\frac{H}{6}\gamma_c\left(x_1+2x_2+2x_3+2x_4+2x_5+2x_6+x_7\right)x_1\\
& -\frac{H}{12}\gamma_n[\left(x_1-x_2\right)\left(2x_1-\frac{\left(x_1-x_2\right)}{3}\right)\\
& +\left(2x_1-x_2-x_3\right)\left(2x_1-\frac{\left(x_1-x_3\right)^2+\left(x_1-x_3\right)\left(x_1-x_2\right)+\left(x_1-x_2\right)^2}{3\left(2x_1-x_3-x_2\right)}\right)\\
& +\left(2x_1-x_3-x_4\right)\left(2x_1-\frac{\left(x_1-x_4\right)^2+\left(x_1-x_4\right)\left(x_1-x_3\right)+\left(x_1-x_3\right)^2}{3\left(2x_1-x_4-x_3\right)}\right)\\
& +\left(2x_1-x_4-x_5\right)\left(2x_1-\frac{\left(x_1-x_5\right)^2+\left(x_1-x_4\right)\left(x_1-x_5\right)+\left(x_1-x_4\right)^2}{3\left(2x_1-x_5-x_4\right)}\right)\\
& +\left(2x_1-x_5-x_6\right)\left(2x_1-\frac{\left(x_1-x_6\right)^2+\left(x_1-x_5\right)\left(x_1-x_6\right)+\left(x_1-x_5\right)^2}{3\left(2x_1-x_6-x_5\right)}\right)\\
& +\left(2x_1-x_6-x_7\right)\left(2x_1-\frac{\left(x_1-x_7\right)^2+\left(x_1-x_6\right)\left(x_1-x_7\right)+\left(x_1-x_6\right)^2}{3\left(2x_1-x_6-x_7\right)}\right)]\leq 0
\end{aligned} \quad (5)$$

where:

$\gamma_n$ = Unit weight of the soil
$\gamma_c$ = Unit weight of the concrete.
$FS_o$= Factor of safety against overturning

### 2.2.2 sliding constraint

The sliding verification is carried out by comparing the forces causing the sliding with the forces resisting it. The earth pressure acting on the back of the wall is the only sliding force and the friction along the bottom of the base is the only resisting force in this case. The resultant of the friction is calculated by multiplying the weight of the wall and the soil acting as part of the wall by the coefficient of the base friction. Thus, the sliding constraint is defined as follows:

$$\begin{aligned}
g_2(x) = {} & FS_s\left(\frac{1}{2}\gamma_n H^2 K_a\right)-[\frac{H}{6}\gamma_c(x_1+2x_2+2x_3+\\
& 2x_4+2x_5+2x_6+x_7)+\\
& \frac{H}{12}\gamma_n((x_1+x_2)+(2x_1-x_2-x_3)+(2x_1-x_3-x_4)\\
& +(2x_1-x_4-x_5)\\
& +(2x_1-x_5-x_6)+(2x_1-x_6-x_7))]\tan\delta\leq 0
\end{aligned} \quad (6)$$

where:

$\tan\delta$ = Friction coefficient between the wall base and the foundation soil
$FS_s$ = Factor of safety against sliding

### 2.2.3 Total vertical forces within the middle third of the base constraint

Duncan et al. [25] suggested that eccentricity should be within the middle third of the base. Thus, the separation between the wall base and the soil does not occur. This constraint is inspired by the idea that tensile stresses do not develop in the base-pressure distribution. The constraint is given as below:

$$
\begin{aligned}
& g_3(x)=\{\frac{1}{6}\gamma_n H^3 K_a-\frac{H}{12}\gamma_n[(x_1-x_2)\left(x_1-\frac{(x_1-x_2)}{3}\right)+ \\
& (2x_1-x_2-x_3)\left(x_1-\frac{(x_1-x_3)^2+(x_1-x_3)(x_1-x_2)+(x_1-x_2)^2}{3(2x_1-x_2-x_3)}\right)+ \\
& (2x_1-x_3-x_4)\left(x_1-\frac{(x_1-x_3)^2+(x_1-x_3)(x_1-x_4)+(x_1-x_4)^2}{3(2x_1-x_3-x_4)}\right)+ \\
& (2x_1-x_4-x_5)\left(x_1-\frac{(x_1-x_4)^2+(x_1-x_4)(x_1-x_5)+(x_1-x_5)^2}{3(2x_1-x_4-x_5)}\right)+ \\
& (2x_1-x_4-x_5)\left(x_1-\frac{(x_1-x_4)^2+(x_1-x_4)(x_1-x_5)+(x_1-x_5)^2}{3(2x_1-x_4-x_5)}\right)+ \\
& (2x_1-x_5-x_6)\left(x_1-\frac{(x_1-x_5)^2+(x_1-x_5)(x_1-x_6)+(x_1-x_6)^2}{3(2x_1-x_5-x_6)}\right)+ \\
& (2x_1-x_6-x_7)\left(x_1-\frac{(x_1-x_6)^2+(x_1-x_6)(x_1-x_7)+(x_1-x_7)^2}{3(2x_1-x_6-x_7)}\right)]\}/\left(4x_1^2/6\right)- \\
& \{\frac{H}{6}\gamma_c(x_1+2x_2+2x_3+2x_4+2x_5+2x_6+x_7)+\frac{H}{12}\gamma_n((x_1-x_2)+(2x_1-x_2-x_3)+ \\
& (2x_1-x_3-x_4)+(2x_1-x_4-x_5)+(2x_1-x_5-x_6)+(2x_1-x_6-x_7))\}/(2x_1)\leq 0
\end{aligned}
\tag{7}
$$

## 2.2.4 Bearing capacity constraint

Bearing-capacity failure happens in soil when the contact pressure between the footing and the soil causes shear failure in the foundation soil. In this optimization problem the Terzaghi bearing-capacity theory [26] is used to calculate the safe bearing capacity and compared with the maximum base pressure. The constraint from the bearing-capacity failure is given as below:

$$
\begin{aligned}
& g_4(x)=\{\frac{1}{6}\gamma_n H^3 K_a-\frac{H}{12}\gamma_n[(x_1-x_2)\left(x_1-\frac{(x_1-x_2)}{3}\right)+ \\
& (2x_1-x_2-x_3)\left(x_1-\frac{(x_1-x_3)^2+(x_1-x_3)(x_1-x_2)+(x_1-x_2)^2}{3(2x_1-x_2-x_3)}\right)+ \\
& (2x_1-x_3-x_4)\left(x_1-\frac{(x_1-x_3)^2+(x_1-x_3)(x_1-x_4)+(x_1-x_4)^2}{3(2x_1-x_3-x_4)}\right)+ \\
& (2x_1-x_4-x_5)\left(x_1-\frac{(x_1-x_4)^2+(x_1-x_4)(x_1-x_5)+(x_1-x_5)^2}{3(2x_1-x_4-x_5)}\right)+ \\
& (2x_1-x_5-x_6)\left(x_1-\frac{(x_1-x_5)^2+(x_1-x_5)(x_1-x_6)+(x_1-x_6)^2}{3(2x_1-x_5-x_6)}\right)+ \\
& (2x_1-x_6-x_7)\left(x_1-\frac{(x_1-x_6)^2+(x_1-x_6)(x_1-x_7)+(x_1-x_7)^2}{3(2x_1-x_6-x_7)}\right)]\} \\
& /\left(4x_1^2/6\right)+\{\frac{H}{6}\gamma_c(x_1+2x_2+2x_3+2x_4+2x_5+2x_6+x_7) \\
& \qquad )+\frac{H}{12}\gamma_n((x_1-x_2)+(2x_1-x_2-x_3)+ \\
& \qquad {}_1-x_3-x_4)+(2x_1-x_4-x_5)+(2x_1-x_5-x_6)+ \\
& \qquad (2x_1-x_6-x_7))\}/(2x_1)-\frac{\gamma_n x_1 N_\gamma}{FS_b}\leq 0
\end{aligned}
\tag{8}
$$

where:

$N_\gamma$ = Bearing capacity factor
$FS_b$ = Factor of safety against bearing capacity failure

## 2.2.5 Shear verification constraints

Shear and bending verifications are carried out to satisfy and verify the internal stability of the retaining wall. Therefore, the shear capacity of the different stem sections of a concrete gravity wall is calculated according to the *Building Code Requirements for Structural Concrete* [14]. As there are no stirrups, the concrete of the stem must have adequate capacity to resist the shear force. The nominal shear capacity is:

$$V_n/b=\frac{1}{6}b_w d\sqrt{f_c'} \tag{9}$$

where:

$V_n/b$ = Nominal shear capacity per unit length of the wall
$b_w$ = Width of shear surface (unit length for the wall)
$d$ = Effective depth (thickness of the stem)
$f_c'$ = 28-day compressive strength of the concrete

ACI 318 uses the ultimate strength design so the computed lateral earth pressures must be multiplied by the load factors. The factors for earth pressure and dead load are 1.6 and 1.2, respectively.

The stem must have adequate thickness so that the following condition is fulfilled.

$$V_u/b\leq 0.5\varphi V_n\ /b \tag{10}$$

where:

$V_u/b$ = Factorized shear force per unit length of the wall.
$\varphi$ = Resistance factor = 0.85

As a result, the following constraints are obtained for five different sections, from the bottom to the top.

$$
\begin{aligned}
& g_5(\mathrm{x})=1.6\cdot\frac{1}{2}\cdot\gamma_z\cdot\left(\frac{H}{6}\right)^2\cdot K_a-\frac{0.85}{6}\cdot x_6\cdot\sqrt{f_c'}\leq 0 \\
& g_6(\mathrm{x})=1.6\cdot\frac{1}{2}\cdot\gamma_z\cdot\left(\frac{H}{3}\right)^2\cdot K_a-\frac{0.85}{6}\cdot x_5\cdot\sqrt{f_c'}\leq 0 \\
& g_7(\mathrm{x})=1.6\cdot\frac{1}{2}\cdot\gamma_z\cdot\left(\frac{H}{2}\right)^2\cdot K_a-\frac{0.85}{6}\cdot x_4\cdot\sqrt{f_c'}\leq 0 \\
& g_8(\mathrm{x})=1.6\cdot\frac{1}{2}\cdot\gamma_z\cdot\left(\frac{2H}{3}\right)^2\cdot K_a-\frac{0.85}{6}\cdot x_3\cdot\sqrt{f_c'}\leq 0 \\
& g_9(\mathrm{x})=1.6\cdot\frac{1}{2}\cdot\gamma_z\cdot\left(\frac{5H}{6}\right)^2\cdot K_a-\frac{0.85}{6}\cdot x_2\cdot\sqrt{f_c'}\leq 0
\end{aligned}
\tag{11}
$$

### 2.2.6 Bending verification constraints

The thicknesses of the stem must have enough strength to resist the bending moments. The tensile strength of the concrete can be used in the design, because the stem of the wall can tolerate random cracks without detrimentally affecting their structural integrity, and ductility is not an essential feature of the design. The constraints from the bending verification can be given as follows:

$$\begin{aligned}
g_{10}(\mathrm{x}) &= 1.6\times\frac{\gamma_n\left(\frac{H}{6}\right)^3 K_a}{4{x_6}^2} - 1.2\times\frac{\gamma_c\frac{H}{6}(x_6+x_7)}{2x_6} - f_{ctd} \le 0\\
g_{11}(\mathrm{x}) &= 1.6\times\frac{\gamma_n\left(\frac{H}{3}\right)^3 K_a}{4{x_5}^2} - 1.2\times\frac{\gamma_c\frac{H}{6}(x_5+2x_6+x_7)}{2x_5} - f_{ctd} \le 0\\
g_{12}(\mathrm{x}) &= 1.6\times\frac{\gamma_n\left(\frac{H}{2}\right)^3 K_a}{4{x_4}^2} - 1.2\times\frac{\gamma_c\frac{H}{6}(x_4+2x_5+2x_6+x_7)}{2x_4} - f_{ctd} \le 0\\
g_{13}(\mathrm{x}) &= 1.6\times\frac{\gamma_n\left(\frac{2H}{3}\right)^3 K_a}{4{x_3}^2} - \\
&\quad 1.2\times\frac{\gamma_c\frac{H}{6}(x_3+2x_4+2x_5+2x_6+x_7)}{2x_3} - f_{ctd} \le 0\\
g_{14}(\mathrm{x}) &= 1.6\times\frac{\gamma_n\left(\frac{5H}{6}\right)^3 K_a}{4{x_2}^2} - \\
&\quad 1.2\times\frac{\gamma_c\frac{H}{6}(x_2+2x_3+2x_4+2x_5+2x_6+x_7)}{2x_2} - f_{ctd} \le 0
\end{aligned} \qquad (12)$$

where:

$f_{ctd}$ = Concrete design strength in tension

### 2.2.7 Design constraints

The minimum thickness for the concrete gravity wall at the top is recommended to be 0.3 m [27]. However, this is in contradiction with the aim of this study, i.e., to see the outline of the optimum cross-section this aspect is not taken into account. However, the $x_i$ dimensions must be greater than zero. Therefore, the following constraints can be defined.

$$\begin{bmatrix} -1 & 0 & 0 & 0 & 0 & 0 & 0\\ 0 & -1 & 0 & 0 & 0 & 0 & 0\\ 0 & 0 & -1 & 0 & 0 & 0 & 0\\ 0 & 0 & 0 & -1 & 0 & 0 & 0\\ 0 & 0 & 0 & 0 & -1 & 0 & 0\\ 0 & 0 & 0 & 0 & 0 & -1 & 0\\ 0 & 0 & 0 & 0 & 0 & 0 & -1 \end{bmatrix} \times \begin{bmatrix} x_1\\ x_2\\ x_3\\ x_4\\ x_5\\ x_6\\ x_7 \end{bmatrix} \le \begin{bmatrix} 0\\0\\0\\0\\0\\0\\0 \end{bmatrix} \qquad (13)$$

### 2.3 OPTIMIZATION METHOD

The constrained nonlinear optimization problem is defined as below:

$$\text{minimize } f(x) \qquad (14)$$

$$\text{subject to: } g_i(x) \le 0 \text{ for } i = 1, 2, \ldots, n \qquad (15)$$

where $f(x)$ and $g_i(x)$ are continuous and have continuous second partial derivatives, and the feasible region described by Eq. (15) is non-empty. A computer program was developed to solve the problem using the interior point method. The details and algorithms of this method can be found in books about nonlinear optimization [28].

## 3 OPTIMIZATION EXAMPLES

Several physical and mechanical properties of the walls and soils are assigned to the functions of the optimization problem in order to obtain the optimum cross-section of these situations. The assigned parameters corresponding to the optimization problem are given in

**Table 1**. Input parameters for design examples.

| Input Parameters | Unit | Symbol | Value |
|---|---|---|---|
| Height of the wall | m | H | 2.0 |
| Internal friction angle of the retained soil | degree | $\phi$ | 35 |
| Internal friction angle of the base soil | degree | $\phi_b$ | 35 |
| Friction angle between the wall base and the soil | degree | $\delta$ | 25.35 |
| Unit weight of the retained soil | kN/m$^3$ | $\gamma_n$ | 16.0 |
| Unit weight of the base soil | kN/m$^3$ | $\gamma_{nb}$ | 16.0 |
| Concrete design strength in tension | Mpa | $f_{ctd}$ | 0.9 |
| Concrete characteristic strength in compression | Mpa | $f'_c$ | 16.0 |
| Unit weight of the concrete | kN/m$^3$ | $\gamma_c$ | 25.0 |
| Factor of safety for the overturning stability | - | $FS_o$ | 2.0 |
| Factor of safety against sliding | - | $FS_s$ | 1.5 |
| Factor of safety for the bearing capacity | - | $FS_b$ | 3.0 |

Table 1. The heights of the walls are chosen to be 2.0, 3.0 and 4.0 m, because gravity retaining walls are generally used for heights of less than 5 m. The other parameters are selected as typical values for concrete and cohesionless soil. The coefficient of base friction between medium sand and cast in place concrete can be taken as between 0.45 and 0.55, according to the NAVFAC Design Manual [29].

The first example is the wall with a height of 2 m, and the $x_i$ values of the wall acquired from the optimization study are $x_1$=0.6578 m, $x_2$= 0.0934 m, $x_3$=0.0670 m, $x_4$=0.0436 m, $x_5$=0.0238 m, $x_6$=0.0084 m, and $x_7$=0.0000 m. The cross-sectional area of the wall is 0.3767 m$^2$, which is the result of the objective function too. The first striking feature of the cross-section is that a wide part occurs at the bottom of the wall like a footing (Fig. 4). It is seen from the results that active constraints determining the optimum values are the sliding and bending in the stem (Table 2). The constraints derived from the overturning, the total vertical force in the middle third, the bearing capacity, and the shear in the stem verifications are inactive.

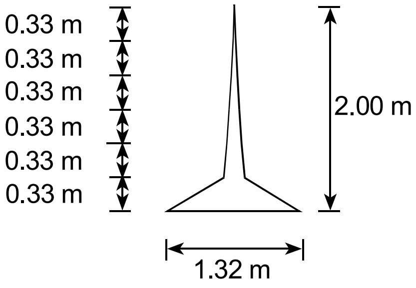

a) H=2

**Figure 4**. Optimum cross-section of a gravity retaining wall with a height of 2 m.

The second example is a retaining wall of 3.0 m in height. The optimum xi values are $x_1$=0.9633 m, $x_2$=0.1707 m, $x_3$=0.1225 m, $x_4$=0.0798 m, $x_5$=0.0436 m, $x_6$=0.0155 m, and $x_7$=0.0000, and the objective function takes the value of 0.9137 (Fig. 5). The factors of safety for the overturning, the sliding, and the bearing capacity are 4.1068, 1.5000, and 7.7099, respectively. The sliding and bending in the stem verifications are the constraints that are equal to zero. In other words, these constraints are active (Table 2). The cross-section of the wall has a very narrow upper part, almost zero at the top and a wide lower part like a footing. The wide lower part contributes the stability of the wall with the retained soil over the base of the wall, especially for the overturning and sliding checks.

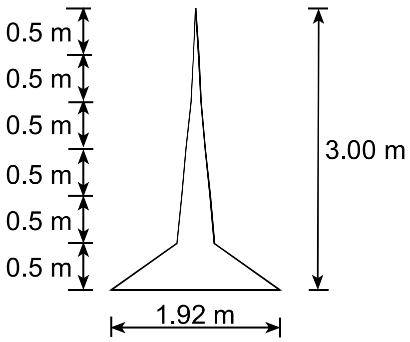

**Figure 5**. Optimum cross-section of a gravity retaining wall with a height of 3 m.

The retaining wall with a height of 4.0 m is considered as the third example. The factors of safety for the overturning, the sliding and the bearing capacity are 3.9975, 1.5000, and 7.0530, respectively. The optimum values of the variables are $x_1$=1.2584 m, $x_2$=0.2613 m, $x_3$=0.1878 m, $x_4$=0.1225 m, $x_5$=0.0670 m $x_6$=0.0238 m and $x_7$=0.0000 m and area of the cross-section is equal to 1.7220 m$^2$ (Fig. 6). The $g_2(x)$, $g_{10}(x)$, $g_{11}(x)$, $g_{12}(x)$, $g_{13}(x)$ and $g_{14}(x)$ constraints derived from the sliding and bending in the stem verifications, respectively, are zero at the optimum $x_i$ values. The cross-section of the wall is very similar to the walls with heights of 2 and 3 m.

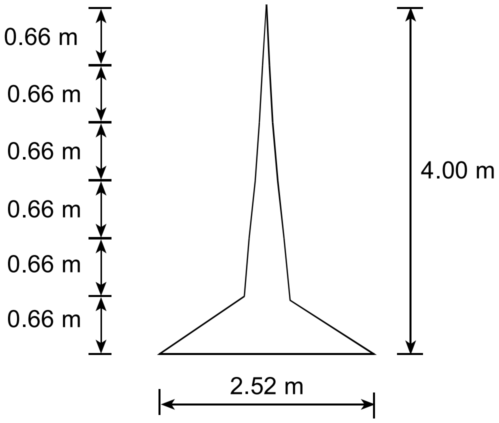

**Figure 6**. Optimum cross section of a gravity retaining wall with a height of 3 m.

The constraint functions are evaluated at the optimum solution points and the results are given in Table 2. The $g_2(x)$ constraint is equal to zero for all the gravity walls mentioned above. Thus, it can be said that the sliding constraint is active for all the walls. Additionally, the constraints derived from the bending in the stem verifications are also equal to zero for the walls. Therefore, bending in the stem checks becomes the other active constraint.

**Table 2**. Results of the constraint functions for the optimum $x_i$ values.

| Constraints | H=2 m | H=3 m | H=4 m |
|---|---|---|---|
| $g_1(x)$ | -12.9428 | -41.1071 | -92,3876 |
| $g_2(x)$ | 0.0000 | 0.0000 | 0,0000 |
| $g_3(x)$ | -23.1743 | -33.8651 | -44,0500 |
| $g_4(x)$ | -140.7466 | -203.0383 | -261,5659 |
| $g_5(x)$ | -4.3915 | -7.8965 | -11,9324 |
| $g_6(x)$ | -11.9432 | -21.2465 | -31,7960 |
| $g_7(x)$ | -21.2523 | -37.4571 | -55,5754 |
| $g_8(x)$ | -31.8122 | -55.5870 | -81,8056 |
| $g_9(x)$ | -43.3270 | -75.0844 | -109,6252 |
| $g_{10}(x)$ | 0.0000 | 0.0000 | 0,0000 |
| $g_{11}(x)$ | 0.0000 | 0.0000 | 0,0000 |
| $g_{12}(x)$ | 0.0000 | 0.0000 | 0,0000 |
| $g_{13}(x)$ | 0.0000 | 0.0000 | 0,0000 |
| $g_{14}(x)$ | 0.0000 | 0.0000 | 0,0000 |

A common feature of the optimum cross-sections of the walls is to have a wide lower part like a strip footing. In addition, the bending in the stem verifications determines the thicknesses of the stems at a regular interval from the base. The general outlines of the optimum cross-section are similar to each other (Fig. 4, 5, and 6). The normalized thicknesses obtained by dividing the thicknesses by the height of the wall are given in Fig. 7. The normalized thicknesses are almost equal for the walls and the normalized thicknesses increase slightly with increasing height, except for the thickness at the base (corresponding to $x_1$).

The normalized dimensions of the condition that has an internal friction angle of 25° for the retained soil and the foundation soil are given in Fig. 8. The other parameters are assigned to the constrained nonlinear programming problem, as in Table 1. Here, a 10° decrease in internal friction angle causes an approximately 52% increase in the normalized thickness corresponding to $x_1$, and a nearly 22% increase occurs in the normalized thicknesses corresponding to $x_2$, $x_3$, $x_4$, $x_5$, $x_6$. The active constraints are sliding and bending in the stem verifications in this case too. Such an increase in the width corresponding to $x_1$ is caused by a high lateral earth pressure due to a low internal friction angle. The base key can be utilized in order to obtain a viable bottom width.

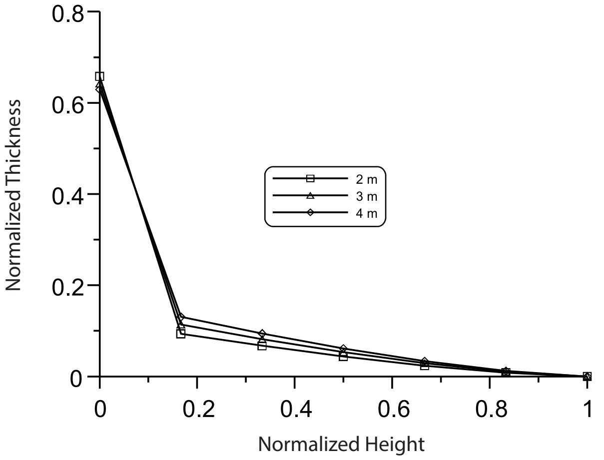

**Figure 7**. Normalized dimensions for $\phi$=35°.

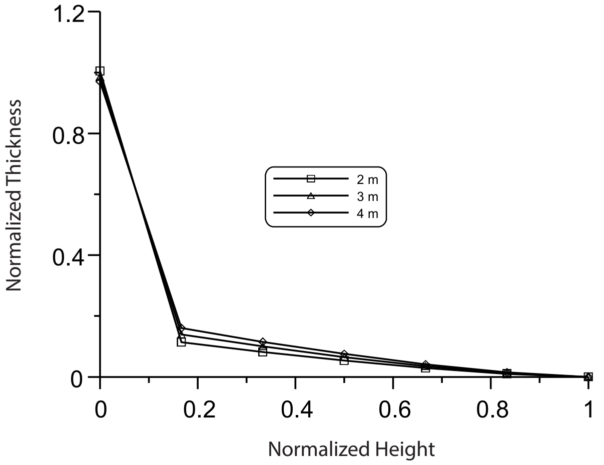

**Figure 8**. Normalized dimensions for $\phi$=25°.

The normalized dimensions given in Fig. 7 and Fig. 8 can be used for proportioning and the normalized thicknesses of the internal friction angles between 25° and 35° can be found by linear interpolation. The sliding constraint is the active constraint for all cases, so some measures, for example, adding a base key beneath the footing, installing anchors, etc., may be used to design more economic cross-sections for gravity retaining walls.

## 4 CONCLUSIONS

This study aimed to determine the optimum cross-section outline of a symmetrical gravity retaining wall on granular soil. The cross-sectional area of the plain concrete wall is assumed to be a direct indicator of the cost. Therefore, the objective function is defined as the cross-sectional area. Additionally, the constraints of the optimization problem are derived from the verifications that a concrete gravity retaining wall should satisfy. Thus, the constraint nonlinear optimization problem, defined by the objective function and constraints, is obtained. The problem is solved by developing a computer-program-based interior point method. The check of the sliding is an active constraint for external stability verifications and the bending in the stem verifications is an active constraint of the internal stability checks. The cross-sections of the walls with different heights have similar outlines. The outlines of the optimum cross-sections have wide lower parts, like wall footings, and slender stems that have minimum thicknesses satisfying the bending verifications. The areas of the optimum cross-sections are less than those of conventional plain concrete gravity retaining walls. The use of these optimum cross-sections will substantially reduce the costs.

## REFERENCES

[1] Whitlow, R. (2001). Basic soil mechanics, Fourth Edition. Prentice Hall, England.

[2] Coulomb, C.A. (1776). Essai sur une application des regles de maximus et minimus a Quelques Problèmes de Statique Relatifs a l'Architecture. Mem. Acad. Roy. Des Sciences 3, 38.

[3] Rankine, W.J.M. (1857). On the stability of loose earth. Philosophical Transactions of the Royal Society 147, 9-27.

[4] Peck, R.B., Hanson, W.E., Thornburn, T.H. (1974). Foundation Engineering, Second Edition. Wiley & Sons, New York.

[5] Clough, G.W., Duncan, J.M. (1971). Finite element analysis of retaining wall behaviour. Journal of Soil Mech.& Found. (ASCE) 97, 12, 1657-1673.

[6] Kulhawy, F.H. (1974). Analysis of a high gravity retaining wall. Proc. ASCE Conf. on Analysis and Design in Geotechnical Engineering, New York, 159-172.

[7] Nakai, T. (1985). Finite element computations for active and passive earth pressure problems on retaining wall. Soils & Found. 25, 3, 98-112.

[8] Bakeer, R.M. and Bhatia, S.K. (1989). Earth pressure behind a gravity retaining wall. Numer. Anal. Methods in Geomech. 13, 6, 665-673.

[9] Goh, A.T.C. (1993). Behavior of cantilever retaining walls. Journal of Geotechnical Engineering Division (ASCE) 199, 11, 1751-1770.

[10] Woodward, P.K. (1997). Earth pressure coefficients based on the Lade-Duncan failure criterion. Engineering Structures 9, 9, 733-737.

[11] Soubra, A.H. (2000). Static and seismic passive earth pressure coefficients on rigid retaining structure. Canadian Geotechnical Journal 37, 2, 463–478.

[12] Yang, X.L., Yin, J.H. (2006). Estimation of seismic passive earth pressures with nonlinear failure criterion. Engineering Structures 28, 3, 342-348.

[13] Coduto, D.P. (2001). Foundation Design, Second Edition, Prentice Hall, New Jersey.

[14] ACI (1999), Building Code Requirements for Structural Concrete (ACI 318-99), American Concrete Institute.

[15] Guerra, A., Kiousis, P.D. (2006). Design optimization of reinforced concrete structures. Computers and Concrete 3, 5, 313-334.

[16] Kortnik, J. (2009). Optimization of the high safety pillars for the underground excavation of natural stone blocks. Acta Geotechnica Slovenica 6, 1, 61-73.

[17] Gil-Martin, L.M., Hernandez-Montes, E., Aschheim, M. (2010). Optimization of piers for retaining walls. Structural and Multidisciplinary Optimization 41, 6, 979-987.

[18] Mendjel, D., Messast, S. (2012). Development of limit equilibrium method as optimization in slope stability analysis. Structural Engineering and Mechanics 41, 3, 339-348.

[19] Jelusic, P., Zlender, B. (2013). Soil-nail wall stability analysis using ANFIS. Acta Geotechnica Slovenica 10, 1, 35-48.

[20] Rhomberg, E.J., Street, W.M. (1981). Optimal design of retaining walls. Journal of Structural Division, ASCE 107, 5, 992-1002.

[21] Alshawi, F.A.N., Mohammad, A.L., Farid, B.J. (1988). Optimum design of tied-back retaining walls. The Structural Engineering 66, 6, 97-105.

[22] Saribas, A., Erbatur, F. (1996). Optimization and sensitivity of retaining structures. Journal of Geotechnical Engineering, ASCE 122, 8, 649-656.

[23] Basudkar, P.K. and Lakshman, B. (2006). Optimal cost design of cantilever retaining walls. Proc. Indian Geotechnical Conference, Chennai, 525-528.

[24] Truman, K.Z., Hoback, A.S. (1992). Optimization of steel piles under rigid slab foundations using optimality criteria. Structural and Multidisciplinary Optimization 5, 1, 30-36.

[25] Duncan, J.M., Clough, G.W., Ebeling, R.M. (1990). Design and performance of earth retaining structures. Proc. ASCE Conf. on Design and Peformance of Earth Retaining Structures, New York, 251-277.

[26] Terzaghi, K. (1943). Theoretical Soil Mechanics. John Wiley and Sons, New York.

[27] Smith, G.N., Smith, I.G.N. (1998). Elements of Soil Mechanics. John Wiley and Sons, New York.

[28] Antoniou A., Lu, W.S. (2007). Practical Optimization Algorithms and Engineering Applications. Springer, New York.

[29] U.S. NAVY (1982b). Foundations and Earth Structures-NAVFAC Design Manual 7.2. Naval Facilities Engineering Command, Arlington, VA.

# NAVODILA AVTORJEM

## VSEBINA ČLANKA

Članek naj bo napisan v naslednji obliki:

- Naslov, ki primerno opisuje vsebino članka in ne presega 80 znakov.
- Izvleček, ki naj bo skrajšana oblika članka in naj ne presega 250 besed. Izvleček mora vsebovati osnove, jedro in cilje raziskave, uporabljeno metodologijo dela, povzetek izidov in osnovne sklepe.
- Največ 6 ključnih besed, ki bi morale biti napisane takoj po izvlečku.
- Uvod, v katerem naj bo pregled novejšega stanja in zadostne informacije za razumevanje ter pregled izidov dela, predstavljenih v članku.
- Teorija.
- Eksperimentalni del, ki naj vsebuje podatke o postavitvi preiskusa in metode, uporabljene pri pridobitvi izidov.
- Izidi, ki naj bodo jasno prikazani, po potrebi v obliki slik in preglednic.
- Razprava, v kateri naj bodo prikazane povezave in posplošitve, uporabljene za pridobitev izidov. Prikazana naj bo tudi pomembnost izidov in primerjava s poprej objavljenimi deli.
- Sklepi, v katerih naj bo prikazan en ali več sklepov, ki izhajajo iz izidov in razprave.
- Vse navedbe v besedilu morajo biti na koncu zbrane v seznamu literature, in obratno.

### Dodatne zahteve

- Vrstice morajo biti zaporedno oštevilčene.
- Predložen članek ne sme imeti več kot 18 strani (brez tabel, legend in literature); velikost črk 12, dvojni razmik med vrsticami. V članek je lahko vključenih največ 10 slik. Isti rezultati so lahko prikazani v tabelah ali na slikah, ne pa na oba načina.
- Potrebno je priložiti imena, naslove in elektronske naslove štirih potencialnih recenzentov članka. Urednik ima izključno pravico do odločitve, ali bo te predloge upošteval.

## ENOTE IN OKRAJŠAVE

V besedilu, preglednicah in slikah uporabljajte le standardne označbe in okrajšave SI. Simbole fizikalnih veličin v besedilu pišite poševno (npr. *v*, *T* itn.). Simbole enot, ki so sestavljene iz črk, pa pokončno (npr. Pa, m itn.). Vse okrajšave naj bodo, ko se prvič pojavijo, izpisane v celoti.

## SLIKE

Slike morajo biti zaporedno oštevilčene in označene, v besedilu in podnaslovu, kot sl. 1, sl. 2 itn. Posnete naj bodo v katerem koli od razširjenih formatov, npr. BMP, JPG, GIF. Za pripravo diagramov in risb priporočamo CDR format (CorelDraw), saj so slike v njem vektorske in jih lahko pri končni obdelavi preprosto povečujemo ali pomanjšujemo.

Pri označevanju osi v diagramih, kadar je le mogoče, uporabite označbe veličin (npr. *v*, *T* itn.). V diagramih z več krivuljami mora biti vsaka krivulja označena. Pomen oznake mora biti razložen v podnapisu slike.

Za vse slike po fotografskih posnetkih je treba priložiti izvirne fotografije ali kakovostno narejen posnetek.

## PREGLEDNICE

Preglednice morajo biti zaporedno oštevilčene in označene, v besedilu in podnaslovu, kot preglednica 1, preglednica 2 itn. V preglednicah ne uporabljajte izpisanih imen veličin, ampak samo ustrezne simbole. K fizikalnim količinam, npr. *t* (pisano poševno), pripišite enote (pisano pokončno) v novo vrsto brez oklepajev. Vse opombe naj bodo označene z uporabo dvignjene številke$^1$.

## SEZNAM LITERATURE

### Navedba v besedilu

Vsaka navedba, na katero se sklicujete v besedilu, mora biti v seznamu literature (in obratno). Neobjavljeni rezultati in osebne komunikacije se ne priporočajo v seznamu literature, navedejo pa se lahko v besedilu, če je nujno potrebno.

### Oblika navajanja literature

**V besedilu**: Navedite reference zaporedno po številkah v oglatih oklepajih v skladu z besedilom. Dejanski avtorji so lahko navedeni, vendar mora obvezno biti podana referenčna številka.

Primer: »..... kot je razvidno [1,2]. Brandl and Blovsky [4], sta pridobila drugačen rezultat…«

**V seznamu**: Literaturni viri so oštevilčeni po vrstnem redu, kakor se pojavijo v članku. Označimo jih s številkami v oglatih oklepajih.

*Sklicevanje na objave v revijah*:

[1] Jelušič P., Žlender, B. 2013. Soil-nail wall stability analysis using ANFIS. Acta Geotechnica Slovenica 10(1), 61-73.

*Sklicevanje na knjigo*:

[2] Šuklje, L. 1969. Rheological aspects of soil mechanics. Wiley-Interscience, London

*Sklicevanje na poglavje v monografiji*:

[3] Mitchel, J.K. 1992. Characteristics and mechanisms of clay creep and creep rupture, in N. Guven, R.M. Pollastro (eds.), Clay-Water Interface and Its Rheological Implications, CMS Workshop Lectures, Vol. 4, The clay minerals Society, USA, pp. 212-244..

*Sklicevanje na objave v zbornikih konferenc*:

[4] Brandl, H., Blovsky, S. 2005. Slope stabilization with socket walls using the observational method. Proc. Int. conf. on Soil Mechanics and Geotechnical Engineering, Bratislava, pp. 2485-2488.

Sklicevanje na spletne objave:

[5] Kot najmanj, je potrebno podati celoten URL. Če so poznani drugi podatki (DOI, imena avtorjev, datumi, sklicevanje na izvorno literaturo), se naj prav tako dodajo.

## PODATKI O AVTORJIH

Članku priložite tudi podatke o avtorjih: imena, nazive, popolne poštne naslove, številke telefona in faksa, naslove elektronske pošte. Navedite kontaktno osebo.

## SPREJEM ČLANKOV IN AVTORSKE PRAVICE

Uredništvo si pridržuje pravico do odločanja o sprejemu članka za objavo, strokovno oceno mednarodnih recenzentov in morebitnem predlogu za krajšanje ali izpopolnitev ter terminološke in jezikovne korekture. Z objavo preidejo avtorske pravice na revijo ACTA GEOTECHNICA SLOVENICA. Pri morebitnih kasnejših objavah mora biti AGS navedena kot vir.

---

Vsa nadaljnja pojasnila daje:

Uredništvo
ACTA GEOTECHNICA SLOVENICA
Univerza v Mariboru,
Fakulteta za gradbeništvo
Smetanova ulica 17, 2000 Maribor, Slovenija
E-pošta: ags@uni-mb.si

# INSTRUCTIONS FOR AUTHORS

## FORMAT OF THE PAPER

The paper should have the following structure:

- A Title, which adequately describes the content of the paper and should not exceed 80 characters;
- An Abstract, which should be viewed as a mini version of the paper and should not exceed 250 words. The Abstract should state the principal objectives and the scope of the investigation and the methodology employed; it should also summarise the results and state the principal conclusions;
- Immediately after the abstract, provide a maximum of 6 keywords;
- An Introduction, which should provide a review of recent literature and sufficient background information to allow the results of the paper to be understood and evaluated;
- A Theoretical section;
- An Experimental section, which should provide details of the experimental set-up and the methods used to obtain the results;
- A Results section, which should clearly and concisely present the data, using figures and tables where appropriate;
- A Discussion section, which should describe the relationships shown and the generalisations made possible by the results and discuss the significance of the results, making comparisons with previously published work;
- Conclusions, which should present one or more conclusions that have been drawn from the results and subsequent discussion;
- A list of References, which comprises all the references cited in the text, and vice versa.

## Additional Requirements for Manuscripts

- Use double line-spacing.
- Insert continuous line numbering.
- The submitted text of Research Papers should cover no more than 18 pages (without Tables, Legends, and References, style: font size 12, double line spacing). The number of illustrations should not exceed 10. Results may be shown in tables or figures, but not in both of them.
- Please submit, with the manuscript, the names, addresses and e-mail addresses of four potential referees. Note that the editor retains the sole right to decide whether or not the suggested reviewers are used.

## UNITS AND ABBREVIATIONS

Only standard SI symbols and abbreviations should be used in the text, tables and figures. Symbols for physical quantities in the text should be written in Italics (e.g. $v$, $T$, etc.). Symbols for units that consist of letters should be in plain text (e.g. Pa, m, etc.).
All abbreviations should be spelt out in full on first appearance.

## FIGURES

Figures must be cited in consecutive numerical order in the text and referred to in both the text and the caption as Fig. 1, Fig. 2, etc. Figures may be saved in any common format, e.g. BMP, JPG, GIF. However, the use of CDR format (CorelDraw) is recommended for graphs and line drawings, since vector images can be easily reduced or enlarged during final processing of the paper.

When labelling axes, physical quantities (e.g. $v$, $T$, etc.) should be used whenever possible. Multi-curve graphs should have individual curves marked with a symbol; the meaning of the symbol should be explained in the figure caption. Good quality black-and-white photographs or scanned images should be supplied for the illustrations.

## TABLES

Tables must be cited in consecutive numerical order in the text and referred to in both the text and the caption as Table 1, Table 2, etc. The use of names for quantities in tables should be avoided if possible: corresponding symbols are preferred. In addition to the physical quantity, e.g. $t$ (in Italics), units (normal text), should be added on a new line without brackets.
Any footnotes should be indicated by the use of the superscript$^1$.

## LIST OF REFERENCES

### citation in text

Please ensure that every reference cited in the text is also present in the reference list (and vice versa). Any references cited in the abstract must be given in full. Unpublished results and personal communications are not recommended in the reference list, but may be mentioned in the text, if necessary.

### Reference style

**Text**: Indicate references by number(s) in square brackets consecutively in line with the text. The actual authors can be referred to, but the reference number(s) must always be given:

Example: "... as demonstrated [1,2]. Brandl and Blovsky [4] obtained a different result ..."

**List**: Number the references (numbers in square brackets) in the list in the order in which they appear in the text.

*Reference to a journal publication*:
[1] Jelušič P., Žlender, B. 2013. Soil-nail wall stability analysis using ANFIS. Acta Geotechnica Slovenica 10(1), 61-73.

*Reference to a book*:
[2] Šuklje, L. 1969. Rheological aspects of soil mechanics. Wiley-Interscience, London

*Reference to a chapter in an edited book*:
[3] Mitchel, J.K. 1992. Characteristics and mechanisms of clay creep and creep rupture, in N. Guven, R.M. Pollastro (eds.), Clay-Water Interface and Its Rheological Implications, CMS Workshop Lectures, Vol. 4, The clay minerals Society, USA, pp. 212-244.

*Conference proceedings:*
[4] Brandl, H., Blovsky, S. 2005. Slope stabilization with socket walls using the observational method. Proc. Int. conf. on Soil Mechanics and Geotechnical Engineering, Bratislava, pp. 2485-2488.

*Web references*:
[5] As a minimum, the full URL should be given and the date when the reference was last accessed. Any further information, if known (DOI, author names, dates, reference to a source publication, etc.), should also be given.

## AUTHOR INFORMATION

The following information about the authors should be enclosed with the paper: names, complete postal addresses, telephone and fax numbers and E-mail addresses. Indicate the nameof the corresponding author.

## ACCEPTANCE OF PAPERS AND COPYRIGHT

The Editorial Committee of the Slovenian Geotechnical Review reserves the right to decide whether a paper is acceptable for publication, to obtain peer reviews for the submitted papers, and if necessary, to require changes in the content, length or language.
On publication, copyright for the paper shall pass to the ACTA GEOTECHNICA SLOVENICA. The AGS must be stated as a source in all later publication.

For further information contact:

Editorial Board
ACTA GEOTECHNICA SLOVENICA
University of Maribor,
Faculty of Civil Engineering
Smetanova ulica 17, 2000 Maribor, Slovenia
E-mail: ags@uni-mb.si

## NAMEN REVIJE

Namen revije ACTA GEOTECHNICA SLOVENICA je objavljanje kakovostnih teoretičnih člankov z novih pomembnih področij geomehanike in geotehnike, ki bodo dolgoročno vplivali na temeljne in praktične vidike teh področij.

ACTA GEOTECHNICA SLOVENICA objavlja članke s področij: mehanika zemljin in kamnin, inženirska geologija, okoljska geotehnika, geosintetika, geotehnične konstrukcije, numerične in analitične metode, računalniško modeliranje, optimizacija geotehničnih konstrukcij, terenske in laboratorijske preiskave.

Revija redno izhaja dvakrat letno.

## AVTORSKE PRAVICE

Ko uredništvo prejme članek v objavo, prosi avtorja(je), da prenese(jo) avtorske pravice za članek na izdajatelja, da bi zagotovili kar se da obsežno razširjanje informacij. Naša revija in posamezni prispevki so zaščiteni z avtorskimi pravicami izdajatelja in zanje veljajo naslednji pogoji:

### fotokopiranje

V skladu z našimi zakoni o zaščiti avtorskih pravic je dovoljeno narediti eno kopijo posameznega članka za osebno uporabo. Za naslednje fotokopije, vključno z večkratnim fotokopiranjem, sistematičnim fotokopiranjem, kopiranjem za reklamne ali predstavitvene namene, nadaljnjo prodajo in vsemi oblikami nedobičkonosne uporabe je treba pridobiti dovoljenje izdajatelja in plačati določen znesek.

Naročniki revije smejo kopirati kazalo z vsebino revije ali pripraviti seznam člankov z izvlečki za rabo v svojih ustanovah.

### elektronsko shranjevanje

Za elektronsko shranjevanje vsakršnega gradiva iz revije, vključno z vsemi članki ali deli članka, je potrebno dovoljenje izdajatelja.

## ODGOVORNOST

Revija ne prevzame nobene odgovornosti za poškodbe in/ali škodo na osebah in na lastnini na podlagi odgovornosti za izdelke, zaradi malomarnosti ali drugače, ali zaradi uporabe kakršnekoli metode, izdelka, navodil ali zamisli, ki so opisani v njej.

## AIMS AND SCOPE

ACTA GEOTECHNICA SLOVENICA aims to play an important role in publishing high-quality, theoretical papers from important and emerging areas that will have a lasting impact on fundamental and practical aspects of geomechanics and geotechnical engineering.

ACTA GEOTECHNICA SLOVENICA publishes papers from the following areas: soil and rock mechanics, engineering geology, environmental geotechnics, geosynthetic, geotechnical structures, numerical and analytical methods, computer modelling, optimization of geotechnical structures, field and laboratory testing.

The journal is published twice a year.

## COPYRIGHT

Upon acceptance of an article by the Editorial Board, the author(s) will be asked to transfer copyright for the article to the publisher. This transfer will ensure the widest possible dissemination of information. This review and the individual contributions contained in it are protected by publisher's copyright, and the following terms and conditions apply to their use:

### photocopying

Single photocopies of single articles may be made for personal use, as allowed by national copyright laws. Permission of the publisher and payment of a fee are required for all other photocopying, including multiple or systematic copying, copying for advertising or promotional purposes, resale, and all forms of document delivery.

Subscribers may reproduce tables of contents or prepare lists of papers, including abstracts for internal circulation, within their institutions.

### electronic storage

Permission of the publisher is required to store electronically any material contained in this review, including any paper or part of the paper.

## RESPONSIBILITY

No responsibility is assumed by the publisher for any injury and/or damage to persons or property as a matter of product liability, negligence or otherwise, or from any use or operation of any methods, products, instructions or ideas contained in the material herein.

9 771854 017001

Univerza v Mariboru

Fakulteta za gradbeništvo

www.fg.um.si

Univerza
*v Ljubljani*

Fakulteta
*za gradbeništvo*
*in geodezijo*

*Naravoslovnotehniška*
Fakulteta

www.fgg.uni-lj.si

www.ntf.uni-lj.si

SLOVENSKO GEOTEHNIŠKO DRUŠTVO
SLOVENIAN GEOTECHNICAL SOCIETY

www.sloged.si

SLOVENSKO DRUŠTVO ZA
PODZEMNE GRADNJE

SLOVENIAN SOCIETY FOR
UNDERGROUND STRUCTURES

www.ita-slovenia.si